# Modulation of GPCR function by heteromerization

**Nil Casajuana-Martín**

UAB
Universitat Autònoma
de Barcelona

# MODULATION OF GPCR FUNCTION BY HETEROMERIZATION

**Nil Casajuana-Martín**

**Supervisors**
Leonardo Pardo
Sergi Ferré

Laboratory of Computational Medicine
Biostatistics Unit, Faculty of Medicine
Universitat Autònoma Barcelona

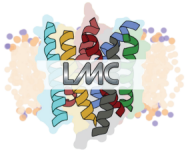


Doctorate program in Bioinformatics
2024

# Table of Contents

# 1 INTRODUCTION

## 1.1 G-Protein Coupled Receptors (GPCRs)

### 1.1.1 Historical perspective

The Cambridge physiologist John Newport Langley proposed in 1909 the presence of a “receptive substance” in our organism that would mediate drug action (Maehle *et al.*, 2002). This idea remained hypothetical until Raymond P. Ahlquist made his famous distinction, in 1948, between α- and β-adrenoceptors. Earl Sutherland won a Noble Prize in 1971 for his discoveries concerning the mechanisms of the action of hormones, especially adrenaline, via second messengers, namely cAMP (The Nobel Prize in Physiology or Medicine 1971 - Press release - NobelPrize.org). Years later, Alfred Gillman and Martin Rodbell introduced the figure of the signal transductor, a “mediator” between the first messenger and the second messenger: the G-protein (The Nobel Prize in Physiology or Medicine 1994 - Press release - NobelPrize.org). However, there was still a missing piece in the puzzle because up until then the concept of a “receptor” was somehow accepted but still enigmatic. One of the key events in the acceptance of the concept of receptor was the introduction in 1965 of a subtype specific pharmaceutical (propranolol) as the first clinically useful β-adrenergic receptor blocker, for which James W. Black was awarded with the Nobel Prize in 1988 (Press release: The Nobel Prize in Chemistry 1965 - NobelPrize.org). “Receptive substances” are, these days, known as the G-protein-coupled receptor (GPCR) family of proteins. Robert Lefkowitz and Brian Kobilka biochemically identified and unraveled the structure and dynamics of GPCRs, earning them the Nobel prize in 2012 (Press release: The Nobel Prize in Chemistry 2012 - NobelPrize.org).

### 1.1.2 Families of GPCRs, G-proteins and effectors

We now know that GPCRs are highly diversified in mammalian genomes with current estimates of about 800 genes (3-4% of the human proteome) (Fredriksson and Schiöth, 2005). These include GPCRs for sensory functions that mediate olfaction (~400 receptors), taste (33 receptors), light perception (10 receptors) and pheromone signaling (5 receptors) (Maßberg and Hatt, 2018; Mombaerts, 2004); and non-sensory GPCRs (~350 receptors) that transduce signals of endogenous ligands (Alexander *et al.*, 2019). The first classification scheme of GPCRs dates from 1994 and divided the sequences into classes A-F of which D and E were not found in vertebrates (Kolakowski, 1994). A more recent approach, which overlaps the A-F nomenclature, named the classification as "GRAFS" due to subfamily nomenclature: Glutamate (class C, 22 receptors), Rhodopsin (class A, >700 receptors including ~400 olfactory receptors), Adhesion (class B2, 33 receptors), Frizzled (class F, 11 receptors) and Secretin (class B1, 14 receptors) (Alexander *et al.*, 2019; Fredriksson and Schiöth, 2005). The response of GPCRs (**Figure 1**) to extracellular signals is operated through second messenger cascades controlled by different heterotrimeric guanine nucleotide-binding G-proteins (G-proteins) coupled at their intracellular regions (Oldham and Hamm, 2008; Gilman, 1987). In humans, there are 16 Gα subunits that can signal independently (classified as Gαs, Gαi, Gαq and Gα12) and 5 Gβ and 13 Gγ subunits that are obligate heterodimers (Gβγ) to signal (Wootten *et al.*, 2018). The active conformation of the receptor is blocked and signaling is attenuated by agonist dissociation and/or deactivation through interaction with visual/β-arrestins (there are 4 arrestins involved in mammalian GPCR signaling) (Peterson and Luttrell, 2017) in response to activation-specific

phosphorylation by G-protein-coupled receptor kinases (GRKs, there are 7 in mammals) (Komolov and Benovic, 2018).

### 1.1.3 Structures of GPCRs

Significant advances in crystallization of GPCRs (Serrano-Vega *et al.*, 2008; Day *et al.*, 2007), together with cryogenic electron microscopy (cryo-EM) (Renaud *et al.*, 2018) have permitted the elucidation of structures of many members of this family (Munk *et al.*, 2019). All GPCR structures share a common architecture of seven transmembrane domains (TMs) connected to each other with three extracellular (ECL) and three intracellular loops (ICL), a disulfide bridge between ECL2 and TM3, and a cytoplasmic C–terminus containing an α-helix (helix 8) parallel to the cell membrane. Closer comparison of these crystal structures has revealed subfamily-conserved changes in the α-helical scaffold in the form of tight ($3_{10}$ turn) and wide (π bulge) turns at the extracellular part of the TM domains (Katritch *et al.*, 2013; Gonzalez *et al.*, 2012). These differences are believed to be derived from residue insertion or deletion events accumulated during the evolution of GPCRs. Extensive structural characterization of the family has permitted structure-based sequence alignments between the TM helices of classes A-F and propose a cross-class GPCR residue numbering (Isberg *et al.*, 2015) based on a modified Ballesteros-Weinstein scheme (Ballesteros and Weinstein, 1995).

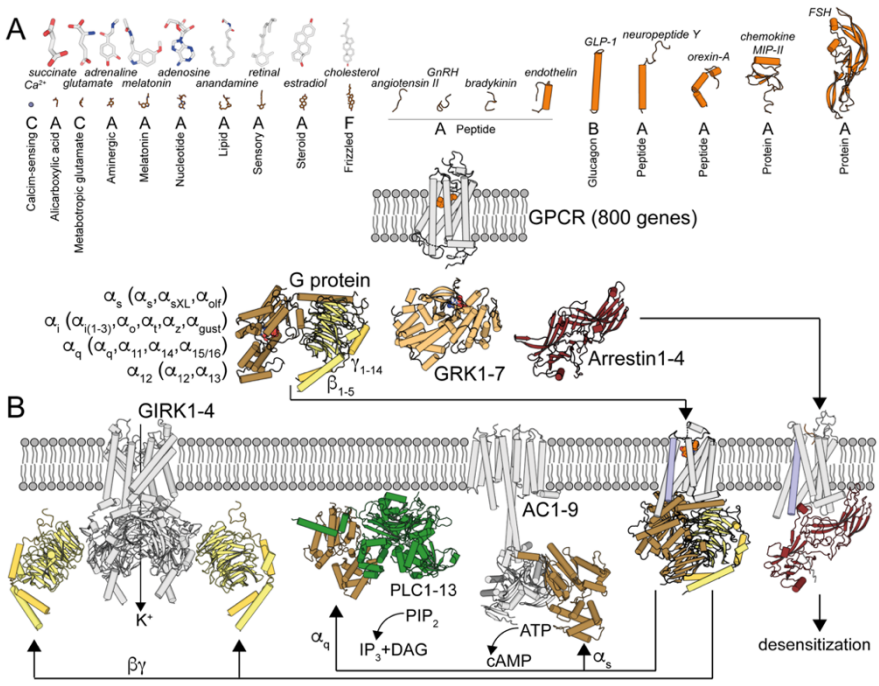


***Figure 1. G-protein-coupled receptor signaling. (a)*** *Representative extracellular ligands, depicted in a proportional (in orange) and in a non-proportional (for non-peptidic ligands in white) size, from small ions (left) to large proteins (right). GPCR class (A-C, F) and family to which these ligands belong are also shown according to GPCRdb (Pándy-Szekeres et al., 2018). These ligands bind at the extracellular side of GPCRs (illustrated with the structure of retinal-bound rhodopsin in white (Palczewski et al., 2000), PDB id 1F88) and transduce the signal to the intracellular side. Active GPCRs mainly interact with intracellular heterotrimeric G-proteins (illustrated with the structure of GDP-bound Giα1Gβ1Gγ2 in brown/yellow (Wall et al., 1995), 1GP2), G-protein-coupled receptor kinases (illustrated with the structure of ATP-bound GRK1 in light orange (Singh et al., 2008), 3C4W), and arrestins (illustrated with the structure of arrestin1 in red (Granzin et al., 1998), 1AYR).* ***(b)*** *Agonist binding triggers the outward movement of TM6 (in blue), opening an intracellular cavity for G-protein binding (illustrated with the crystal structure of the ternary complex composed of agonist- $\beta_2$AR-Gs (Rasmussen et al., 2011), 3SN6). The formation of the ternary complex triggers an exchange of GDP for GTP, through a large-scale opening of the α-helical domain from the Ras domain in the α-subunit (Dror et al., 2015; Galés et al., 2006), resulting in dissociation of the α and βγ subunits. The GTP-bound state of the α-subunit binds either AC to convert ATP into cAMP (illustrated with the cryo-EM structure of AC9 bound to $\alpha_s$ (Qi et al., 2019), 6R3Q) or PLC to catalyze the hydrolysis of PIP2 to IP3 and DAG (illustrated with the crystal structure of PLC-β3 bound to $\alpha_q$ (Waldo et al., 2010), 3OHM). βγ-subunits can interact with GIRKs so that they become permeable to K+ ions (illustrated with the crystal structure of GIRK2 in complex with βγ (Whorton and MacKinnon, 2013), 4KFM). Activation of GPCRs also leads to phosphorylation by GRKs and coupling to arrestins (illustrated with the cryo-EM structure of neurotensin receptor 1 in complex with arrestin2/β-arrestin1 (Huang et al., 2020), 6UP7) for desensitization and arrestin-mediated activation of downstream effector proteins. Adapted from Hilger et al. (Hilger et al., 2018).*

**Figure 2a** shows representative structures of families A-C, and F. In class A GPCRs, the endogenous ligand (i.e., adrenaline) binds in a conserved pocket within the seven TM (7TM) domain of the receptor ($\beta_2$-adrenergic). Class B GPCRs for peptide hormones contain an extracellular N-terminal domain that binds to the C-terminal half of the peptide, while the N-terminal part of the peptide penetrates into the receptor's 7TM bundle to a depth comparable to adrenaline in the structure of class A $\beta_2$-adrenergic receptor. Class C GPCRs are structurally more complex than the other classes. First, they form obligate cysteine-linked homodimers. Second, each protomer contains a large and characteristic extracellular Venus fly-trap (VFT) domain which can bind orthosteric ligands (i.e., the endogenous agonist glutamate), a 7TM domain, and a cysteine rich domain (CRD) that connects these two domains. Class F GPCRs are composed of the 7TM domain and an extracellular CRD. In this thesis we have worked on class A GPCRs of the aminergic (5-$HT_{2A}$R, $D_1$R, $D_2$R, $D_3$R), lipid ($CB_1$R), nucleotide ($A_{2A}$R), and peptide (MOR, Gal1R) subfamilies (**Figure 2b**). Black dots indicate that experimental structures of all these studied GPCRs are known.

GPCRs transduce exogenous signals such as several million different colors or one trillion olfactory stimuli (Bushdid *et al.*, 2014) or one thousand bitter molecules (Dagan-Wiener *et al.*, 2019) and endogenous signals that range in size from ions (e.g., $Ca^{2+}$) to small molecules (e.g., glutamate, neurotransmitters) to peptides (e.g., opioids, endothelin, glucagon) or large proteins (e.g., chemokines, glycoprotein hormones) to the cytoplasmic side of the cell membrane (to 16 G-proteins, 4 arrestins, or 7 GRKs) (**Figure 1**). Thus, GPCRs interact with an extraordinary diversity of ligands by means of their extracellular domains and/or the extracellular part of the TM segments, and with a small repertoire of

signaling G-proteins via their intracellular domains and/or the intracellular part of the TM segments. Consequently, GPCRs have adapted, during their evolution, the conserved 7TM scaffold to the structural characteristics of the highly diverse range of extracellular ligands, through structural plasticity, to a conserved set of conformational rearrangements of the TM segments at the intracellular part (Deupi *et al.*, 2007). These findings have been corroborated with the analysis of known inactive and active structures of GPCRs (Venkatakrishnan *et al.*, 2016).

### 1.1.4 GPCRs as drug targets

GPCRs regulate a vast amount of cellular processes (Wootten *et al.*, 2018), and their malfunction, with 435 disease-associated mutations (Zhou *et al.*, 2019), commonly translates into pathological outcomes (Schöneberg and Liebscher, 2021). Thus, they form one of the most important pharmaceutical drug-target class (475 drugs in the market that represent ~34% of all drugs approved by the US Food and Drug Administration) (Hauser *et al.*, 2017). However, these drugs target only 108 unique GPCRs, which represent <10% of all known GPCRs (or ~30% of the ~360 non-olfactory GPCRs), but account for ~27% of the global market share of therapeutic drugs, with aggregated sales for 2011–2015 of ~US$890 billion (Oprea *et al.*, 2018). Thus, the GPCR family is globally underused regarding its potential in drug discovery. For instance, there are ~140 orphan receptors (oGPCRs), whose endogenous ligands remain unknown and therefore their physiological role in the human biology not thoroughly understood.

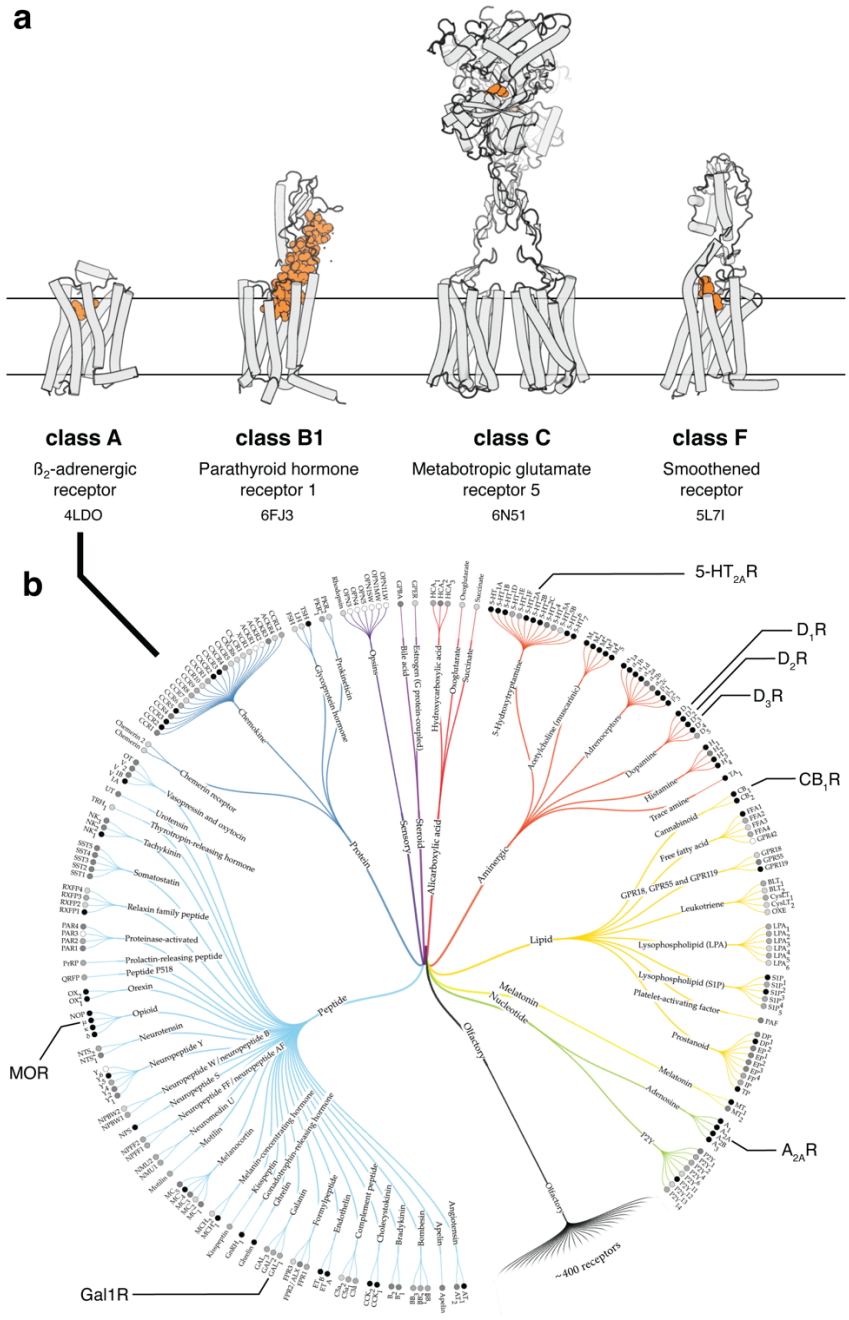


*Figure 2. Representative structures of GPCRs.* ***(a)*** *Schematic view of classes A, B1, C, and F showing the orthosteric ligand in orange spheres. Class B2 is not shown for simplicity.* ***(b)*** *Phylogenetic tree of class A GPCRs (taken from https://gpcrdb.org/structure/statistics). Receptors involved in this thesis are highlighted.*

### 1.1.5 The conformational landscape of GPCRs

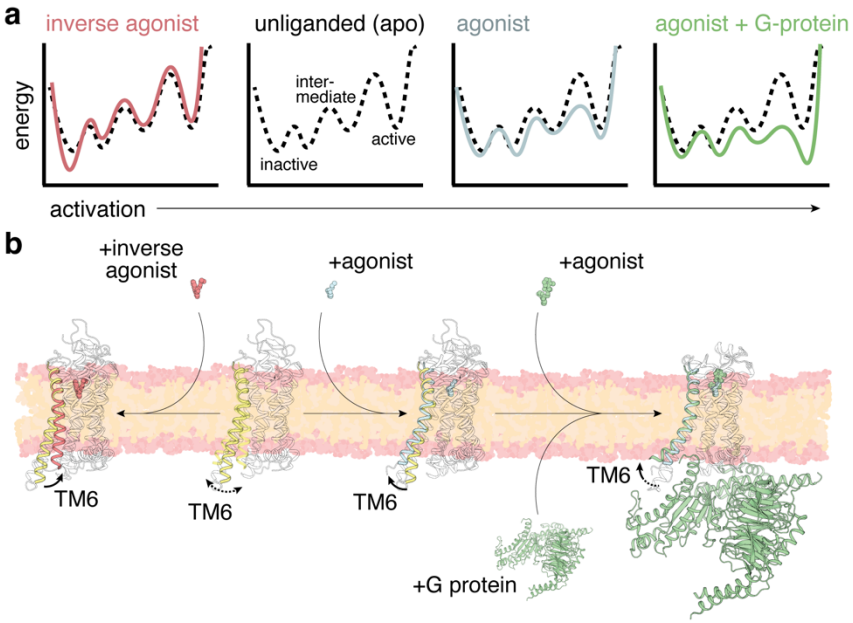


*Figure 3. Dynamic properties of GPCRs. (a) Scheme of the conformational energy landscape of GPCR activation accompanied by (b) a representation of the hallmarks of GPCR activation, TM6 outward movement. In apo receptor the TM6 is highly dynamic, mainly populating inactive-like conformations. The inactive conformation is stabilized by inverse agonists while agonist binding promotes outward movement of TM6. Fully stabilized active conformation of TM6 is only achieved in presence of both agonist and G-protein. Adapted from (Casiraghi, 2023). Credit to Dr. Llinas del Torrent.*

Our understanding of the details of GPCR signaling has advanced greatly. In a simple manner, receptors exist as a population of different conformations: resting, active, inactive, and various intermediates which are spread over an energy landscape (**Figure 3**). The transition probability between conformations depends on their energy difference and the energy barrier between them. Ligands or coupling G-proteins bind preferentially to specific state(s), increasing the proportion of those states, leading to more signaling of the corresponding pathway. Thus, the diverse pharmacology of specific GPCRs can be understood: 1) basal activity arising from a small population of receptors in an active state even in the

absence of agonist; 2) inverse agonists preferring inactive states; 3) agonists favoring and stabilizing intermediate states, and 4) final formation of the agonist-receptor-active G-protein complex further increasing activity (Nygaard *et al.*, 2013; Casiraghi, 2023).

### 1.1.6 GPCR activation

GPCRs are allosteric machines in the way they function. When the ligand binds in the orthosteric cavity (upper/extracellular half of TMD) a signal is transmitted to the intracellular half that broadens the interior cavity. At its turn, interaction with a G-protein triggers the opening of the α-helical domain of the α-subunit for GDP/GTP exchange. The distance between the orthosteric binding pocket of the receptor and the GDP binding site of the G-protein is around 80 Å. The way the "signal" is transmitted is quite well established structurally.

Agonist binding at the extracellular orthosteric site (**Figure 4a**) triggers local structural changes that vary among GPCR classes and families, such as the hydrogen bond interaction between agonists and $S^{5.46}$ in the $\beta_2$-adrenergic receptor (Rasmussen *et al.*, 2011) (**Figure 4a**), the movement of $W^{6.48}$ in the adenosine $A_{2A}$ receptor (Xu *et al.*, 2011), or a conformational toggle switch of $F^{3.36}$ in the cannabinoid $CB_1$ receptor (Krishna Kumar *et al.*, 2019). These changes occur in the immediate proximity of the ligand, but they must translate into larger-scale helix movements at the intracellular site (Rasmussen *et al.*, 2011). This is initially triggered by the PIF motif (**Figure 4**): which executes an inward movement of TM5 at $\underline{P}^{5.50}$, a rotation of TM3 at $\underline{I}^{3.40}$, and an outward movement of TM6 at $\underline{F}^{6.44}$ (Rasmussen *et al.*, 2011). The arrangement of these side chains is transmitted to the intracellular side via the highly conserved NPxxY and DRY motifs, as well as $Y^{5.58}$ (Weis and Kobilka,

2018), so that an intracellular cavity, which is required for the binding of the C-terminal α5 helix of the G-protein, is opened through the outward movement of TMs 5 and 6 (approximately 14Å) (Rasmussen *et al.*, 2011). Due to the high conservation of these amino acids, and despite the structurally diverse type of extracellular signals, the propagation of the signal from the orthosteric binding site to the intracellular amino acids of the TM bundle converge upon structurally conserved mechanisms of effector activation (Venkatakrishnan *et al.*, 2016).

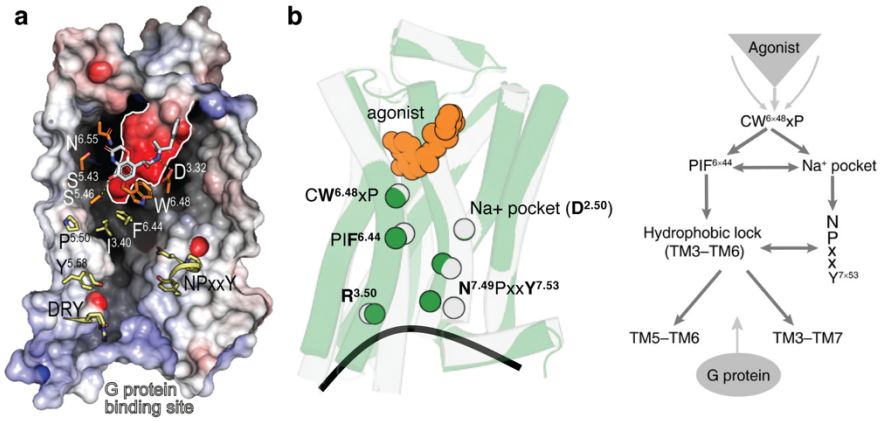


*Figure 4. Schematic view of the details associated with class A GPCR activation. **(a)** Crossection through a prototypical class A GPCR, highlighting the agonist (orange sticks) occupying the orthosteric site (delineated by a white line), the PIF motif located below the orthosteric binding cavity, and the side chains of the highly conserved NPxxY and DRY motifs and $Y^{5.58}$ that transmit the signal from the PIF motif to the G-protein binding site **(b)** Common activation model for class A GPCRs. Residues are shown in circles, conserved contact rearrangements of residue pairs upon activation are denoted by lines. Taken and adapted from (Zhou et al., 2019).*

### 1.1.7 Allosterism and allosteric modulators

Allosterism is defined as "the process by which the binding or/and function of an endogenous or exogenous ligand at one location (the orthosteric site) is influenced by the binding of another ligand or protein at a topographically distinct site (the allosteric site)" (Smith and Milligan, 2010). Ligands that function as allosteric modulators are categorized as negative

(NAM), positive (PAM), or silent (SAM) depending on their ability to decrease, increase, or cause no effect, respectively, on the action (affinity and/or efficacy and/or functional selectivity) of the orthosteric ligand (**Figure 5a**) (Christopoulos, 2014). Ago-PAMs are allosteric modulators than in addition to increasing the potency and/or efficacy of orthosteric agonists, can induce receptor activation by themselves.

The orthosteric binding pocket of related GPCRs is highly conserved, which makes it difficult for drug discovery programs to develop selective compounds (Persechino *et al.*, 2022). Allosteric pockets are less conserved (Persechino *et al.*, 2022; Hedderich *et al.*, 2022), so targeting them is an attractive solution to the selectivity problem.

For class A GPCRs, are several allosteric binding pockets have already been described. As of today, there are 29 structures available in which were the GPCR is co-solved with a modulator, covering an extensive part of its surface (**Figure 5b**). In fact, in a recent computational analysis performed by Hedderich and colleagues they found that almost the entirety surface of the receptor structure was potentially druggable (Hedderich *et al.*, 2022).

One of the most classical allosteric pockets is the extracellular cavity, or vestibule. This area has been involved in the recognition of the orthosteric ligand (Dror et al., 2011; González et al., 2011; Wang, Jiang, et al., 2013), but it can also help tackle the selectivity issue (Newman *et al.*, 2020; Masureel *et al.*, 2018). Additionally, in cases such as this, an orthosteric ligand with an extended moiety towards this vestibule can also be designed (Fronik *et al.*, 2017). These ligands are known as bitopic ligands, and they have been useful, for instance, to tackle the dopamine $D_2/D_3$ receptor selectivity (Kumar *et al.*, 2016).

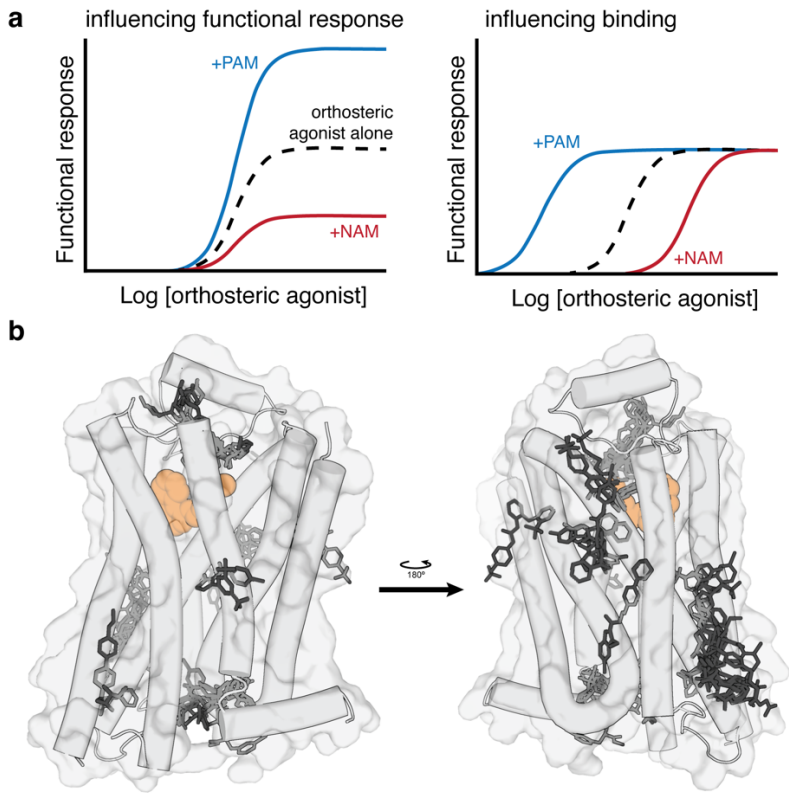


*Figure 5. Allosteric modulation.* ***(a)*** *Functional responses of allosteric modulators. Adapted from (Brogi et al., 2014)* ***(b)*** *The allosteric binding sites and molecules of class A GPCRs, as seen in deposited structures. The orthosteric ligand is shown in orange spheres. The allosteric modulators in black sticks.*

### 1.1.8 The G-protein

G-proteins are heterotrimeric proteins formed by 3 subunits (Gα, Gβ and Gγ). Their mechanism of activation is based on a GDP to GTP exchange in their binding site, located in the Gα subunit (**Figures 1 and 6a,b**). The active state of a GPCR is able to couple a GDP-bound (inactive) G-protein. This interaction will typically induce a GDP to GTP exchange in the Gα subunit, leading to the dissociation of the subunit from the heterotrimeric complex (Syrovatkina *et al.*, 2016) (**Figure 6c**). Now, both Gα and Gβγ will mediate secondary messenger signaling cascades

through activating/inactivating effector proteins (such as adenylyl cyclase, phospholipase, phosphodiesterases, ion channels...) (Hilger, 2021) (see **Figure 1**).

Depending on the family of activated Gα subunit (see above), the intracellular effect will be different, as these stimulate distinct effectors (**Figure 6d**). $G\alpha_s$ activation will lead to activation of adenylyl cyclase (AC) and consequent increase in intracellular cAMP levels. $G\alpha_{i/o}$ activation will have the opposite effect: AC activation will be blocked, and cAMP levels reduced. $G\alpha_q$ activation is related with an increase of the phosphatidyl inositol (IP3) levels and intracellular calcium release through interaction with phospholipase C (PLC). $G\alpha_{12}$ was the last G-protein subtype to be characterized, its role is to regulate a group of Rho guanine nucleotide exchange factors (RhoGEFs) that eventually modulate the RhoA GTPase activity, member of the Ras protein family (Hilger, 2021).

There are structures available for all the four families of G-proteins, in a variety of states including the inactive form, coupled to a receptor, bound to regulatory proteins and inhibitors (https://gproteindb.org/structure/gprot_statistics), and quite recently bound to GTP and the receptor (Papasergi-Scott *et al.*, 2023). The process of G-protein activation upon binding to the receptor is captured by Papasergi-Scott and colleagues using time-resolved cryogenic electron microscopy (Papasergi-Scott *et al.*, 2023). Structural mapping of the α-subunit was re-established by Flock and colleagues based on sequence and structure (Flock *et al.*, 2015) (**Figure 6a,b)**. The α-helical domain of the α-subunit is a highly mobile lobe that opens to allow the exchange of GDP to GTP. Typically, in structures involving a bound receptor, this area is not solved as the flexibility is too high. Only few

structures have been solved in an open state (Rasmussen *et al.*, 2011; Kang *et al.*, 2018; Sun *et al.*, 2021; Xing *et al.*, 2020)).

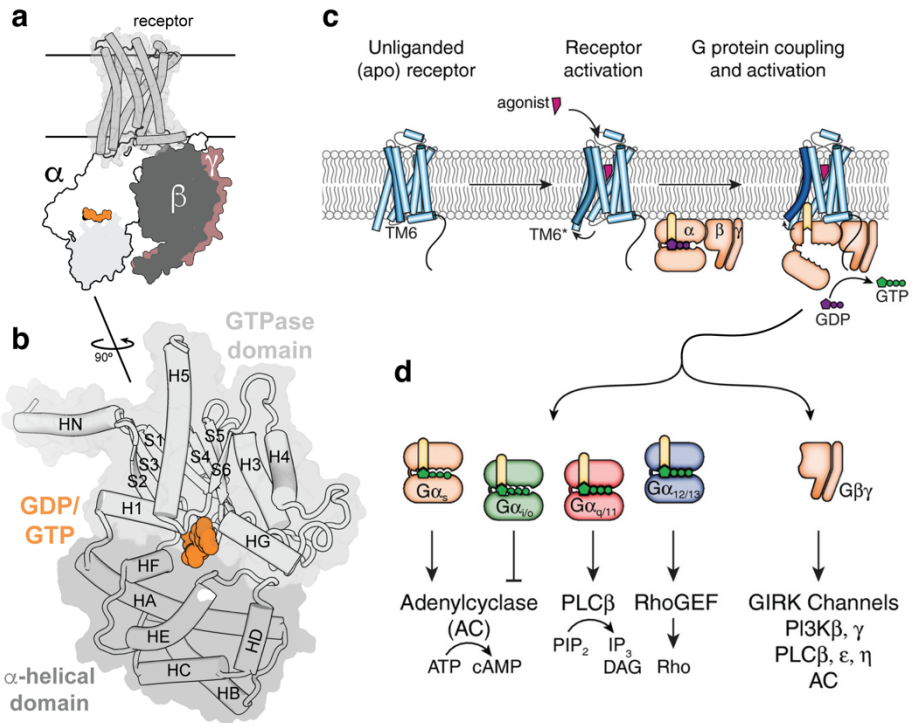


*Figure 6. Signaling of 4 major G-protein subclasses. **(a)** Miniature of the receptor-G-protein complex, and **(b)** close-up to the Gα subunit, with the secondary structure mapping depicted as established by (Flock et al., 2015). **(c)** Schematic simplification of the signaling process and **(d)** the different Gα subtypes and the cascades these trigger, taken from (Hilger, 2021).*

## 1.2 GPCR oligomers

The concept of GPCR oligomerization is highly controversial. The first evidence of class A GPCRs interacting in the membrane dates to 1975, when the group of Lefkowitz identified negative cooperativity between the orthosteric binding sites of $\beta_2$AR, only explainable if the two receptors were interacting (Limbird *et al.*, 1975). Additional evidence of dimeric complexes of $\beta_2$AR was found in 1982 (Fraser and Venter, 1982), , followed by a handful of other receptors in the following decades

(Rodríguez-Frade *et al.*, 1999; Bai *et al.*, 1998; Ng *et al.*, 1996; Capponi and Catt, 1980). Higher-order oligomer formations were proposed for the TSH receptor (Gennick *et al.*, 1987), and *in vivo*, in mouse brain slices, involving $A_{2A}R$ and $D_2R$ heteromers (Ferré *et al.*, 1992).

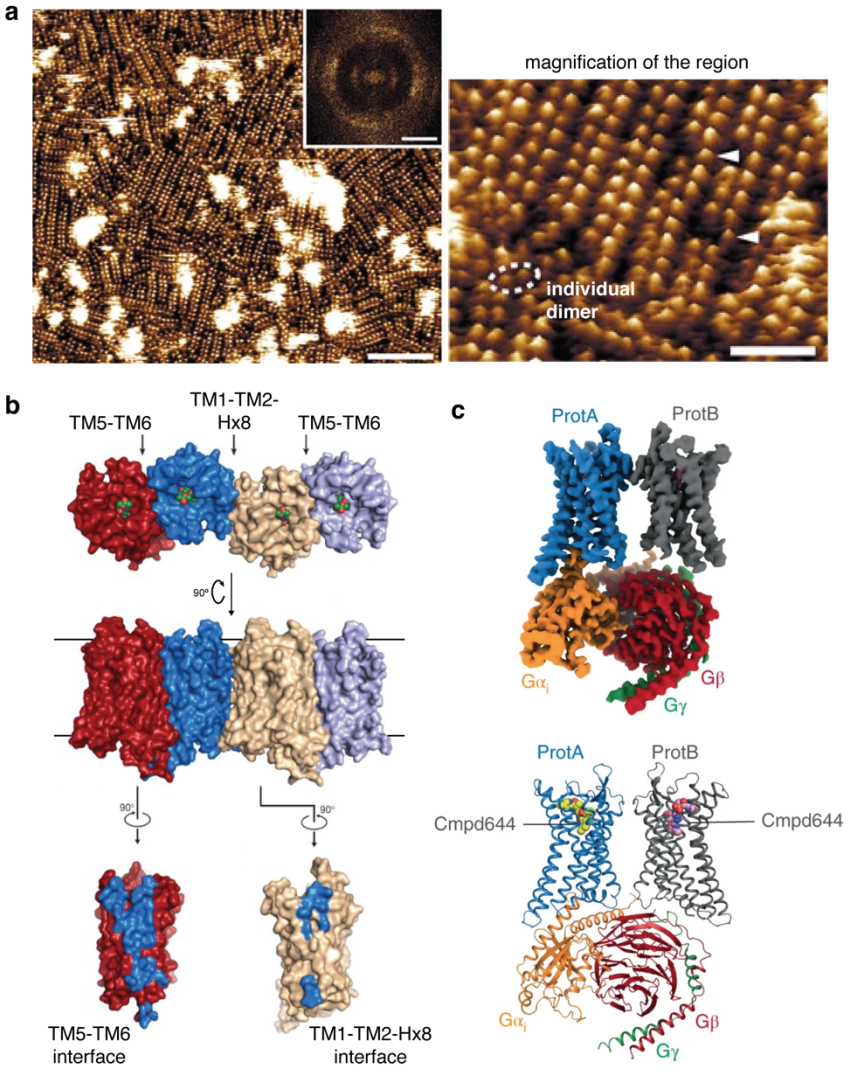


*Figure 7. Molecular structures of GPCR homomers.* ***(a)*** *Organization and topography of the cytoplasmic surface of rhodopsin. Taken from (Fotiadis et al., 2003).* ***(b)*** *The μ-opioid receptor oligomeric arrangement. Adapted from (Manglik et al., 2012).* ***(c)*** *Cryo-EM map and atomic model of dimeric apelin receptor in complex with a Gi heterotrimer. Adapted from (Yue et al., 2022).*

Additional confirmation of on the formation of these complexes were obtained by fluorescence and bioluminescence techniques by several groups (see METHODS, *Experimental methods*). Overton and Blumer provided *in vivo* evidence of GPCR oligomers in 2000 (Overton & Blumer, 2000). Since then, many studies have provided evidence of GPCR interactions using such techniques (reviewed in (Ciruela *et al.*, 2010)). The lack of demonstration of GPCR oligomers in native tissues was an important caveat (Ferré *et al.*, 2009; Pin *et al.*, 2007), until Albizu and authors used time-resolved fluorescence resonance energy transfer between GPCR ligands to reveal oligomers in native tissues (Albizu *et al.*, 2010).

The first physical observation of GPCR oligomerization at the atomic level was observed in rhodopsin aggregates in native disk membranes, by atomic-force microscopy, whose minimal unit was a dimer (**Figure 7a**) (Fotiadis *et al.*, 2003). Among the obtained GPCR structures, by X-ray crystallography or cryo-EM, the following contacts between protomers must be highlighted (described in chronological order). (i) The structure of the chemokine receptor 4 (CXCR4) that shows a homodimer with an interface including TM5 and TM6 (Wu *et al.*, 2010). (ii) The structure of MOR (**Figure 7b**) that shows receptor protomers associated into pairs through two different interfaces (Manglik *et al.*, 2012). The first is via TM1, TM2 and Hx8 and the second interface is comprised of TM5 and TM6 (hereby referred to as the TM 5/6 interface). (iii) The structure of the turkey $\beta_1$-adrenergic receptor that also displays two dimer interfaces (Huang *et al.*, 2013). One interface also involves TM1, TM2 and Hx8, as previously described in the MOR. In contrast, the other interface engages residues from TM4, TM5 and ICL2 (TM 4/5 interface). (iv) The structure of $A_1R$ that reveals an interface including TM4, TM5, ICL2, and the helix of ECL2

(Glukhova *et al.*, 2017). (v) The cryo-EM structures of a full length mGlu5 receptor in the apo inactive/open and active/closed conformations (Koehl *et al.*, 2019), which showed that activation leads to compacting of the mGlu5 dimer, enabling the 7TM domains to reposition closer, via a TM6–TM6 interface. (vi) Other class C (Papasergi-Scott *et al.*, 2020; Du *et al.*, 2021) and class D (not expressed in humans) (Velazhahan *et al.*, 2021) homo- and hetero-dimers were obtained by cryo-EM. And (vii) the apelin receptor-G-protein complex in a 2:1 stoichiometric ratio was solved in 2022 (Yue *et al.*, 2022) (**Figure 7c**), demonstrating the allosteric effect of one protomer over its counterpart by mutagenesis.

Owing to the high number of GPCRs, roughly ~800 (~350 for nonsensory GPCRs), the probability for casual, nonfunctional, heteromer formation is very high. This, however, contrasts with the specificity of the interactions, namely not all GPCRs interact with each other, only few of them. As of today, no specific rules have been described to predict whether two given GPCRs form heterodimers. An online tool (http://www.gpcr-hetnet.com/) reports both experimentally determined interactions within the GPCR superfamily, as well as noninteracting GPCRs that may serve as negative controls (Borroto-Escuela *et al.*, 2014).

### 1.2.1 GPCR heteromers and allosterism

The term “heteromer” is defined as “a macromolecular complex composed of at least two (functional) receptor units (protomers) with biochemical properties that are demonstrably different from those of its individual components” (Ferré *et al.*, 2009). Depending on their counterpart, GPCRs can form homomers (if both protomers are identical) or heteromers (if they are different) (Ferré *et al.*, 2009).

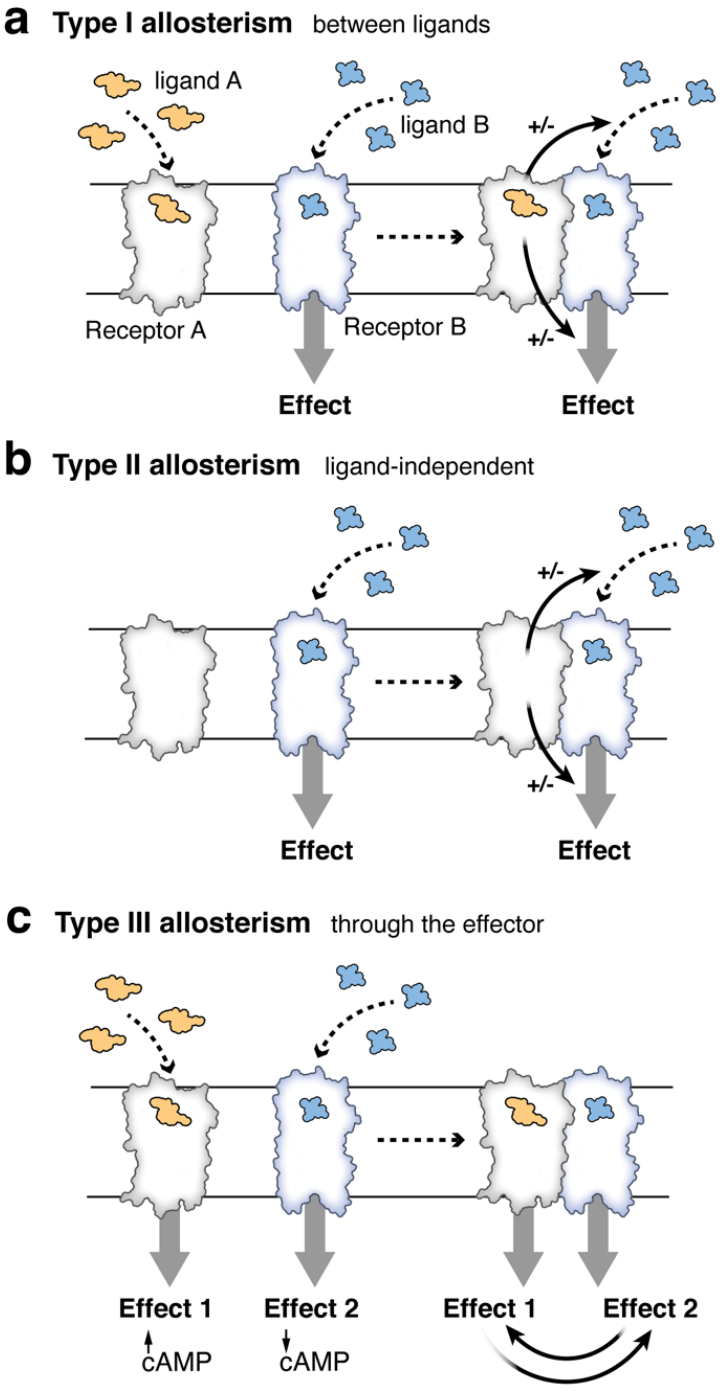


*(Figure legend on next page)*

*Figure 8. Allosterism in GPCR heteromers. (a) Type I allosterism, in which a ligand (in orange) binding to one protomer (gray contour) can modify the affinity (ligand binding depicted by the gray broken arrow) or the efficacy (receptor activation depicted by the wide gray arrow) of another ligand (in blue) binding to the partner receptor (blue contour). (b) Type II allosterism, or ligand-independent allosterism, in which the affinity (gray broken arrow) or efficacy (wide gray arrow) of a ligand (in blue) for a GPCR (blue contour) can be modified just by heteromerization with a molecularly different GPCR (gray contour). (c) Type III allosterism, or allosterism through the effector, by which activation of a Gi-coupled receptor leads to inhibition of cAMP formation upon activation of a Gs-coupled receptor.*

Receptor oligomerization can influence receptor signaling (Gomes *et al.*, 2016). As defined above, allosterism can happen between a molecule and a protein or between a protein and another protein. In fact, the first experimental observations of allosterism were from proteins that exhibited cooperative behavior due to an oligomeric architecture (Changeux and Edelstein, 2005). Thus, it can be assumed that allosteric interactions will constitute a common property of GPCR heteromers (Ferré *et al.*, 2020, 2014, 2009). In a recent review (Ferré *et al.*, 2022), three types of allosterism were described for GPCR heteromers (**Figure 8**).

**Type I allosterism or allosterism between ligands**

Type I allosterism entails the ability of an orthosteric ligand of one protomer to modify the functional properties (affinity and/or efficacy) of a different orthosteric ligand of another molecularly distinct protomer via the TM helices of the heteromer (**Figure 8a**). GPCRs are dynamic proteins that permit rapid small-scale structural fluctuations (Nygaard *et al.*, 2013). Thus, one protomer can modify the position of the amino acids of the orthosteric binding site involved in ligand binding and, therefore, the binding affinity; or/and modify the amino acids that transmit the signal from the PIF motif to the G-protein site, and therefore ligand efficacy, of the partner receptor through the protein-protein transmembrane interface (Ferré *et al.*, 2022). This modulation, named cross-talk, can be positive (+) or negative (-), depending whether the effect increases or decreases,

respectively, the functional properties of the second agonist. Similarly, antagonist binding to one protomer might block (cross-antagonism) or facilitate (cross-agonism) agonist-induced activation of the partner receptor. In cross-antagonism, antagonist binding to one protomer triggers the interaction with TM6 of the partner protomer, blocking the opening of the intracellular cavity for G-protein binding. In cross-agonism, antagonist binding to one protomer disrupts the interaction with TM6 of the partner protomer, facilitating the opening of the intracellular cavity for G-protein binding.

**Type II allosterism or ligand-independent allosterism**

Type II allosterism, or ligand-independent allosterism, occurs when the functional properties of a ligand for a given GPCR can be modified just by heteromerization (**Figure 8b**). The mechanisms of +/- cross-talk are as in type I allosterism.

**Type III allosterism or allosterism through the effector**

In this case the effector (e. g., adenylyl cyclase) acts as a mediator for the cross-influence observed between the two protomers of the heterodimer. Of special functional significance are those heteromers constituted by one homodimer coupled to a Gs protein and another different homodimer coupled to a Gi protein, a GPCR heterotetramer. In this case activation of a Gi-coupled receptor leads to inhibition of cAMP formation upon activation of a Gs-coupled receptor (canonical Gs-Gi antagonist interaction at the AC level), without modifying the intracellular values of cAMP at despite the activation of both receptors.

# 2 OBJECTIVES

The global objective of this thesis is to understand the molecular mechanisms of how GPCR (hetero)oligomerization influences the physiological role of receptors and their use as therapeutic targets, using complementary computational and experimental (performed by others, see below) techniques. The explored molecular mechanisms are summarized in **Figure 1**.

We aim to understand how ligand binding to one protomer increases (+) o decreases (-) receptor heteromerization (**Figure 1a**). We have used as a model heteromer the complex between adenosine $A_{2A}$-dopamine $D_2$ receptor and different antipsychotic drugs as ligands (Case Study #1).

2. We aim to understand how receptor oligomerization influences the binding affinity of/and efficacy of the orthosteric agonist bound to the partner receptor (**Figure 1b**). We have used a model heteromer the complex between galanin $Gal_1$ receptor (Gal1R) and the μ-opioid receptor (MOR). The main aim is to understand how heteromerization of MOR with Gal1R decreases (-) binding affinity and efficacy of (S)-methadone, but not (R)-methadone (Case Study #2).

3. We aim to understand how antagonist binding to one protomer blocks agonist-induced activation of the partner receptor (cross-antagonism) (**Figure 1c**). We have studied the ability of the selective dopamine $D_3$ receptor ($D_3R$) antagonist PG01034 to block SKF81297-induced dopamine $D_1$ receptor activation (Case Study #5).

4. We aim to understand how heteromerization alters the receptor G-protein selectivity pattern (i.e. the recruitment of different G-protein at the interacting protomer) (**Figure 1d**). We have studied the ability of Gal1R to signal through non-canonical Gs coupling rather than canonical Gi/o coupling in the MOR-Gal1R heteromer (Case Study #3), and 5-$HT_{2A}$R

signal through non-canonical Gi/o coupling rather than canonical Gq/11 coupling in the $CB_1R$-5-$HT_{2A}R$ heteromer (Case Study #4).

5. We aim to understand how receptor heteromerization biases agonists to activate the β-arrestin signaling cascade of the partner receptor (**Figure 1e**). We have used structurally similar phenylpiperazine derivatives with different pharmacological profile at the $D_1R$-$D_3R$ heteromer (Case Study #5).

This research has been performed by combining structural bioinformatics, molecular dynamics and data-mining of structure and sequence databases with experimental results from site-directed mutagenesis, functional assays and biophysical techniques. It is important to note that chemical synthesis, chemical biology, and *in vitro* and *in vivo* evaluation has been performed by others listed in the original publications.

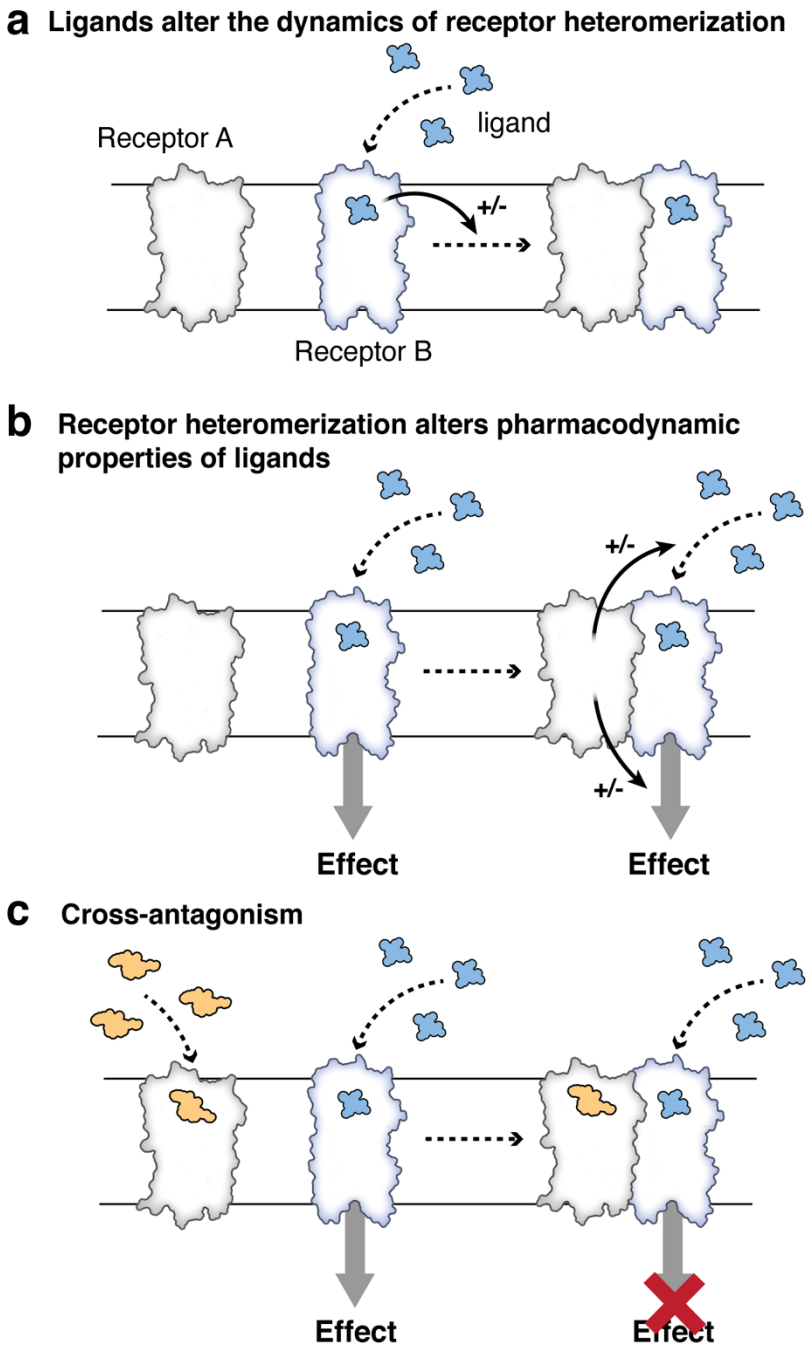
a Ligands alter the dynamics of receptor heteromerization
Receptor A
ligand
+/-
Receptor B
b Receptor heteromerization alters pharmacodynamic properties of ligands
+/-
+/-
Effect
Effect
c Cross-antagonism
Effect
Effect

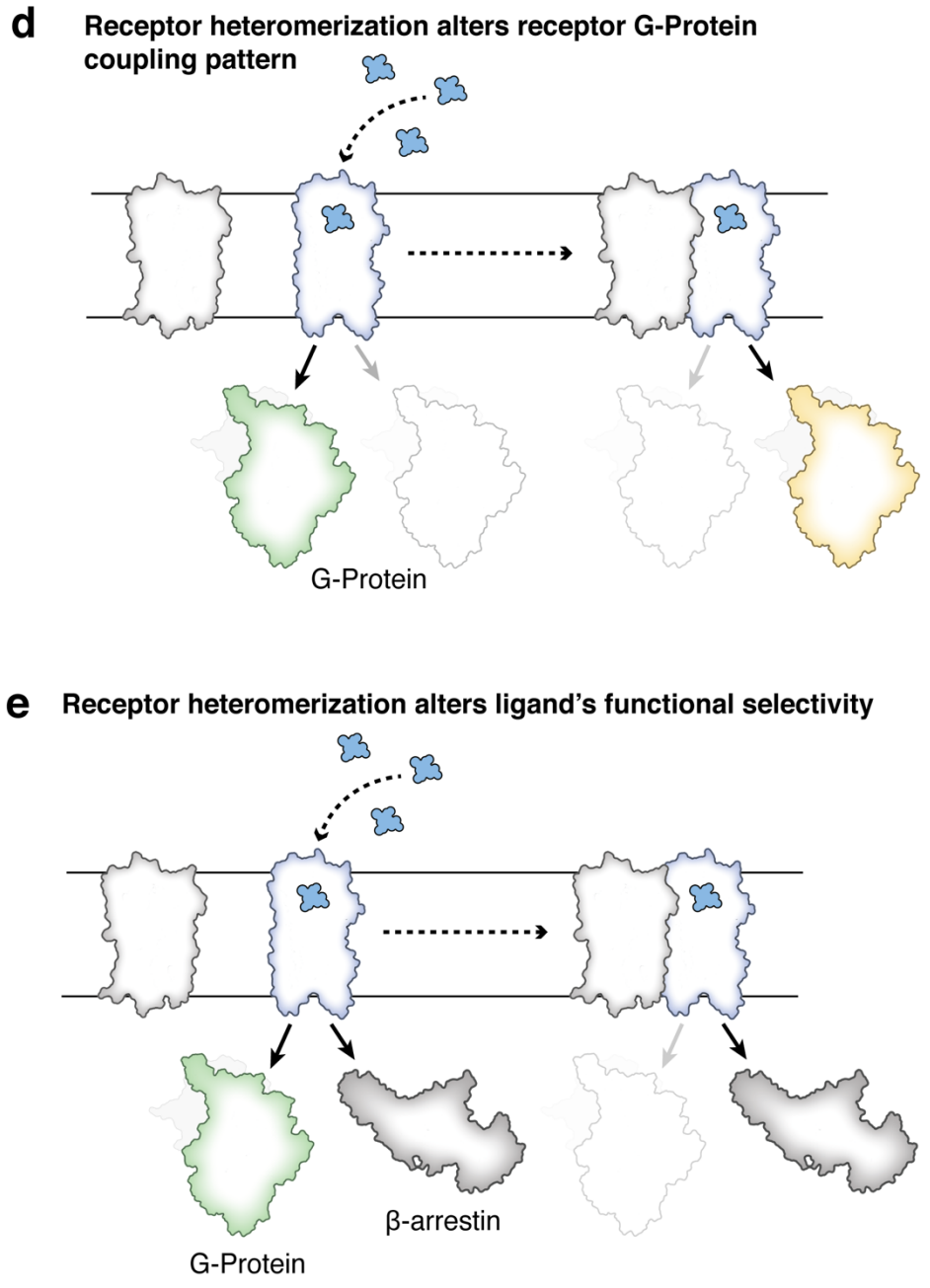


*Figure 1. Allosteric mechanisms for the modulation of GPCR heteromers studied in this thesis.*

# 3 METHODS

The first low resolution structure of a GPCR was the projection structure of rhodopsin in 1993 (Schertler *et al.*, 1993), which could provide a 9 Å resolution three-dimensional structure of rhodopsin in 1995 (Unger and Schertler, 1995). The crystal structure of rhodopsin at 2.8 Å resolution was finally released in 2000 (Palczewski *et al.*, 2000). However, it was not until the year 2007 that the crystal structure of the $\beta_2$-adrenergic receptor bound to the partial inverse agonist carazolol at 2.4 Å resolution was published (Cherezov *et al.*, 2007; Rosenbaum *et al.*, 2007). This significant breakthrough and thanks to the significant advances in crystallization of GPCRs (Serrano-Vega *et al.*, 2008; Day *et al.*, 2007), together with cryogenic electron microscopy (cryo-EM) (Callaway, 2015; Renaud *et al.*, 2018) have permitted to elucidate the structures of many GPCRs (Munk *et al.*, 2016). Today, there are more than 1000 GPCR structures (https://gpcrdb.org/structure/statistics) deposited in the Protein Data Bank (PDB). We now know structures of classes A (Palczewski *et al.*, 2000), B (Siu *et al.*, 2013), C (Koehl *et al.*, 2019), and F (Wang, Wu, *et al.*, 2013), bound to either agonists, antagonists, inverse agonists, or allosteric modulators (Rosenbaum *et al.*, 2007; Rasmussen *et al.*, 2011; Kruse *et al.*, 2013), in the form of monomers or homo-oligomers (Manglik *et al.*, 2012; Huang *et al.*, 2013), in complex with G-proteins (Zhuang *et al.*, 2020; Xing *et al.*, 2020; Zhang *et al.*, 2017; Krishna Kumar *et al.*, 2019; Rasmussen *et al.*, 2011), visual (Kang *et al.*, 2015) or β- (Huang *et al.*, 2020) arrestins, or GRK5 (Chen *et al.*, 2021).

Despite this vast amount of structural information on GPCRs, there are always key structural parts of the system of interest that are unknown and must be modelled by computational techniques (i.e., extracellular or/and intracellular loops or/and the N- and C- terminus). GPCRs are dynamic proteins that permit structural fluctuations to adopt several conformations,

in which the TM helices and the extracellular and intracellular domains change, ranging from inactive to active states. In addition, the state(s) of the receptor that we might want to study may not be resolved experimentally. Ligands or coupling G-proteins bind preferentially to specific state(s), increasing the proportion of those states. Therefore, if the structure of the ligand(s) under study is(are) not resolved in its(their) binding mode to the receptor, we must model the complex computationally. Similarly, the active form of the receptor can bind to G-proteins, arrestins or GRKs, and if the structure of the complex of interest is not known, it must be computationally obtained.

In the following sections, we describe the methods, both computational and experimental (performed by others), employed in the thesis to characterize the ligand-receptor-effector systems of interest.

## 3.1 Homology modeling

This technique predicts the unknown structure of a *target* receptor by using the known structure of a homologous *template* receptor. We have used for homology modeling of the systems of interest two different techniques. First, and more traditional, MODELLER software (Eswar *et al.*, 2006; Martí-Renom *et al.*, 2000) approximates the structure of a *target* providing a sequence alignment and the *template* structure(s) file(s). MODELLER predicts the *target* structure by optimally satisfying spatial restraints derived from the alignment and expressed as probability density functions for the features restrained (Šali and Blundell, 1993). MODELLER can also model missing loops (Fiser *et al.*, 2000). The second tool, and probably one of the biggest breakthroughs in science in the recent years, is AlphaFold2 (Jumper *et al.*, 2021), an artificial intelligence fed on the pairs of sequence-structure data available, with excellent performances. In the case of GPCRs, because the receptors can have different conformations, AlphaFold2 is biased towards the active state since there is an actual bias in the information available (around 60% of the structures are in the active or active-like state, https://gpcrdb.org/structure/statistics). However, for globular proteins, and for completing the missing parts of the sequence, it can be very effective. The standard homology modeling workflow is shown in **Figure 1**.

All the receptors involved in this thesis had at least one structure solved, however some situations required homology modeling. Mainly, ECLs of $D_1R$ (see below) and the inactive conformation of Gal1R. The stability of these predicted structural models was assessed by molecular dynamics (MD) simulations (see below).

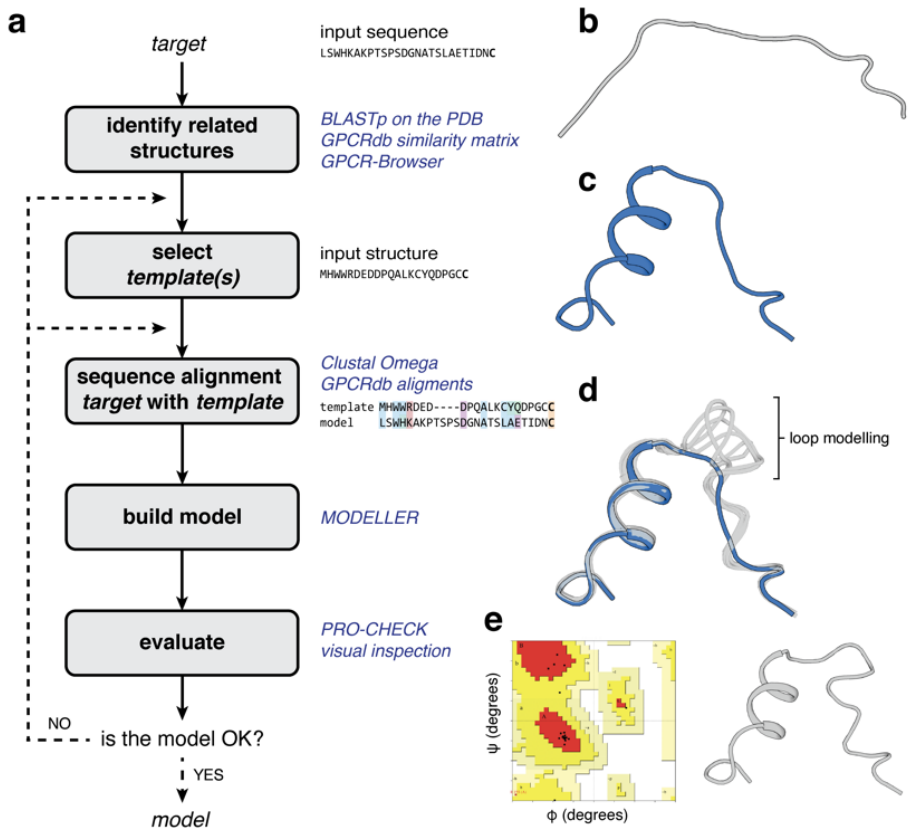


*Figure 1. General workflow to perform homology modeling.* ***(a)*** *The steps followed are shown on the right, and on the left examples and the software used (in blue italics). The protocol begins with the identification of homology related structures, which can be obtained with the help of a rather classical method like a protein BLAST (BLASTp) against the PDB database (Altschul et al., 1990), or a more specific method for GPCRs like the GPCRdb service (Munk et al., 2016) or the GPCR-Browser (http://lmc.uab.cat/ghm/). From the related structures, the template or templates are usually selected based on the structure quality (e. g. resolution) and the adequacy to the structure aimed to be modelled (e.g. in GPCRs, if it is the right activation state, similarity of the orthosteric binding pocket, etc). Once the templates are selected, these must be aligned to the target sequence, using Clustal Omega (Sievers et al., 2011) (typically for multiple sequence alignments) or GPCRdb (Kooistra et al., 2021) (more focused to GPCRs), and manually refined. These two steps are crucial for a building a proper model and have to be carefully curated and iterated if the model is insufficient. MODELLER (Eswar et al., 2006; Martí-Renom et al., 2000) is fed with the sequence alignment and the template structures, and provides a series of model candidates, that can then be evaluated by visual inspection and using webservers like PRO-CHECK (Laskowski et al., 1993). Schematic representation of* ***(b)*** *an unstructured target sequence,* ***(c)*** *the template structure,* ***(d)*** *the retrieved models by MODELLER superposed to the template structure and* ***(e)*** *the Ramachadran outliers plots as calculated by PRO-CHECK and the final selected model.*

## 3.2 Docking

Ligands with unknown experimental binding mode were docked into the receptor orthosteric binding site using AutoDock (Eberhardt *et al.*, 2021) or the docking facility in the Molecular Operating Environment (MOE) software (Chemical Computing Group Inc., Montreal, Quebec, Canada). One hundred docking solutions per ligand were generated, the top-ranking solutions were visually inspected, and conformations that matched with the structure-activity relationships of the orthosteric pocket were selected for MD simulations (see below).

Blind docking is used when the binding site of a ligand in the target protein is not known (Hassan *et al.*, 2017; Heté Nyi and Van Der Spoel, 2002). HPEPDOCK (Hierarchical flexible Peptide Docking approach) (Zhou, Li, *et al.*, 2018) was used to study the putative interaction of the last 23 residues of the $CB_1R$ C-terminus of $CB_1R$ onto the α-subunit of the G-protein. The stability of the docking poses was explored using MD simulations (see below).

## 3.3 Building dimers

It is not possible to establish beforehand the domain(s) (TMs, ICLs, ECLs, or/and C-terminal) of two interacting GPCRs that contribute to the formation of the homo/heterodimer. In other words, the receptor interface at which the monomer-monomer interactions occur cannot be predicted by either sequence analysis or computer simulations. Experimentally, the use of synthetic peptides with the sequence of TM domains of the receptor, fused to cell-penetrating peptides (Milletti, 2012; Guidotti *et al.*, 2017), to disrupt bimolecular fluorescence complementation (BiFC) signals (see the *Experimental studies* section), has been a very valuable

tool to predict contacts between TM domains of interacting GPCRs. Once the interface is known, a template to model the dimeric complex can be retrieved from the available structures. Apart from the cryo-EM structures of receptor dimeric complexes (see INTRODUCTION), there are also crystallographic structures of GPCRs that present possible (homo)dimeric interfaces. Whether these interfaces are real or due to crystal packing is still controversial (Stenkamp et al., 2018), however, these structures can still be used as templates.

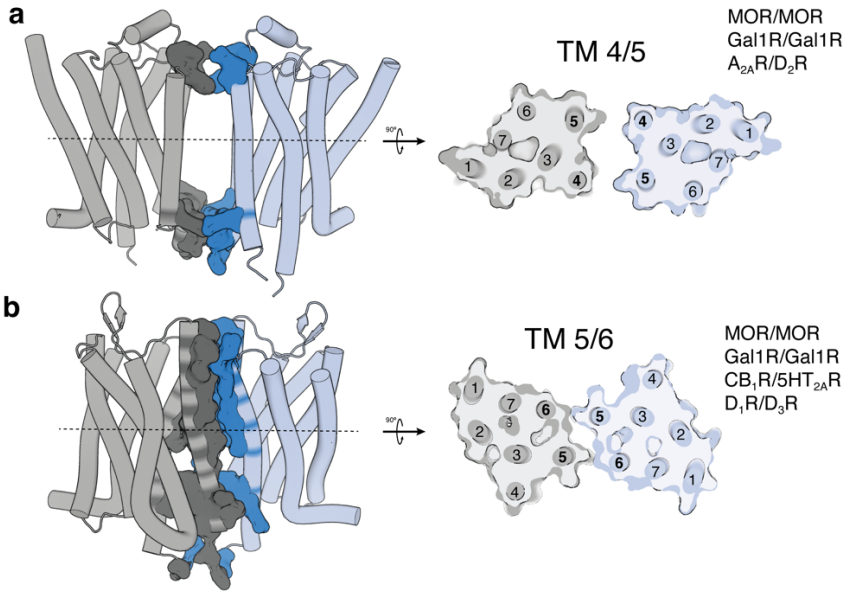


*Figure 2. Templates used for the dimers built in this thesis. Representations of* ***(a)*** *the TM4/5 interface as observed in the crystal structure of the* $\beta_1$*AR in a dimeric state (Huang et al., 2013), and* ***(b)*** *the TM5/6 interface as observed in the crystal structure of the MOR bound to a morphinan antagonist (Manglik et al., 2012).The dimeric structures are presented in two orientations: sideview from the membrane plane and up from the extracellular site, where receptors are shown as slices. Next to the sliced view are indicated the homo- and heterodimers built using each of these structures as templates.*

Based on the experimental results, all the dimers studied in this thesis displayed a symmetrical disposition and involved either a TM4 and TM5 (TM 4/5) interface or TM5 and TM6 (TM5/6) interface. Both interfaces have been found in crystal structures and the possibility of an oligomeric

interaction is studied in the original publication (Manglik *et al.*, 2012; Huang *et al.*, 2013). The general protocol used in this thesis is *i*) align the receptors of interest with the template, *ii*) removal of clashes or structural hindrances by visual inspection, *iii*) energy minimization, and *iv*) MD simulations (see below).

**Figures 2a,b** show the different heteromers studied in this thesis and the molecular models built via the TM 4/5 dimeric interface of the $\beta_1$-adrenergic receptor (PDB code 4GPO) (Huang *et al.*, 2013) or via the TM 5/6 interface of the MOR structure (4DKL) (Manglik *et al.*, 2012).

## 3.4 Molecular Dynamics (MD) simulations

The structure of a protein still has its limitations since proteins are dynamic systems (Henzler-Wildman and Kern, 2007). NMR studies, spectroscopy, fluorescence-based techniques or novel cryoEM approaches have attempted to capture dynamic events (Shimada *et al.*, 2018; Lerner *et al.*, 2021), but either the size of the system or the time resolution still pose a challenge (Henzler-Wildman and Kern, 2007). To fill in those gaps, computational modeling can make use of techniques like Molecular Dynamics (MD). This technique can predict the movement of atoms with picosecond resolution and for systems of hundreds of kilodaltons (Karplus and Petsko, 1990; Karplus and McCammon, 2002).

MD has achieved significant contributions to study structure-function relationships of GPCRs (Latorraca *et al.*, 2017). In general, MD simulations consist in a discrete atomistic representation of thousands or millions of atoms that form the system formed by the ligand, the GPCR monomer, dimer, or tetramer of interest, the intracellular effector, the surrounding lipid bilayer, and the water environment. The force that the

system exerts on each atom is computed in a succession of short time steps, so the position and velocity of them are updated according to Newton's laws of motion at each time step. The integration of Newton's equations is performed successively along time intervals using specific algorithms, such as leap-frog or Verlet scheme. The selection of the time interval is crucial for the stability of the system, which typically is around 1 to 2 fs.

### 3.4.1 Force-field

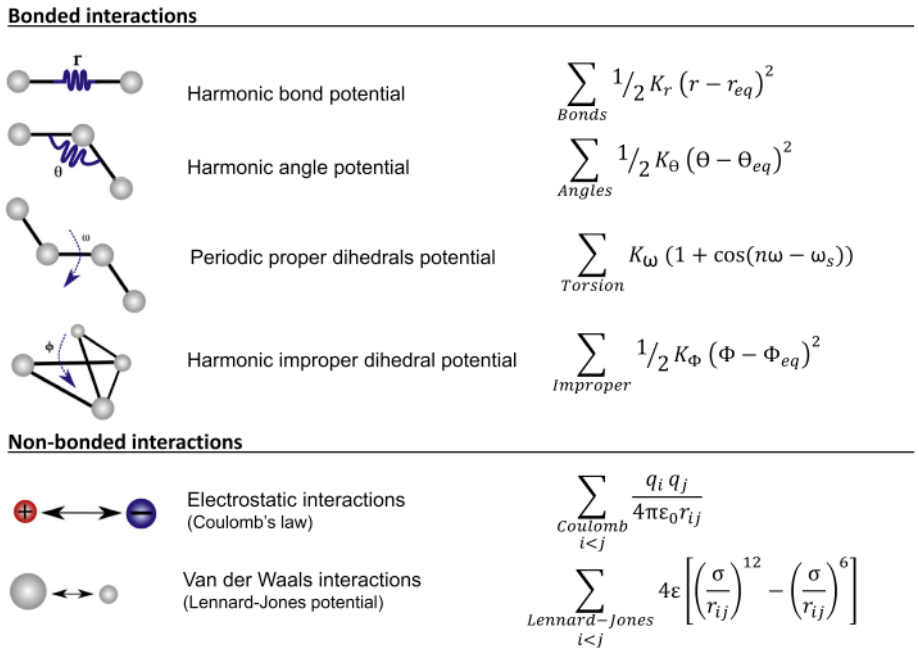


***Figure 3. Energetic terms of the potential energy function applied in a classical MD force-field.*** *A schematic representation of bonded and non-bonded interactions is depicted on the left. The energy equations associated with each interaction type are depicted on the right. Figure taken from (Aranda-Garcia et al., 2022).*

Atomistic, molecular mechanics or force-field simulations model the system accounting for atom nuclei explicitly. The simulation calculates the energy of a system according to the positions of the atoms, based on a

force-field. A force-field contains the interaction function and parameters used to determine the potential energy (V) of a system. A typical force-field function is usually divided in bonded ($V^{bonds} + V^{angles} + V^{torsion} + V^{improper}$) and non-bonded terms ($V^{van\ der\ Waals} + V^{electrostatics}$) terms (see **Figure 3**).

For the MD simulations performed in this thesis, the *amber14sb* library (Maier *et al.*, 2015) was used for protein and ions, a GROMACS adaptation of *lipid14* (Dickson *et al.*, 2014) for lipids, *TIP3P* (Jorgensen *et al.*, 1983) for water, and the general Amber force field (*GAFF2*) (He *et al.*, 2020) with HF/6-31G*-derived restrained electrostatic potential (RESP) atomic charges for ligands (Bayly *et al.*, 1993).

### 3.4.2 Preparing a system for MD

In all structures, fusion proteins were removed, stabilizing mutations were mutated to the native sequence, protonation states were assigned with the PDB 2PQR tool (Dolinsky *et al.*, 2004) using PROPKA to predict the pKa values of ionizable groups in the proteins at pH 6.5 (Søndergaard *et al.*, 2011), disulfide bonds between cysteines were built using the tleap module of Ambertools19, and highly conserved internal water molecules were added using HomolWat (Mayol *et al.*, 2020).

Membrane systems were built with PACKMOL-Memgen (Schott-Verdugo and Gohlke, 2019). The software embeds the ligand, the GPCR oligomer, and the intracellular effector into a lipid bilayer box containing 1-palmitoyl-2-oleoyl-sn-glycero-3-phosphatidylcholine (POPC), cholesterol (CHL), water molecules and monoatomic Na+ and Cl- ions (0.15 M). Globular protein systems were embedded in a water dodecahedron box (to optimize the system size) built with GROMACS (Abraham *et al.*, 2015).

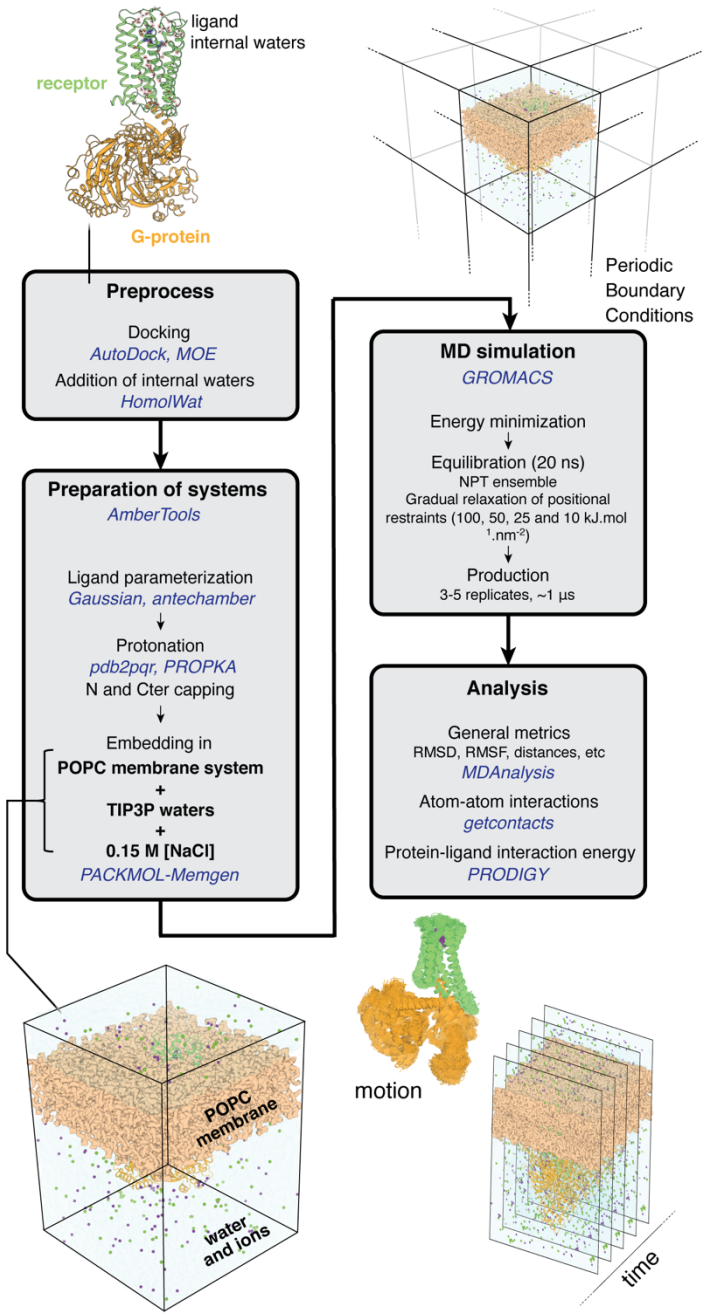


*Figure 4. Workflow of the unbiased all-atom MD simulations protocol. The software used in each step is depicted in blue italics, as it is mentioned along the lines in the text.*

### 3.4.3 MD protocol

MD simulations explore the system conformations at a microscopic level based on macroscopic properties (thermodynamic properties). Thus, the system (box, as represented in **Figure 4**) must be subjected to specific thermodynamic conditions, defined by the macroscopic ensembles. The most common ensembles are the NVT or canonical ensemble (constant number of atoms N, volume V and temperature T) and the NPT or isothermal-isobaric ensemble (constant number of atoms N, pressure P and temperature T). To maintain the specified conditions, the so-called coupling thermostats and barostats are employed. An NVT ensemble is not suitable for a membrane system, because the dimensions of the box are determined by the area and the length per lipid, which are variable and not well characterized (Berger *et al.*, 1997). Only the NPT ensemble is hence suitable for simulations involving a lipid bilayer, and the pressure coupling must be different on the X,Y axis from the Z axis (semi-isotropic or anisotropic). Moreover, to avoid problems with boundary effects caused by the finite size of the box, periodic boundary conditions (PBC) must be used.

The initial system does not fulfill the required thermodynamic conditions. Equilibration ensures that the system's thermodynamic properties like temperature, pressure, volume, density, and number of atoms are stable. The standard protocol follows a two-phase equilibration process with NVT plus NPT ensembles. The NPT equilibration phase for globular proteins consisted in three steps in which restraints on the protein and peptide were reduced progressively to allow for accommodation of the molecules prior to MD. In the case of membrane systems, the protocol consisted in a six step NPT equilibration (10 ns + 5 ns + 2 ns + 2 ns + 2 ns + 2 ns). In

the first step, the whole system was fixed except hydrogen atoms. In the second step, the protein loops were released from restraints. In the final four steps, the restraints on the ligand and α-carbon atoms of the protein were relaxed from 1000, 400, 25 to 10 kJ $mol^{-1}$ $nm^{-2}$, respectively. At the same time, the phosphate group of the POPC molecules was also restrained and progressively released only in the Z axis, which is a standard action taken to avoid artifacts in the membrane.

After equilibration, unrestrained MD simulation (several replicas between 0.5-1 μs) are produced at a constant temperature of 300 K, using separate v-rescale thermostats for the receptor, ligands lipids and solvent molecules. A time step of 2.0 fs was used for the integration of equations of motions. All bonds and angles were kept frozen using the LINCS algorithms. Lennard-Jones interactions were computed using a cutoff of 10 Å, and the electrostatic interactions were treated using PME with the same real-space cutoff under periodic boundary conditions. The MD software used for all the simulations presented in this thesis is GROMACS (Abraham *et al.*, 2015). **Figure 4** shows a schematic view of the MD protocol.

### 3.4.4 Analysis of the simulations

Analysis of the MD trajectories is performed by monitoring interatomic distances, angles, dihedrals, and root-mean square deviation (RMSD) or fluctuation (RMSF). RMSD is measured between the positions of the selection of interest (e.g. Cα atoms) at frame *n* and *n-1*, thus, a time evolution can be computed. RMSF instead measures the average displacement of each element in the selection (e.g. each Cα atom) to its average position along the simulation. Both quantities are usually indicative of stability in the trajectory. All these variables were monitored

with the python package MDAnalysis (Michaud-Agrawal *et al.*, 2011; Gowers *et al.*, 2016). The analysis of non-covalent interactions was performed with the python package getcontacts (https://getcontacts.github.io/) and interaction energies were calculated with PRODIGY (Protein binding energy prediction) (Vangone and Bonvin, 2015). Typically, these packages use adaptations of the most frequent non-covalent interactions found in nature (**Figure 5**).

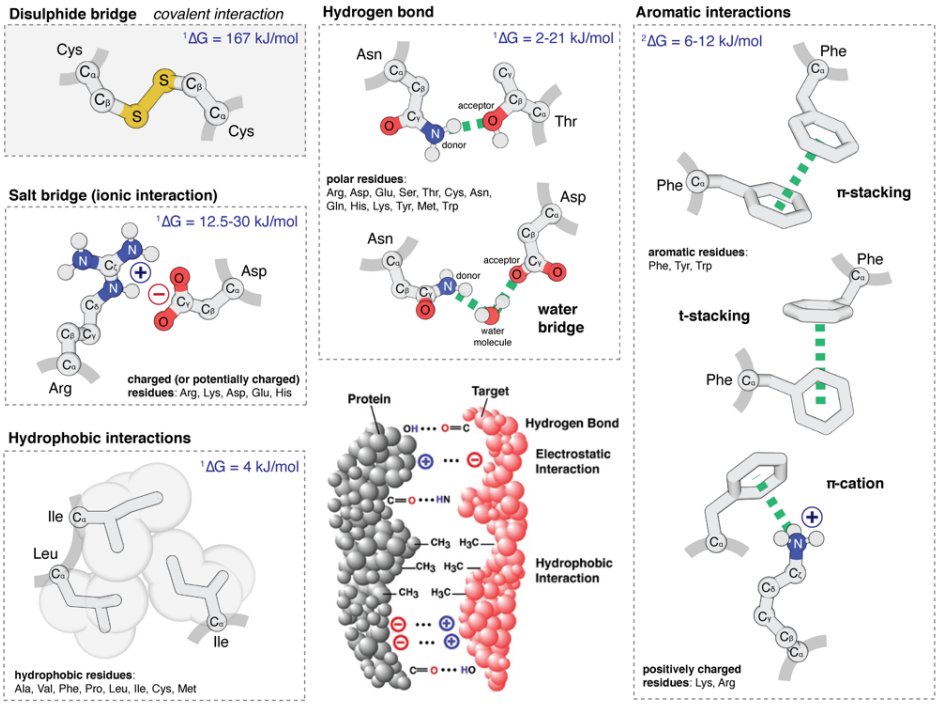


*Figure 5. Most common non-covalent (and covalent) interactions. The affinity (strength) of a protein-protein or protein-ligand interaction will depend to a high extent on the number and type of non-covalent interactions. Non-covalent bonds involve salt bridges (or ionic bonds), hydrogen bonds, aromatic interactions and hydrophobic effects. Disulphide bridges (a covalent bond) can happen between protomers as well. For a protein-protein or ligand-protein interaction to be tight there has to be both a shape and electrostatic complementarity (as it is shown in the middle lower pane, taken from (Hoshino et al., 2014)).*

## 3.5 Modeling the dopamine $D_1$ receptor

The structure of the dopamine $D_1$ receptor ($D_1R$) has been solved by both X-ray and cryo-EM in the active conformation bound to Gs. We are interested in the inactive conformation of $D_1R$, thus we exemplify sections 1.1, 1.2, and 1.4 in modeling the inactive conformation of $D_1R$. ECL2 is not solved in any of the available structures of $D_1R$ and is usually a key region of the structure (Wheatley *et al.*, 2012). The best template for ECL2 was the $\beta_1$ adrenergic receptor ($\beta_1AR$) (**Figure 6a**). However, it was unclear if that was the right configuration for the loop, and 1 $\mu$s of unbiased MD was performed to check for the potential configurations of the same, obtaining a stable one in the last 150 ns (**Figure 6b**).

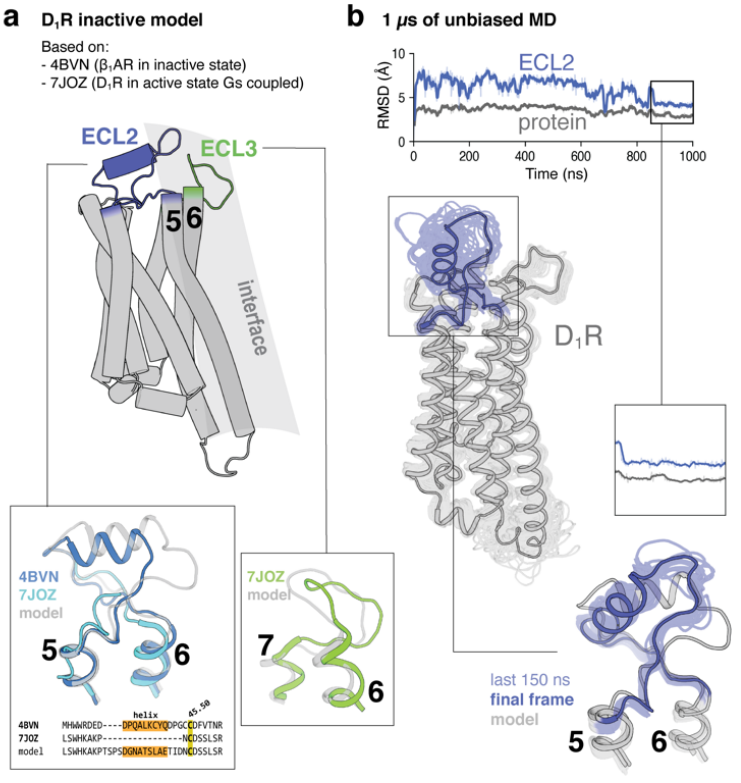


*(Figure legend on next page)*

*Figure 6. Design and refinement of an inactive $D_1R$ model.* ***(a)*** *$D_1R$ has 61% and 42% of sequence similarity and identity, respectively, with $ß_1AR$. The bottom panel (right) shows ECL3 in the model (gray) and in the structure of active D1R (green). However, ECL2 is not solved in any of the known structures of $D_1R$ and was modeled using the structure of the $ß_1AR$ as template. The bottom panel (left) shows ECL2 in the model (gray), in the $ß_1AR$ (dark blue), and the solved part in $D_1R$ (light blue). The sequence alignment between $D_1R$ (7JOZ only shows the amino acids solved in the structure) and $ß_1AR$ is also shown.* ***(b)*** *The stability of this computational model of $D_1R$ was tested in 1 µs unbiased MD simulation. RMSD plots show that, as expected, the modeled ECL2 is more flexible than the TM domain. However, ECL2 seems stabilized in the last 150 ns of simulation. Evolution of the structures of $D_1R$ (gray) and ECL2 (blue) along the MD simulation is shown in the middle panel and a detailed view of the structures of ECL2 during the last 150 ns is shown in the bottom panel.*

## 3.6 Experimental methods

Predictions generated from computational analyses, such as those performed in this thesis, require experimental validation and over the course of this thesis our group has extensively collaborated with experimental researchers. The predictions derived from our modeling studies were tested using two principal groups of techniques: those that analyze protein-protein interactions, and those that provide information about GPCR signaling, both of which are explained in this section.

### 3.6.1 Techniques to study protein-protein interactions

In the 1960s Osamu Shimomura caught more than 850,000 jellyfish in order to purify the first natural fluorescent protein which was later widely used in science: the Green Fluorescent Protein (GFP) (Miyawaki, 2008). This discovery sparked a revolution and researchers began to use these proteins to monitor biological processes ranging from gene expression to protein-protein interactions. From those jellyfish, Shimomura also identified aequorins, a protein that was able to produce blue light only when stimulated with calcium (Miyawaki, 2008). Hence, he had discovered the first fluorescent protein (which emits light when stimulated

by light) and the first bioluminescent protein (which emits light when stimulated by a reagent). Finally, he presumably even characterized the first resonance energy transfer, as GFP only glows green when it is near to a stimulated aequorin.

In the following section, a series of techniques using both fluorescence and bioluminescence to study protein-protein interactions will be presented.

**Protein complementation techniques: Bimolecular Fluorescence and Luminescence Complementation (BiFC/BiLC)**

In 2000, Gosh and colleagues split a GFP into two halves and fused each to two subunits of an anti-parallel leucine zipper to study heteromerization dynamics (Ghosh *et al.*, 2000). The rationale is that if the two leucine zipper subunits, protomers or chains interact the two GFP halves will hybridize and reconstitute a functional fluorescent protein. which will emit green light upon stimulation, this being the detectable readout. This technique was coined as Bimolecular Fluorescent Complementation (BiFC) (Kerppola, 2006). By fusing the split GFP fragments with GPCRs, BiFC can also be used to study receptor dimerization dynamics. In the experiments shown in this thesis, the fluorescent protein used is yellow instead of green (YFP).

One drawback of BiFC is that it can affect interaction dynamics, as split fluorescent proteins tend to bind irreversibly (Kerppola, 2006; Dixon *et al.*, 2016). Split bioluminescent proteins provide an alternative, in a technique known as Bimolecular Luminescence Complementation (BiLC). Split bioluminescent proteins are often preferred, as they provide higher sensitivity (Dixon *et al.*, 2016). In the studies shown here, a nanoluciferase

(NLuc) is used, and the proteins of interest are fused to the smaller fragment, known as SmBit, and a larger fragment, or LgBit.

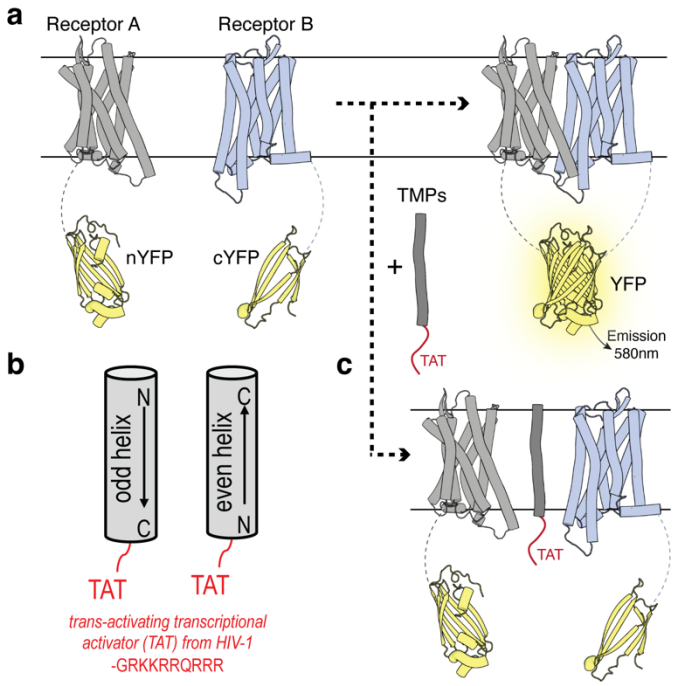


*Figure 7. Bimolecular fluorescence complementation (BiFC) with transmembrane helix peptides (TMPs). **(a)** Graphical representation of the complementation. **(b)** TMPs have to be designed carefully so that the TAT sequence is always facing the cytosol. Receptors' TMs 1, 3, 5 and 7 have the TAT sequence fused at the C-terminus, but TMs 2, 4 and 6 have it at the N-terminus. **(c)** TMPs can compete with the interaction interface of the two receptors studied.*

### Transmembrane helix peptides (TMPs)

As previously mentioned, there are cases in which BiFC might be forcing the interaction between the fusion partners (Kerppola, 2006; Dixon *et al.*, 2016), that is why the technique is used in the studies shown in this thesis in combination of what are known as synthetic transmembrane helix peptides (TMPs). This strategy consists of the use peptides having a part of the sequence corresponding to a given GPCR TM segment and another part with the YGRKKRRQRRR sequence of activator of transcription

(TAT) protein of the human immunodeficiency HIV-1 virus (Schwarze *et al.*, 1999). The latter is a strong positively charged sequence that will drive the whole peptide towards its insertion in the membrane, with the TAT sequence falling in the intracellular area. This way the GPCR TM will potentially compete with the interaction interface between receptors (**Figure 7**). The potency of peptides containing the TAT sequence was *in vivo* proven by the delivery of TAT-β-galactosidase to different mice tissues (Schwarze *et al.*, 1999).

The BiFP fluorescence signal is therefore measured both in the presence and absence of TMPs. If a decrease in signal is observed when a TMP is co-transfected, one can assume that this TM helix is involved in the dimerization interface and that the BiFC signal is driven by specific GPCR interactions, as opposed to unspecific BiFC reconstitution. This technique has demonstrated its destabilizing effects in previous publications (Navarro, Cordomí, Casadó-Anguera, *et al.*, 2018; Navarro, Cordomí, Brugarolas, *et al.*, 2018; Köfalvi *et al.*, 2020; Moreno *et al.*, 2017; Cai *et al.*, 2019; Franco *et al.*, 2021), not included in this thesis. In the studies shown in this thesis (CHAPTER II, III and IV) each TM helix (1 to 7) of the receptors of interest is tested to explore all the possible interfaces.

**Bioluminescence resonance energy transfer (BRET)**

This technique relies on the same principle as aequorin and GFP observed in jellyfish, as described above. Aequorin can only emit light if stimulated with calcium, and if the protein is found at a sufficiently close (between 5-10 nm) to GFP, the latter will be excited by aequorin and will also emit light at a different wavelength, a phenomenon known as resonance energy transfer. Then, after stimulation with calcium, one can measure the basal light (blue light in the case of aequorin) versus the light

emitted by the fluorescent counterpart (green light in the case of GFP), to see if these two proteins are in close enough contact for energy transfer to occur. If each of these are fused to two receptors of interest, it can be extrapolated that if the readout is fluorescent emitted light, the receptors may be interacting. In the experiments shown in this thesis, the bioluminescent protein energy donor is a Renilla luciferase (RLuc), and YFP is the fluorescent resonance energy transfer partner.

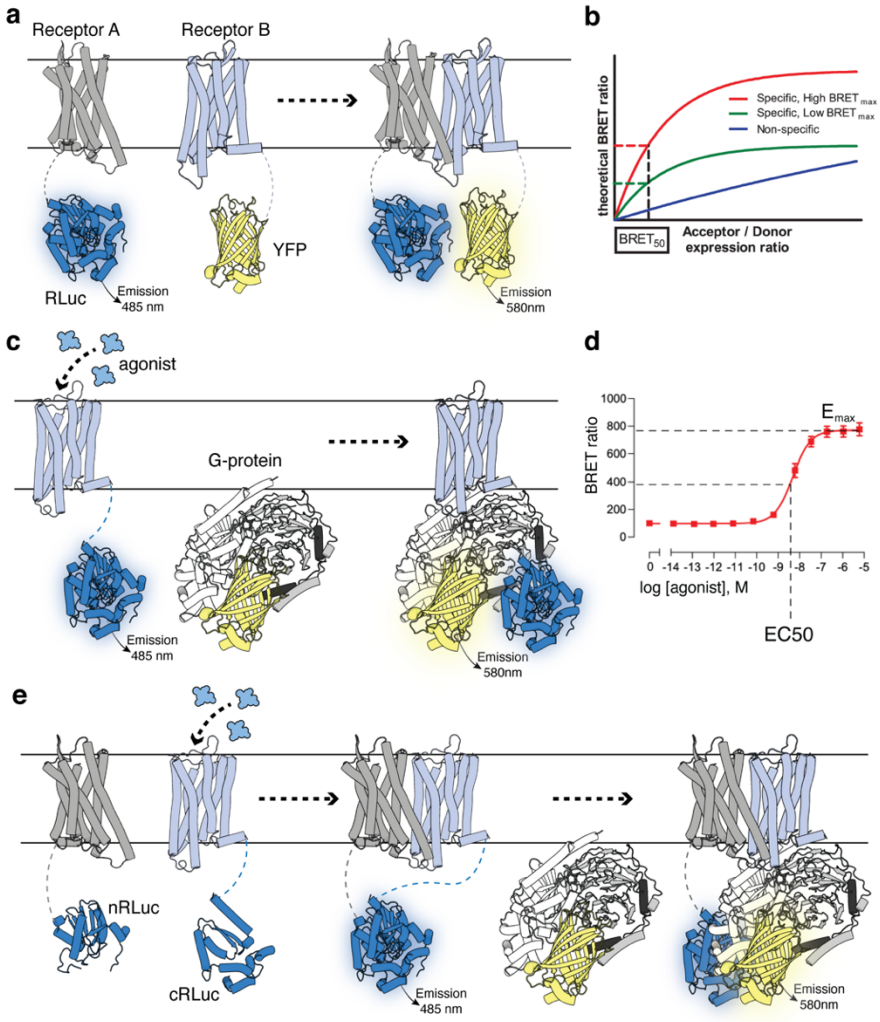


*(Figure legend on next page)*

*Figure 8. Techniques based on resonance energy transfer.* ***(a)*** *Schematic representation of bioluminescence resonance energy transfer (BRET), and* ***(b)*** *an example of theoretical BRET saturation curves taken from (Szalai et al., 2014). (**c**) Schematic representation of ligand-induced BRET ratio and* ***(d)*** *a real dose-response curve taken from (Avet et al., 2022). (**e**) Schematic representation of complemented donor-acceptor resonance energy transfer (CODA-RET).*

In BRET saturation experiments, one GPCR is fused to RLuc while the other to YFP, and the increase of yellow light versus basal is measured upon increasing concentrations of the RLuc-fused receptors (**Figure 8a**). With a constant expression of the YFP-fused counterpart, if the behavior observed follows a sigmoidal curve, the two receptors are likely interacting in the membrane. Instead, if the behavior observed is linear, the increase in light is probably just due to the increase in RLuc-fused receptor expression (**Figure 8b**).

BRET can also be used to study receptor-effector couplings. An experiment that is shown in this thesis consists in the fusion of Rluc to the GPCR, and the YFP to the G-protein (**Figure 8c**). Upon increasing concentrations of an agonist, one could expect to see increased G-protein coupling, meaning there will be an increase of light emission versus basal. Then, what is measured here is known as the BRET ratio, and a drug concentration-binding curve can be obtained. From this, values of affinity (EC50) and efficacy (Emax) can be calculated (**Figure 8d**).

**Complemented donor-acceptor resonance energy transfer (CODA-RET)**

BRET and protein complementation techniques can also be combined to measure more than one interactive event at once, in what is known as CODA-RET (Urizar *et al.*, 2011). This technique is used in the results shown in this thesis to study both receptor dimerization and G-protein coupling, and the output measurement is still the BRET ratio. Typically, each receptor is fused to one half of the Rluc, and the effector protein to

YFP. Then, light emission versus basal is only observed when the two receptors are interacting (Rluc hybridizes) and G-protein is coupling (there is an energy transfer between Rluc and YFP) (**Figure 8e**).

### 3.6.2 Functional studies

Receptor functionality can also be studied by following intracellular effects and the downstream signaling cascade. Each G-protein that a GPCR can couple with will induce distinct intracellular effects when activated. If the receptor preferentially binds a Gs (stimulatory) an increase in cAMP levels can be measured. The opposite will be observed if the receptor couples to a Gi (inhibitory). In the case of the Gq, calcium release via phospholipase C (PLC) activity will be observed. The techniques to measure these secondary messengers (cAMP and $Ca^{2+}$) also rely on fluorescence and energy transfer.

**cAMP accumulation assays (Figure 9a)**

With this technique, basal cAMP molecules are labelled with a fluorophore, while fluorophore-conjugated anti-cAMP antibodies are added. When the anti-cAMP antibodies recognize labelled cAMP, an energy transfer occurs, and can be detected. However, if the levels of cAMP in the cell were to increase, most of the labelled cAMP will be displaced from those antibodies, inducing a decrease in fluorescence. The lower the fluorescence, the higher the increase in cAMP. In cases in which a decrease in cAMP needs to be measured (Gi-coupling), the cell needs to be first stimulated with forskolin (Fk), which will induce the cAMP production by binding to the adenylyl cyclase (AC).

### $Ca^{2+}$ release assays (Figure 9b)

Calcium assays are detected using a synthetic biosensor, which is generally based on a fusion protein that can recognize the cation and trigger a light in response. In the assays presented in this thesis a fluorescent protein is fused to calmodulin (CaM), a protein that undergoes a conformational change upon calcium binding. This conformational change is, in turn, transmitted to the fluorescent protein fusion partner, allowing it to be stimulated. The higher the concentration of $Ca^{2+}$, the higher the detected light (Chen *et al.*, 2013).

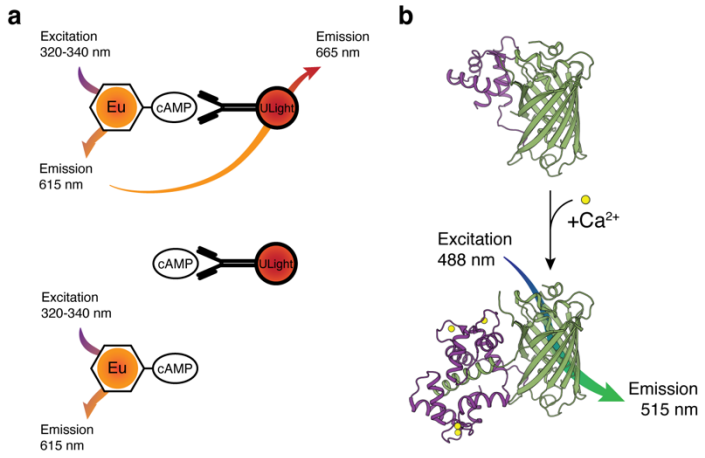


*Figure 9. Signaling assays for signaling response characterization of GPCRs. (a) Principles of the cAMP assay used. Europium labeled cAMP is provided that emits light at 615 nm after excitation. Energy transfer happens between Europium and ana antibody with ULight bead attached to an antibody targeting cAMP molecules when they are close enough (upper panel). However, when endogenous cAMP levels increase, these non-tagged molecules will compete for the ULight antibodies reducing the energy transfer (lower panel).* ***(b)*** *Ca2+ mobilization assay principles. Cells are transfected with GPF (pale green) fused to calmodulin (in purple) engineered construct, which is non-fluorescent in its resting state. When Ca2+ increase is present, the ions will bind to calmodulin and cause its structural rearrangement, so GFP is able to emit fluorescence light if properly excited.*

# 4 CHAPTER I

*Ligands alter the dynamics of receptor heteromerization*

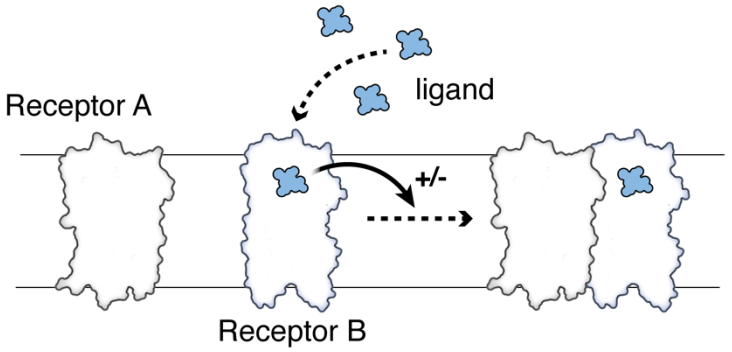

## 4.1 Case Study #1. Exploring the effects of standard antipsychotics on adenosine $A_{2A}$-dopamine $D_2$ receptor heteromerization.

Published as **co-first author** in

Valle-León, M.[1], Casajuana-Martin, N.[1], Llinas del Torrent, C., Argerich, J., Gómez-Acero, L., Sahlholm, K., Ferré, S., Pardo, L., Ciruela, F. **Unique Effect of Clozapine on Adenosine $A_{2A}$-Dopamine $D_2$ Receptor Heteromerization.** *Biomedicine & Pharmacotherapy* (2023)

[1]These authors contributed equally

### 4.1.1 Introduction

$D_2R$ signaling is crucially involved in several physiological functions, such as control of movement, goal-directed behavior and reward, memory, and behavioral salience, as well as regulation of prolactin release. In the brain, $D_2R$ is highly expressed in the striatum and to a somewhat lower extent in the midbrain, cortex, hypothalamus, amygdala, and hippocampus (Beaulieu and Gainetdinov, 2011). Antipsychotic drugs are antagonists or weak partial agonists of $D_2R$. These are typically divided into three groups: first, second and third-generation antipsychotics. The compounds from each group are efficacious as antipsychotics and have different types and degrees of secondary effects, mainly EPS (extrapyramidal effects, in essence, involuntary and uncontrollable movements). The properties from each group (with a representative compound) are summarized in **Table 1**.

*Table 1. Summary of the properties of the compounds used in this study.*

| Group | Compound | Pharmacology on $D_2R$ | EPS |
|---|---|---|---|
| **First generation** | Haloperidol | Antagonist | High |
| **Second generation** | Clozapine | Antagonist | Low |
| **Third generation** | Aripiprazole | Partial agonist | Low |

According to several meta-analyses, clozapine still represents one of the most effective antipsychotic drugs with the lowest incidence in EPS (Leucht *et al.*, 2009; Huhn *et al.*, 2019). Therefore, identification of the unique molecular and cellular mechanisms of clozapine, as compared to those of other antipsychotics, should allow us to explain its unique pharmacological profile. A possible mechanism to consider is the differential effect of clozapine on the immediate environment of $D_2R$, more specifically on its interactions with other membrane proteins, such as other GPCRs. There is significant experimental evidence indicating that a main population of striatal $D_2R$ forms heteromers with the adenosine $A_{2A}$ receptor ($A_{2A}R$) within a macromolecular complex that includes adenylyl cyclase (AC) (Bonaventura *et al.*, 2015; Ferré *et al.*, 2022; Navarro, Cordomí, Casadó-Anguera, *et al.*, 2018), and there is preclinical evidence indicating the involvement of $A_{2A}R$ and $A_{2A}R$-$D_2R$ heteromers in schizophrenia. Actually there is evidence for reduced levels of the heteromer (in postmortem caudate nucleus and striatum) even though the separate expression of these receptors is upregulated (Valle-León *et al.*, 2021).

Using a NanoBiT assay (an alternative name for nanoluciferase, NL, complementation, see METHODS), the objective was to investigate in more detail the dynamics of $A_{2A}R$-$D_2R$ heteromerization in living cells after long exposure to the antipsychotic drugs haloperidol, aripiprazole, or clozapine. Computational studies were implemented to structurally rationalize the differential impact of antipsychotics on $A_{2A}R$-$D_2R$ heteromerization. Importantly significant qualitative differences were obtained with clozapine compared to haloperidol and aripiprazole, providing a possible new mechanism involved in the unique clinical profile of clozapine.

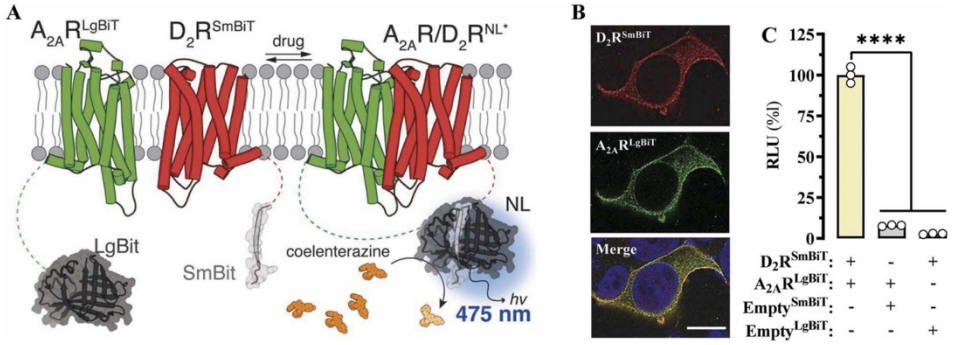


*Figure 1. NanoBiT-based $A_{2A}R/D_2R$ heteromer detection in living cells. (a) Schematic representation of the NanoBiT-based receptor-receptor interaction detection system. The $A_{2A}R$ and $D_2R$ tagged with LgBiT and SmBiT (i.e., $A_{2A}R^{LgBiT}$ and $D_2R^{SmBiT}$, respectively) and its potential drug-dependent dynamic modulation is shown. Upon $A_{2A}R/D_2R$ heteromerization, the proximity of the receptors may allow the NanoBiT fragments to reconstitute a functional nanoluciferase (NL), thus able to metabolize the coelenterazine 400a substrate leading to 475 nm light emission. (b). Immunofluorescence detection of $A_{2A}R$ and $D_2R$ in living cells. HEK-293 T cells were transiently transfected with the cDNA encoding $A_{2A}R^{LgBiT}$ and $D_2R^{SmBiT}$ and processed for immunofluorescence detection using specific anti-$A_{2A}R$ and anti-$D_2R$ antibodies (see Methods of original publication). (c) $A_{2A}R/D_2R$ heteromer-mediated NL complementation. HEK-293 T cells transiently transfected with $A_{2A}R^{LgBiT}$ and $D_2R^{SmBiT}$ were incubated with coelenterazine 400a (10 µM) and the luminescence recorded. Results from three independent experiments performed in triplicate were expressed as percentages (mean ± SEM) of the relative luminescence signal (RLU). ****p < 0.0001 one-way ANOVA with Dunnett's post-hoc test when compared to $A_{2A}R^{LgBiT}$ plus $D_2R^{SmBiT}$ expressing cells.*

## 4.1.2 Results

### Antipsychotics differentially alter the dynamics of $A_{2A}R$-$D_2R$ heteromerization in living cells

The group at UB engineered a NanoLuc Binary Technology (NanoBiT)-based assay (Wouters *et al.*, 2018) to monitor the dynamics of $A_{2A}R$-$D_2R$ heteromerization in HEK-293 T cells. To this end, $A_{2A}R$ and $D_2R$ were fused to a long portion (LgBiT) and a short portion (SmBiT) of nanoluciferase (NL) (**Figure 1a**). Upon expression in HEK-293 T cells, $A_{2A}R^{LgBiT}$ and $D_2R^{SmBiT}$ showed a high degree of co-distribution both intracellularly and at the plasma membrane level (**Figure 1b**). The ability of NL to reconstitute after heteromerization in HEK293T cells expressing

$A_{2A}R^{LgBiT}$ and $D_2R^{SmBiT}$ was evaluated by recording NL-mediated luminescence (**Figure 1c**). Collectively, these results validate our NanoBiT-based approach to monitor the density of $A_{2A}R$-$D_2R$ heteromers in living cells.

The impact of antipsychotics on the temporal dynamics of $A_{2A}R$-$D_2R$ heteromerization was evaluated by treating $A_{2A}R^{LgBiT}$ and $D_2R^{SmBiT}$ expressing HEK-293 T cells with haloperidol, clozapine, or aripiprazole for 2 h or 16 h. To this end, concentration-response curves were constructed after incubation of $A_{2A}R^{LgBiT}$ and $D_2R^{SmBiT}$ expressing HEK-293 T cells with increasing concentrations of haloperidol, clozapine, and aripiprazole for 2 h or 16 h (**Figure 2a**). Interestingly, while 2 h of incubation with haloperidol or aripiprazole did not alter the heteromer content, the same treatment with clozapine significantly reduced the amount of heteromer in a concentration dependent manner (pEC50=6.1 ± 0.3) (**Figure 2a**). However, 16 h of exposure resulted in a significant concentration-dependent increase in $A_{2A}R$-$D_2R$ heteromers with haloperidol or aripiprazole (pEC50=7.8 ± 0.4 and pEC50=6.8 ± 0.4, respectively), while clozapine did not show differences compared to controls (**Figure 2a**). In general, these results demonstrate a differential effect of clozapine compared to other antipsychotics on the dynamics of $A_{2A}R$-$D_2R$ heteromerization. Both haloperidol and aripiprazole promoted an increase in $A_{2A}R$-$D_2R$ heteromerization upon long-term exposure, while clozapine shows a unique temporal modulation, with an initial decrease followed by normalization and a lack of long-term-induced increase in $A_{2A}R$-$D_2R$ heteromerization.

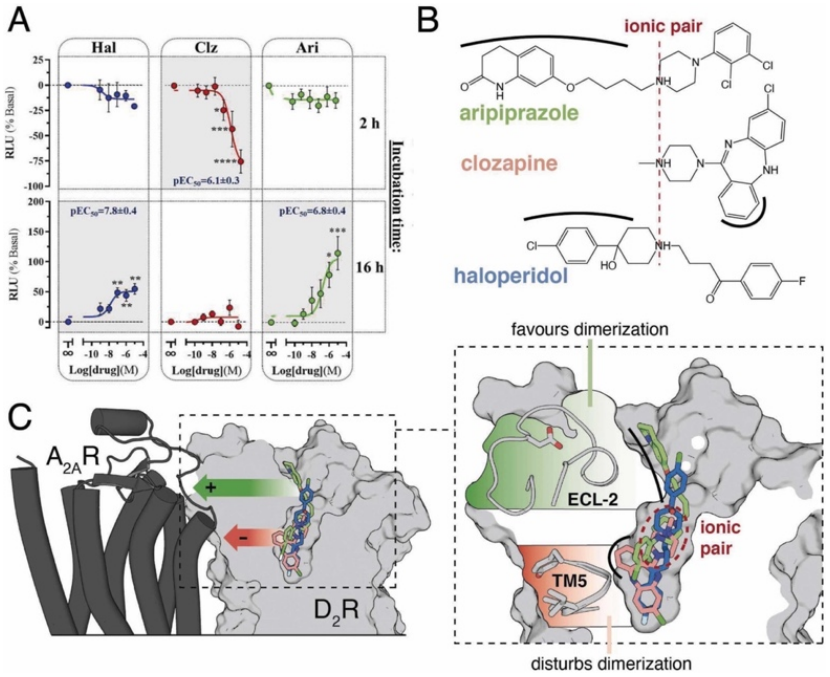


*Figure 2. Dynamic modulation of $A_{2A}R$-$D_2R$ heteromerization by antipsychotics. (a) HEK-293T cells transiently expressing $A_{2A}R^{LgBiT}$ and $D_2R^{SmBiT}$ were incubated with increasing concentrations of haloperidol (Hal), clozapine (Clz), and aripiprazole (Ari) for 2h or 16h and NanoBiT concentration-response curves were constructed. Results are expressed as percentages (mean ± SEM) of the relative luminescence signal (RLU) of vehicle (∞) treated cells from five independent experiments performed in triplicate. *p < 0.0, **p < 0.01, ***p < 0.001, one-way ANOVA with Dunnett's post hoc test when compared to vehicle treated cells.* ***(b,c)*** *Chemical structures and molecular docking of haloperidol (blue), clozapine (pink), and aripiprazole (green) into the $D_2R$ monomer (PDB id 6CM4). The protonated amine of the ligands (red dashed line) that forms an ionic pair with $D114^{3.32}$ of $D_2R$ is highlighted (red circle). The bulky aromatic ring of clozapine, absent in the other compounds, that occupies an additional volume near TM5 is highlighted (black line); and the groups of haloperidol and aripiprazole, absent in clozapine, that extend toward ECL2 are also highlighted (black line). The position of $A_{2A}R$ (5IU4, grey cylinders) in the $A_{2A}R$-$D_2R$ heteromer, constructed from the TM 4/5 dimeric interface observed in the $\beta_1AR$ (4GPO), is shown as a reference but not included in the docking procedure.*

*Table 2. Computational simulations of antipsychotic compounds bound to the $D_2R$ monomer or $A_{2A}R$-$D_2R$ heteromer.* *Average values (in Å) of key properties in three replicas of unbiased 1 μs MD simulations.*

| | ligand | property | replica 1[a] | replica 2[a] | replica 3[a] | p-value[b] |
|---|---|---|---|---|---|---|
| $D_2R$ | --- | (x,y) TM 5 $D_2R$[c] | (9.4, -3.6) | (9.3, -3.4) | (10.0, -3.9) | |
| | Aripiprazole | | (9.9, -3.9) | (10.0, -3.9) | (9.7, -3.6) | (0.188, 0.173) |
| | Haloperidol | | (9.2, -3.3) | (9.6, -4.1) | (9.6, -3.7) | (0.412,0.413) |
| | Clozapine | | (10.1, -5.3) | (9.8, -4.6) | (10.3, -4.6) | (0.063,0.023) |
| $A_{2A}R$-$D_2R$ | --- | (x,y) TM 4 $D_2R$[d] | (3.4, -13.5) | (3.7, -13.6) | (3.0, -13.4) | |
| | Clozapine | | (3.4, -13.5) | (3.6, -13.8) | (3.7, -13.8) | (0.250,0.089) |
| | --- | (x,y) TM 5 $D_2R$[e] | (9.8, -3.2) | (9.6, -3.4) | (9.9, -3.6) | |
| | Clozapine | | (10.4, -5.6) | (10.4, -5.8) | (10.8, -5.0) | (0.023,0.025) |
| | --- | (x,y) TM 4 $A_{2A}R$[f] | (15.9, -12.6) | (15.9, -12.6) | (17.7, -11.6) | |
| | Clozapine | | (15.4, -16.6) | (17.0, -15.1) | (16.7, -14.4) | (0.412,0.023) |
| | --- | (x,y) TM 5 $A_{2A}R$[g] | (7.9, -20.9) | (8.2, -21.0) | (10.8, -20.7) | |
| | Clozapine | | (6.9, -23.8) | (8.7, -23.1) | (8.0, -21.6) | (0.206,0.025) |
| | --- | distance between centers of mass[h] | 24.4 | 25.1 | 23.2 | |
| | Clozapine | | 28.4 | 27.4 | 27.5 | 0.025 |

[a]Average values of 100 structures collected every 10 ns [b]Statistical significante was calculated by Mann–Whitney test, one-tailed, n1 = n2 = 3, relative to unliganded receptor. P-values < 0.05 are shown in bold [c-g]Center of mass of amino acids [c]$Y192^{5.41}$-$I195^{5.44}$ of $D_2R$, and [d]$T165^{4.55}$-$P169^{4.59}$ and [e]$Y192^{5.41}$-$V196^{5.45}$ of $D_2R$ and [f]$I136^{4.56}$-$P139^{4.60}$ [g]$Y179^{5.40}$-$F183^{5.44}$ of $A_{2A}R$ in the $A_{2A}R$-$D_2R$ heteromer [h]Distance between the centers of mass of $D_2R$ and $A_{2A}R$ in the $A_{2A}R$-$D_2R$ heteromer

## Different structural conformations of $D_2R$ upon binding to antipsychotics

GPCRs are dynamic proteins that permit rapid ligand-dependent small-scale structural fluctuations (Nygaard *et al.*, 2013). We have proposed that these fluctuations promote allosteric interactions in GPCR heteromers through their transmembrane interface (Ferré *et al.*, 2022), which we recently applied to the analysis of the effect of clozapine on the signaling of the $CB_1R$-5-$HT_{2A}R$ heteromer (Guinart *et al.*, 2020). Thus, to understand the distinctive molecular signature of clozapine, relative to haloperidol or aripiprazole, I first performed computational simulations of these three antipsychotics (**Figure 2b**) bound to the $D_2R$ monomer. Our initial simulations revealed key structural differences, despite those all three antipsychotics bind to the same orthosteric pocket (**Figure 2c**). Specifically, the aromatic ring of clozapine occupies an additional volume near TM5, while both haloperidol and aripiprazole, with a more compact and elongated structure, extend towards the extracellular environment

(**Figure 2c**). Therefore, the bulky aromatic ring, present only in clozapine, could alter TM5 of $D_2R$, which forms part of the $A_{2A}R$-$D_2R$ heteromerization interface (Navarro et al., 2018), disturbing $A_{2A}R$-$D_2R$ heteromerization; whereas the extended binding modes of haloperidol and aripiprazole to the extracellular domain, absent in clozapine, could influence the conformation of extracellular loop 2 (ECL2), favouring $A_{2A}R$-$D_2R$ heteromerization (see below and **Figure 2c**). To test these hypotheses, we first performed three replicate runs of unbiased 1 µs MD simulations of the $D_2R$ monomer in the absence and presence of these antipsychotics.

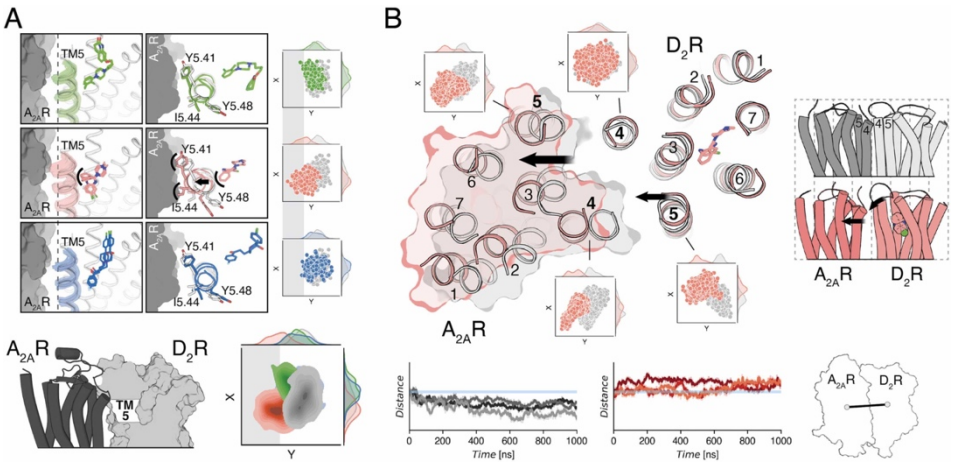


*Figure 3. Influence of clozapine binding to $D_2R$ on the $A_{2A}R$-$D_2R$ heteromer. (a) Representative side (left panels) and upper (middle panels) views of TM5 and the $Y192^{5.41}$, $I195^{5.44}$, and $Y199^{5.48}$ side chains obtained in MD simulations of the $D_2R$ monomer in the absence (in grey) and presence of haloperidol, clozapine, or aripiprazole (color code as in **Figure 2**). The surface of $A_{2A}R$ in grey is shown as a reference but is not included in the simulations. Grey broken line represents the position of TM5 in the simulation of apo-$D_2R$, black arrow represents the movement of TM5 in the presence of clozapine relative to apo-$D_2R$, and black lines represent the aromatic ring of clozapine and the amino acids of $D_2R$ that would clash with $A_{2A}R$. The evolution of the center of mass of amino acids $Y192^{5.41}$- $I195^{5.44}$ in TM5 during three replicates of unbiased 1 µs MD simulations (100 structures collected every 10 ns in each replicate) is shown in right panels. The xy plane is as defined by the Orientations of Proteins in Membranes (OPM) (Lomize et al., 2006). Distributions of the x and y values are shown on the right x-axis and top y-axis, respectively. Grey rectangle represents the area in the y axis that is not occupied by the amino acids of TM5 in the apo simulations. Contour plots and distributions of X,Y values (see **Table 2**) illustrated above for comparison purposes.*

*(b) Representative structures obtained in MD simulations of the $A_{2A}R$-$D_2R$ heteromer in the absence (grey) and presence of clozapine (pink). Evolution of the center of mass of amino acids T165$^{4.55}$-P169$^{4.59}$ in TM4 and Y192$^{5.41}$-V196$^{5.45}$ in TM5 of $D_2R$ and I136$^{4.56}$-P139$^{4.60}$ in TM4 and Y179$^{5.40}$-F183$^{5.44}$ in TM5 of $A_{2A}R$ during three replicas of unbiased 1 μs MD simulations (100 structures collected every 10 ns in each replica) and their distributions. The xy plane is defined as above. Black arrows represent the movement of TM helices in the presence of clozapine relative to apo-$D_2R$. The side view on the $A_{2A}R$-$D_2R$ heteromer (right panels) displays a grid to evaluate the movement of $A_{2A}R$ relative to $D_2R$. The proximity between $A_{2A}R$ and $D_2R$ within the heteromer was monitored by the distance between centers of mass of $A_{2A}R$ and $D_2R$ in the absence (grey) and presence of clozapine (pink). Blue line shows the initial distance that decreases in apo-$D_2R$ and increases in the presence of clozapine.*

Simulations suggest that neither haloperidol nor aripiprazole alters the conformation of TM5 with respect to apo-$D_2R$, while clozapine displaces TM5 (Y192$^{5.41}$ and I195$^{5.44}$) 1.2 Å toward the membrane (supposedly toward the $A_{2A}R$ interface, see below), relative to apo-$D_2R$ ($p = 0.023$, **Table 2**) (**Figure 3a**). On the other hand, ECL2 of $D_2R$, between TMs 4 and 5, also involved in the $A_{2A}R$-$D_2R$ interface (see below), has adopted two different conformations in the known structures: helical in inactive $D_2R$ bound to haloperidol (Fan *et al.*, 2020) and risperidone (Wang *et al.*, 2018) or extended in inactive $D_2R$ bound to spiperone (Im *et al.*, 2020) and active $D_2R$ bound to bromocriptine (Yin *et al.*, 2020; Zhuang *et al.*, 2021) (**Figure 4b**). Previous MD simulations by others have shown that this ECL2 is highly dynamic, with a spontaneous transition between both conformations (Lane *et al.*, 2020). However, the extended conformation positions ECL2 in the binding pocket, limiting its size (Im *et al.*, 2020), so bitopic ligands with extended binding modes to the extracellular domain, such as haloperidol and aripiprazole, could favor the helical conformation. The flexibility of ECL2 in our MD simulations, modelled in the helical conformation (see Methods), was characterized by the root-mean-square fluctuation (RMSF) and associated B-factor values in the absence and presence of these antipsychotics (**Figure 4a**). As expected, the lack of the extended binding mode of clozapine makes ECL2 of $D_2R$ more flexible

(comparable to the values of apo-$D_2R$) than when haloperidol or aripiprazole are bound.

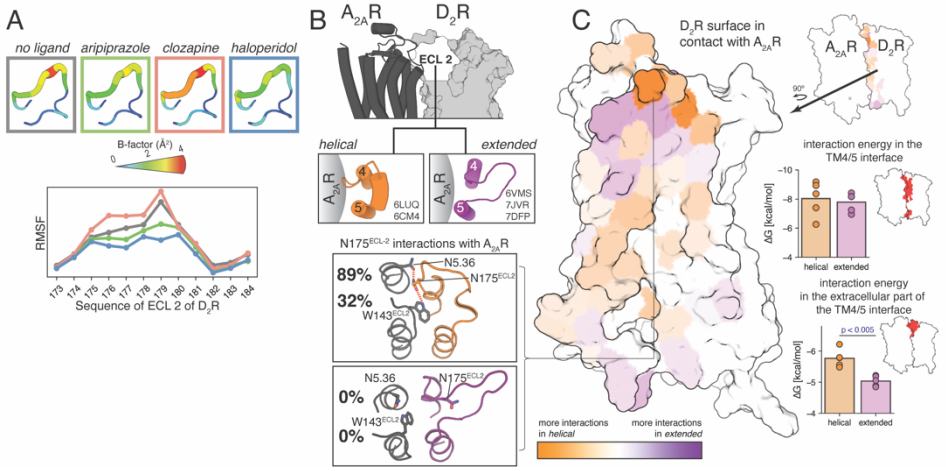


*Figure 4. Influence of haloperidol and aripiprazole binding to $D_2R$ on the $A_{2A}R$-$D_2R$ heteromer. **(a)** Average root-mean-square fluctuation (RMSF) during three replicates of unbiased 1 μs MD simulations (100 structures collected every 10 ns in each replicate) of ECL 2 of $D_2R$, in the helical conformation, in the absence and presence of haloperidol, clozapine, or aripiprazole (color code as in Fig. 3). Detailed view of ECL 2 of $D_2R$ and associated B-factor values. **(b)** ECL 2 of $D_2R$, between TMs 4 and 5, adopts a helical conformation in the 6LUQ and 6CM4 structures and an extended conformation in the 6VMS, 7JVR, and 7DFP structures. ECL 2 is oriented toward $A_{2A}R$ in the helical conformation and folds over the binding pocket in the extended conformation. **(c)** Surface representation of $D_2R$ in contact with $A_{2A}R$ in the $A_{2A}R$-$D_2R$ heteromer, color coded by the difference in the number of interactions in the helical or extended conformation of ECL 2 of $D_2R$, as calculated during five replicates of unbiased 1 μs MD simulations (100 structures collected every 10 ns in each replicate) of A2AR-D2Rextended and A2AR-D2Rhelical in which ECL 2 was modelled in the extended and helical conformation, respectively, without ligand bound to them (see Methods). Calculated energies of interaction, with PRODIGY (Vangone and Bonvin, 2015), between A2AR and D2Rhelical and A2AR and D2Rextended by the amino acids (in red) forming the TM 4/5 interface (top) and the extracellular part of the TM4/5 interface (bottom). Detailed view of the interactions between N175ECL2 in D2Rhelical (top) and D2Rextended (bottom) and A2AR. Statistical significance was calculated by non-parametric Mann–Whitney test.*

## Influence of the different conformations of $D_2R$ on the $A_{2A}R$-D2R heteromeric interface

Here, I want to address the influence of the outward movement of TM5 of $D_2R$, triggered by the bulky aromatic ring of clozapine; and the helical conformation of ECL2 of $D_2R$, stabilized by the extended binding mode of

haloperidol and aripiprazole, on the experimentally observed ligand-induced changes of $A_{2A}R$-$D_2R$ heteromerization. Consequently, we performed similar simulations to those with the $D_2R$ monomer (see above) on the $A_{2A}R$-$D_2R$ heteromer, which, in this case, required computational modelling of the $A_{2A}R$-$D_2R$ interface. Previously reported bimolecular fluorescence complementation (BiFC) experiments, in the presence of synthetic peptides corresponding to different TM domains of $A_{2A}R$ and $D_2R$, revealed TMs 4 and 5 to form the $A_{2A}R$-$D_2R$ heteromer interface (TM 4/5 interface) (Navarro et al., 2018).

Our simulations of the $A_{2A}R$-$D_2R$ heteromer confirmed that the voluminous aromatic ring of clozapine displaces TM5 of $D_2R$ 2 Å towards $A_{2A}R$, relative to apo-$D_2R$ ($p = 0.025$, **Figure 3b** and **Table 2**). This clozapine-induced change in TM5 of $D_2R$ triggers the displacement of TM4 (3.1 Å, $p = 0.023$) and TM5 (2 Å, $p = 0.025$) of $A_{2A}R$, the TM domains that form the heteromeric interface (**Figure 3b** and **Table 2**). Consequently, $A_{2A}R$ moves 3.5 Å apart from $D_2R$ (measured by the distance between the centers of mass of $A_{2A}R$ and $D_2R$ ($p = 0.025$, **Figure 4b** and **Table 2**), in a rigid body movement in which the deformation of $A_{2A}R$ is negligible (as it can be observed in the RMSD plots in **Suppl. Figure 1**). This displacement is also captured with protomer-protomer interaction maps (**Suppl. Figure 1**), where a reduction of the interactions is observed, followed by a lower interaction energy as calculated by PRODIGY (Vangone and Bonvin, 2015). In summary, these MD simulations indicate that the bulky aromatic ring of clozapine destabilizes the heteromerization of $A_{2A}R$-$D_2R$.

ECL2 of $D_2R$ in the extended conformation folds over the binding pocket, whereas ECL2 in the helical conformation, stabilized by haloperidol and aripiprazole binding, orients the $G173^{4.63}$-$Q179^{ECL2}$ stretch of amino acids

toward $A_{2A}R$ (**Figure 4b**), which could influence $A_{2A}R$-$D_2R$ heteromerization in this extracellular part. Thus, to understand the role of these amino acids in the formation of the TM 4/5 interface of $A_{2A}R$-$D_2R$, we performed MD simulations of $A_{2A}R$-$D_2R^{extended}$ (5 ×1 µs) in which ECL2 was modelled in the extended conformation and $A_{2A}R$-$D_2R^{helical}$ (5 ×1 µs) in which ECL2 was modelled in the helical conformation without any bound ligand (see Methods in the original publication). The calculated energy of interaction of full TM 4/5 interface shows no significant differences between extended and helical conformations ($p = 0.71$), but when this analysis is performed only at the extracellular part of the TM 4/5 interface, ECL2 in the helical conformation forms a stronger interaction with $A_{2A}R$ than in the extended conformation ($p = 0.001$) (**Figure 4c**). The decrease in interaction energy is due to a differential pattern of interactions, as observed in the detailed panels of **Figure 4c**, with $N175^{ECL2}$ being most responsible for the change. The helical conformation of ECL2 makes $N175^{ECL2}$ to point towards $A_{2A}R$, contrary to the extended conformation, facilitating the hydrogen bond interaction with N5.36 and $W143^{ECL2}$ of $A_{2A}R$. In summary, these simulations indicate that, contrary to clozapine, haloperidol and aripiprazole stabilize $A_{2A}R$-$D_2R$ heteromerization by stabilizing the helical conformation of ECL2 of $D_2R$.

### 4.1.3 Discussion

Using a NanoBiT-based live cell assay, the present study found evidence for a differential effect of clozapine, compared to haloperidol and aripiprazole, on the dynamics of $A_{2A}R$-$D_2R$ heteromerization. Clozapine disrupted $A_{2A}R$-$D_2R$ heterodimer after 2 h of treatment, while haloperidol and aripiprazole promoted its formation after 16 h of incubation. MD simulations provided mechanistic explanations for the heteromer-

destabilizing effect of clozapine and the heteromer-stabilizing properties of haloperidol and aripiprazole. The bulky tricyclic moiety of clozapine displaces TM5 of $D_2R$, altering the $A_{2A}R$-$D_2R$ heteromeric interface, increasing the mean distance between the $A_{2A}R$ and $D_2R$ protomers in the heteromer. In contrast, the extended binding mode of haloperidol and aripiprazole toward the extracellular domain stabilizes the helical conformation of ECL2 of $D_2R$, enhancing the interaction with $A_{2A}R$.

The relationship between levels of expression of $D_2R$ and EPS is still controversial (Silvestri *et al.*, 2000; Samaha *et al.*, 2007; Suzuki *et al.*, 2015). Based on previous studies (Ögren *et al.*, 1997; Ferré, Schwarcz, *et al.*, 1994; Bonaventura *et al.*, 2015; Ferré, 2016), it might be that it is not simply the increase in the number of $D_2Rs$ in the plasma membrane, but the increase in the number of $D_2Rs$ that form heteromers with $A_{2A}R$, or a relative decrease in the number of $D_2R$ or $A_{2A}R$ not forming heteromers, what facilitates the appearance of EPS upon long exposure to antipsychotics. Clozapine would then be protective against EPS due to its specific ability to destabilize $A_{2A}R$-$D_2R$ heteromerization, while haloperidol and aripiprazole would facilitate $A_{2A}R$-$D_2R$ heteromerization and, therefore, favor EPS. Indeed, this adds an additional layer of complexity to our initial interpretation of the role of $A_{2A}R$-$D_2R$ heteromerization in schizophrenia, where we claimed that an increase in $A_{2A}R$-$D_2R$ heteromers may be of therapeutic importance (Valle-León *et al.*, 2021).

Overall, the present study opens a new rationale for considering GPCR heteromers as therapeutic targets in psychosis: the possibility of decreasing the density or stability of $A_{2A}R$-$D_2R$ heteromers.

## 4.1.4 Supplementary Material

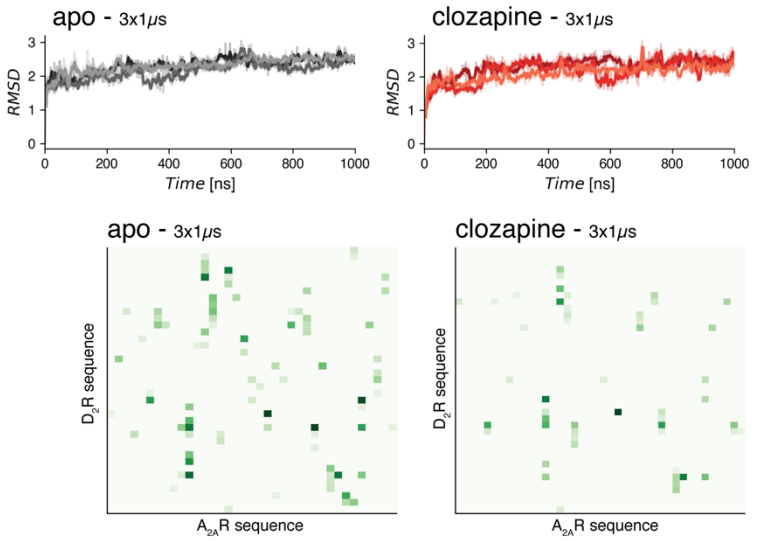


| | | |
|---|---|---|
| ***N interactions*** | 92.14 (23.81) | 81.83 (8.31) |
| ***ΔG$_{estimate}$*** | -8.06 kcal/mol (1.79 kcal/mol) | -5.54 kcal/mol (0.79 kcal/mol) |
| | *mean (std)* | *mean (std)* |

*Supplementary Figure 1. Analysis of the MD simulations with the $D_2R$-$A_{2A}R$ heteromer. The stability of the complex is monitored in the RMSD over simulation time plots, both unliganded (apo) and bound to clozapine (clozapine) showing a similar trend. The frequency of interaction is also monitored between the two protomers, and the total mean number of interactions (N interactions) and mean energy of interaction (ΔGestimate) is also calculated. The data from the heatmaps was obtained from getcontacts (https://getcontacts.github.io/), where each square represents an interaction, and the darker the color the more frequent it is along the simulation. PRODIGY (Vangone and Bonvin, 2015) was used to asses the amount of interactions and energy of interaction.*

# 5 CHAPTER II

*Receptor heteromerization alters the pharmacodynamic properties of ligands*

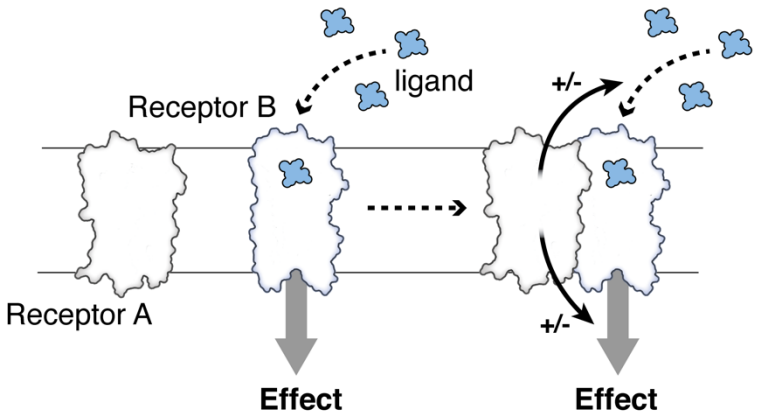

More than 20% of adults worldwide experience different types of chronic pain, which are frequently associated with several comorbidities and a decrease in quality of life. Several approved painkillers are available, but current analgesics are often hampered by insufficient efficacy and/or severe adverse effects. For instance, agonism of MOR offers the most effective treatment for severe pain, but opioids are under intense debate for their poor safety profiles and high potential for abuse, as reflected in the opioid use disorder (OUD) epidemic with >27 million people affected, more than 100,000 deaths per year, and about 145 deaths per day in the recent years in the USA (Strang *et al.*, 2020; Volkow and Collins, 2017).

Consequently, novel strategies for safe, highly efficacious treatments are highly desirable, particularly for chronic pain (Niederberger *et al.*, 2017). Aware of this problem, the National Institute of Drug Abuse (NIDA) has proposed scientific strategies for combating the opioid epidemic (Rasmussen *et al.*, 2018). Others have proposed to develop opioids with functional selectivity or biased agonism, with preferential G-protein-mediated versus β-arrestin-mediated signaling (Schmid *et al.*, 2017).

Another potential approach to harnessing the therapeutic effects of opioids involves targeting GPCR heteromers. For instance, the MOR-Gal1R heteromer localized in the ventral tegmental area (VTA), the midbrain localization of the dopaminergic cells that control reward processing is involved in the dopaminergic effects of opioids and provides a pharmacodynamic explanation for the weaker dopaminergic and euphoric properties of methadone (Cai *et al.*, 2019). Methadone is a synthetic opioid agonist used for the treatment of OUD. The mechanism by which the MOR-Gal1R heteromer is insensitive to methadone, can provide clues for finding additional molecules that poorly bind or activate

the MOR in the VTA while preserving significant activity for MOR in other nervous system regions that mediate analgesia.

## 5.1 **Case Study #2.** Unique pharmacodynamic properties and low abuse liability of the *μ*-opioid receptor ligand (S)-methadone induced by MOR heteromerizing with $Gal_1R$.

In press as **co-first author** in

Levinstein, M.[1], de Oliveira, P. A.[1], Casajuana-Martin, N.[1], Quiroz, C., Budinich, R., Rais, R., Rea, W., Ventriglia, E., Llopart, N., Casadó-Anguera, V., Moreno, E., Walther, D., Glatfelter, G., Weinshenker, D., Zarate, C., Casado, V., Baumann, M., Pardo, L., Ferré, S., Michaelides, M. **Unique pharmacodynamic properties and low abuse liability of the *μ*-opioid receptor ligand (S)-methadone**. *Molecular Psychiatry (2023)*

**Figure 5** was published as **co-first author** in

De Oliveira, P. A.[1], Moreno, E.[1], Casajuana-Martin, N.[1], Casadó-Anguera, V., Cai N-S., Camacho-Hernandez, G. A., Zhu, H., Bonifazi, A., Hall, M. D., Weinshenker, D., Newman, A. H., Logothetis, D. E., Casadó, V., Plant, L. D., Pardo, L., Ferré, S. **Preferential Gs protein coupling of the galanin Gal1 receptor in the *μ*-opioid-$Gal_1$ receptor heterotetramer**. *Pharmacological Research. 182* (2022)

[1]These authors contributed equally

### 5.1.1 Introduction

The use of TM peptides (TMPs, see *Experimental studies* in METHODS) in native tissue preparations and in animals, has provided significant evidence for the localization and function of GPCR heteromers in the brain. One recent example is the localization of heteromers of *μ*-opioid receptors (MORs) and galanin $Gal_1$ receptors (Gal1Rs) in the VTA(Moreno *et al.*, 2017; Cai *et al.*, 2019), which represents a predominant population of MOR that mediates the dopaminergic effects of opioids (Cai *et al.*, 2019). Allosteric mechanisms in the MOR-Gal1R

heteromer determine the ability of Gal1R ligands to decrease the affinity and efficacy of opioids and, importantly, a specific decrease in the potency of methadone (Cai *et al.*, 2019). This MOR-Gal1R heteromer-dependent pharmacodynamic property of methadone provided a mechanistic explanation for its weaker dopaminergic effects, blunted euphoric properties, and lower abuse liability as compared with morphine and other opioids (Cai *et al.*, 2019).

Nonetheless, it is relevant to note that methadone treatment typically consists in a racemic mixture of the two enantiomers of methadone, R ((R)-MTD) and S ((S)-MTD). Historically, it was believed the therapeutic properties of methadone were mediated by (R)-MTD (Chen, 1948), but (S)-MTD is now being considered as well, for instance, for the treatment of depression (Fava *et al.*, 2022). The mechanism of action of (S)-MTD is still not well understood and rather controversial. Its antidepressant activity has been attributed to N-methyl-D-aspartate receptor (NMDAR) antagonism (Fogaça *et al.*, 2019; Hanania *et al.*, 2019; De Martin *et al.*, 2021; Bernstein *et al.*, 2019), with an affinity for the receptor of ~2.6-7.4 $\mu$M (Gorman *et al.*, 1997), ~300 times lower than for MOR (Kristensen, 1995). Recent evidence implicates MOR agonism as a relevant antidepressant mechanism (Williams *et al.*, 2018; Klein *et al.*, 2020; Levinstein *et al.*, 2023), and whilst (S)-MTD is an antagonist for NMDAR, it is an agonist for MOR.

Could it be then that (S)-MTD is the enantiomer that provides the lower addictive liability to methadone treatment? In this study, *in vitro*, *in vivo* and *in silico* pharmacological characterization of racemic methadone, (R)-MTD and (S)-MTD was performed. The findings provide a mechanistic basis for the differential properties of the enantiomers, which may impact on their clinical utility.

### 5.1.2 Results

Comparison of the pharmacology of (R)-MTD and (S)-MTD reveals that they bind to MORs, and only with significantly higher concentrations to NMDARs (**Suppl. Figure 1**).

**(S)-MTD exhibits lower abuse liability than (R)-MTD and (R,S)-MTD but induces significant analgesic effects**

There is evidence that racemic methadone ((R,S)-MTD) is self-administered in humans (Spiga *et al.*, 1996) and rats (Martin *et al.*, 2007). However, the intravenous self-administration (IVSA) of (R)-MTD and (S)-MTD has not been reported. Moreover, depending on the dose administered, (R,S)-MTD can have either rewarding or aversive effects in rats (Steinpreis *et al.*, 1996). IVSA, the standard preclinical approach for predicting abuse liability of drugs in humans (O'Connor *et al.*, 2011), was used to evaluate the reinforcing effects of (R,S)-MTD and its enantiomers in rats. First, the group at NIDA performed dose finding experiments to determine the dose of each drug that maintained IVSA. Rats (male and female Sprague-Dawley rats) exposed to various doses of (R)-MTD readily self-administered 50 µg/kg/infusion and consumed a maximum of ~2 mg/kg at the highest dose. Rats exposed to (S)-MTD never acquired IVSA, even at high unit doses, and did not show any evidence of dose response. Nevertheless, when (R)-MTD-trained rats were switched to (S)-MTD, they showed reliable IVSA at 500 µg/kg/infusion (S)-MTD. The switched rats consumed a cumulative dose of ~30 mg/kg at the highest (S)-MTD dose.

Next, they performed IVSA studies on another cohort of rats trained on either (R)-MTD (50 µg/kg/infusion), (R,S)-MTD (100 µg/kg/infusion), or (S)-MTD (500 µg/kg/infusion) (**Figure 1a–c**). For the first 10 days of

training, rats were on a fixed-ratio 1 (FR1) schedule. During this time, rats in all three groups learned to discriminate the active from inactive lever. On the 11th session, the schedule was increased to FR5 (5 presses for 1 infusion). Whereas rats trained on (R)- and (R,S)-MTD adjusted lever press rates to maintain stable infusion rates, rats trained on (S)-MTD did not. A dose response assessment of IVSA was also performed (**Figure 1d**). Rats trained on (R)- or (R,S)-MTD displayed the typical inverted-U shaped dose-response curve, but rats trained on (S)-MTD showed no evidence of dose response. Rats given (R)-MTD showed peak infusion rates at 25 µg/kg, while rats given (R,S)-MTD peaked at 50 µg/kg. Notably, rats trained on (R,S)-MTD had more infusions at the peak unit dose than those on (R)-MTD, and the (R,S)-MTD curve was significantly shifted to the right indicating that larger drug amounts were required to reach the same level of reinforcement.

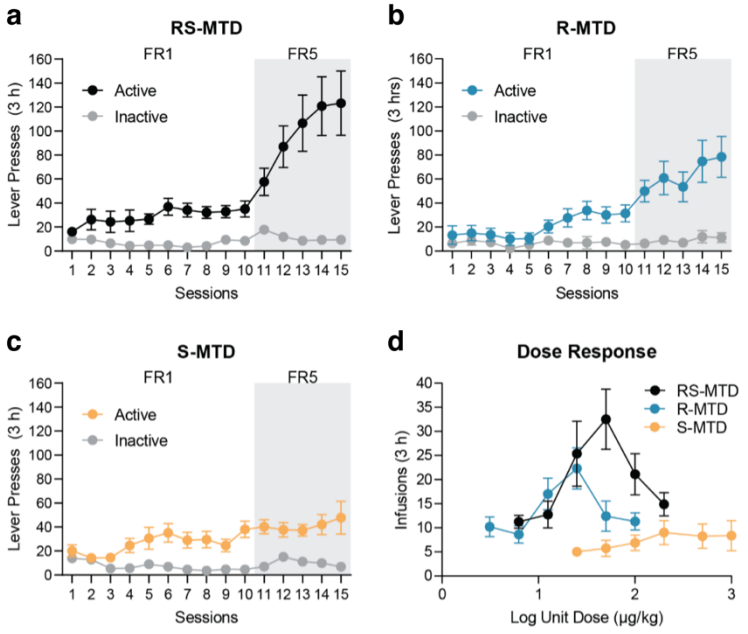


*(Figure legend on next page)*

*Figure 1. Differential abuse liability profile of (R,S)-MTD, (R)-MTD, and (S)-MTD. (a-c) Lever presses during IVSA training for (R,S)-MTD (100 µg/kg/infusion, **a**), (R)-MTD (50 µg/kg/infusion, **b**), and (S)-MTD (500 µg/kg/infusion, **c**). **(d)** IVSA dose responses for (R,S)-MTD, (R)-MTD, and (S)-MTD.*

Analgesic effects were also analyzed in the same strain of rats. In the hotplate, (R,S)-MTD, (R)-MTD, and (S)-MTD demonstrated full MOR agonistic activity, with $ED_{50}$ values (%MPE, maximum possible effect) of 1.2, 0.5 and 17.9 mg/kg, respectively (**Suppl. Figure 2**). In summary, these results demonstrate a significant dissociation between the rewarding (dopaminergic) and analgesic (non-dopaminergic) effects of (S)-MTD.

**Divergent pharmacodynamic effects of (R)-MTD and (S)-MTD at the MOR-Gal1R heteromer**

BRET experiments were performed to evaluate differences in the intrinsic efficacy of (R,S)-MTD, (R)-MTD and (S)-MTD at the MOR (**Figure 2a**). MOR-Rluc and Gi-YFP constructs were transiently co-transfected to HEK-293T cells, and concentration-response curves of (R,S)-MTD, (R)-MTD, and (S)-MTD were analyzed for $E_{max}$ and $EC_{50}$ values (**Figure 2b-d**). As expected, $E_{max}$ for (S)-MTD was significantly lower than for (R)-MTD (about 30% lower, **Figure 2c**), and $EC_{50}$ for (S)-MTD was significantly higher than for (R)-MTD (about 10 times; **Figure 2d**). Thus, relative to (R)-MTD, (S)-MTD is a partial and less potent MOR agonist.

CODA-RET experiments were then performed to determine whether MOR-Gal1R heteromerization might determine the specific pharmacological profile of (S)-MTD (see Methods in the original publication) (**Figure 2g**). HEK-293T cells were co-transfected with MOR fused to nRLuc (MOR-nRLuc), Gal1R was fused to cRLuc (Gal1R-cRLuc) and Gi-YFP (**Figure 2h-j**). In the presence of Gal1R, no detectable increase of response (BRET ratio) could be obtained with (S)-MTD, while

the dose-response curve of (R,S)-MTD was shifted to the right, with an $EC_{50}$ value significantly higher than for R-MTD (~10-fold; **Figure 2j**).

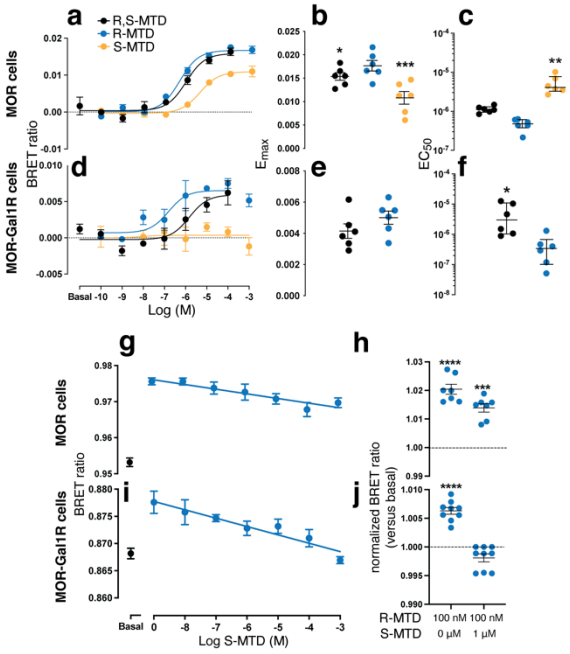


*Figure 2. MOR-Gal1R heteromer-dependent loss of efficacy of (S)-MTD (**a-c, g-h**), BRET experiments in HEK-293T cells cotransfected with MOR fused to RLuc and the α subunit of the Gi protein fused to YFP, (**d-f, i-j**). CODA-RET experiments in HEK-293T cells cotransfected with MOR fused to nRLuc, Gal1R fused to cRLuc and Gi-YFP (schematically shown in g). In b and h, representative experiments with concentration-responses of (R,S)-MTD (black), (R)-MTD (blue), and (S)-MTD (orange); values represent the mean ± standard error of the mean of triplicates; in **b-c** and **e-f**, corresponding $E_{max}$ and $EC_{50}$ values from 6 independent experiments with triplicates, shown as dots and presented with the mean ± standard error of the mean or median with interquartile ranges, respectively; asterisks are compared to (R)-MTD values. In **g** and **i**, representative experiments of the effect of increasing concentrations of (S)-MTD on BRET and CODA-RET values obtained with (R)-MTD at 100 nM; values represent the mean ± SEM of triplicates; in **h** and **j**, corresponding BRET and CODA-RET values of the effect of (R)-MTD (100 nM) in the presence and absence of (S)-MTD (1 µM) from 7 and 9 independent experiments with triplicates, shown as dots and presented with the mean ± standard error of the mean; asterisks are compared to basal values.*

These results, therefore, indicate that (S)-MTD, but not (R)-MTD, changes its pharmacological profile and loses its efficacy for the MOR when forming heteromers with Gal1R. This implies that the changes in the pharmacological profile of (R,S)-MTD within the MOR-Gal1R heteromer,

as previously described, depend on the modified pharmacodynamic properties of (S)-MTD. (S)-MTD seems therefore to bind to the MOR but to have lost its efficacy, acting as a MOR antagonist in the MOR-Gal1R heteromer. Consistent with this, increasing concentrations of (S)-MTD progressively counteracted the effect of a minimal concentration with maximal effect of (R)-MTD (10 μM) (**Figure 2k**). At the highest concentration of (S)-MTD (1 mM), the effect of (R)-MTD was completely blocked, and CODA-RET measurements were not significantly different from basal values (**Figure 2l**). As a control, the same design was applied with BRET experiments with the MOR alone. In this case, the highest concentration of (S)-MTD (1 mM) did not counteract the effect of (R)-MTD (10 μM) (**Figure 2e-f**), and only decreased its effect to the expected maximal level of efficacy of (S)-MTD.

**Binding modes of (S)-MTD and (R)-MTD in MOR**

The recently reported structure of MOR in complex with fentanyl (Zhuang *et al.*, 2022) can be used as a template to understand the pharmacodynamic differences among the enantiomers of methadone at the molecular level. We first performed five replicas of unbiased 1 μs molecular dynamics (MD) simulations of (S)-MTD and (R)-MTD docked into the MOR monomer. *Ab initio* conformational analysis and geometry optimization of (S)- and (R)-MTD were performed at the HF/6-31G* level of theory to obtain the right configuration of the ligand, and the obtained energy minima were docked into the orthosteric binding cavity using MOE (Chemical Computing Group Inc., Montreal, Quebec, Canada) (see METHODS). RMSD of the simulations show that the proposed docking models of (S)-MTD and (R)-MTD remained highly stable (**Figure 3a**). In these models, the protonated amine of (S)-MTD and (R)-MTD forms the conserved ionic interaction with D149$^{3.32}$, and both phenyl groups adopt a

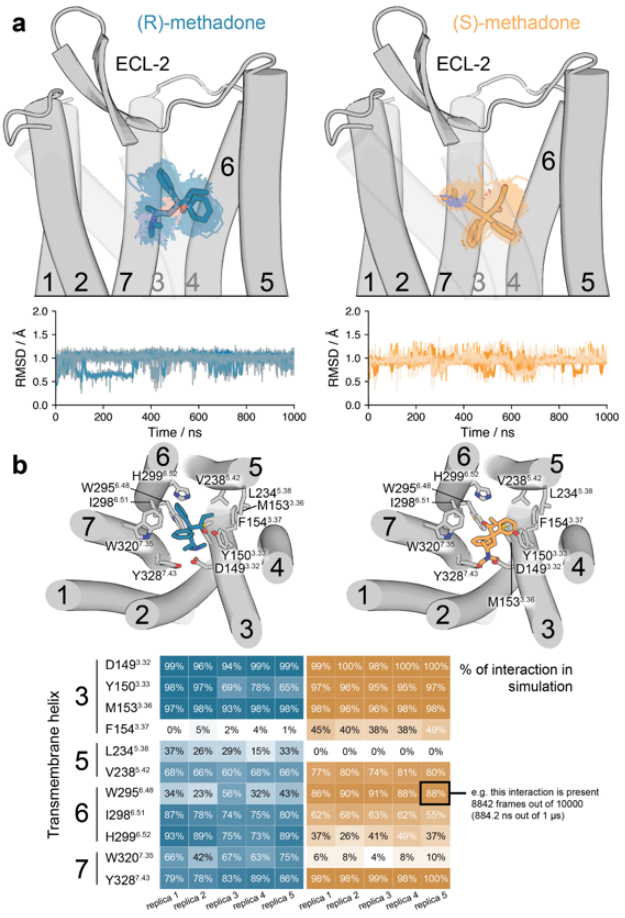


*Figure 3. MD simulations of MOR bound to (R)-MTD and (S)-MTD. (a) Representative structures (solid sticks) and evolution (lines) of (R)-MTD (in blue) and (S)-MTD (in orange) in complex with MOR (gray cylinders, only the initial structure is shown) as devised from five replicas of unbiased 1 µs MD simulations. The stability of the ligand-receptor complexes was analyzed via rmsd of the heavy atoms of (R)-MTD (blue lines) and (S)-MTD (orange lines). The low rmsd values indicate that both enantiomers remained highly stable at the orthosteric site. (b) Detailed views of (R)-MTD and (S)-MTD and their receptor interacting side chains. Calculated frequency contacts (%) between side-chain residues of MOR involved in stable interactions with (R)-MTD or (S)-MTD during MD simulations, color-coded according to the frequency of contacts (https://getcontacts.github.io/).*

"V" shaped conformation in the orthosteric binding site but, importantly, with significant differences. In (R)-MTD, both phenyl rings point up to form T-shaped aromatic interactions with H299$^{6.52}$ and W320$^{7.35}$, whereas the phenyl rings of (S)-MTD point down to interact with W295$^{6.48}$ in a

"sandwich" mode in which the aromatic Trp ring is between both phenyl rings (**Figures 3b** and **4** show a detailed analysis of the binding modes). We suggest that the phenyl ring of (S)-MTD positioned between W295$^{6.48}$ and TM5, absent in (R)-MTD, restricts the necessary movement of W295$^{6.48}$ for activation (Zhuang *et al.*, 2022; Huang *et al.*, 2015), which explains the decreased ability of (S)-MTD to activate MOR.

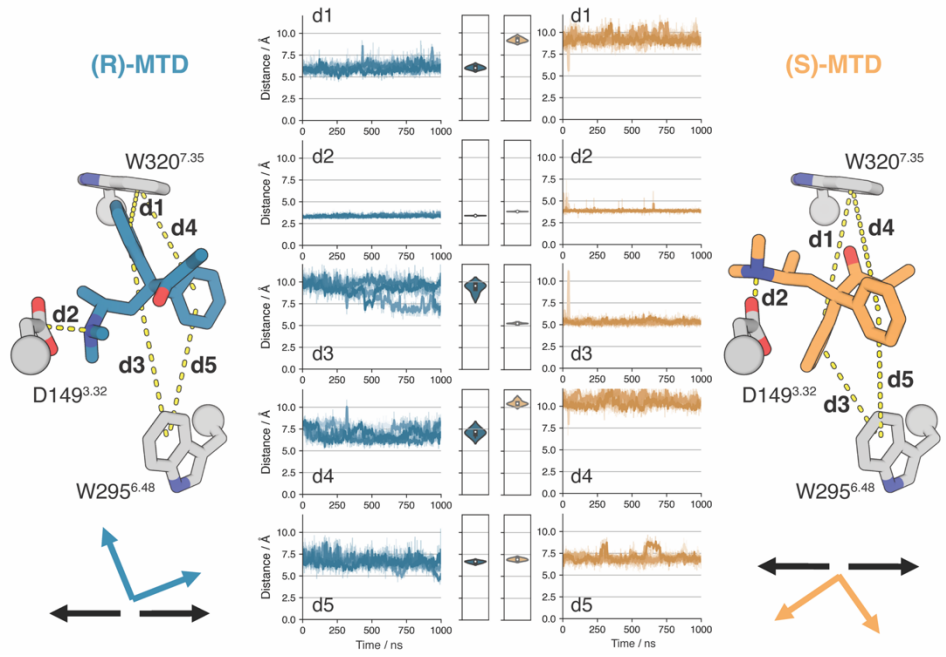


*Figure 4. Representative distances between MOR and (R)-MTD and (S)-MTD during MD simulations. Quantification of the distance between the Cβ atom of D1493.32 and the protonated amine (distance d2) of (R)-MTD (left, in blue) and (S)-MTD (right, in orange), and between the center of mass of both phenyl rings and the center of mass of W2956.48 (d3 and d5 distances) and W3207.35 (d1 and d4 distances) during five replicas of unbiased 1 μs MD simulations. Violin plots represent the distribution of the mean distance for each replicate.*

## MOR-Gal1R quaternary structure reveals a change in homomeric interfaces on MOR

To understand the inability of (S)-MTD to activate MOR in the presence of Gal1R, at the molecular level, we first needed to computationally model

the MOR-Gal1R heteromer. The putative homomeric and heteromeric structure of MOR-Gal1R was evaluated by bimolecular fluorescence complementation (BiFC) experiments in combination with disruptive peptides targeting a specific dimer interface. In these experiments, HEK-293T cells were co-transfected with receptors separately fused to the non-fluorescent hemiproteins (complementary halves) of the yellow fluorescent protein (N-terminal, nYFP; and C-terminal, cYFP).

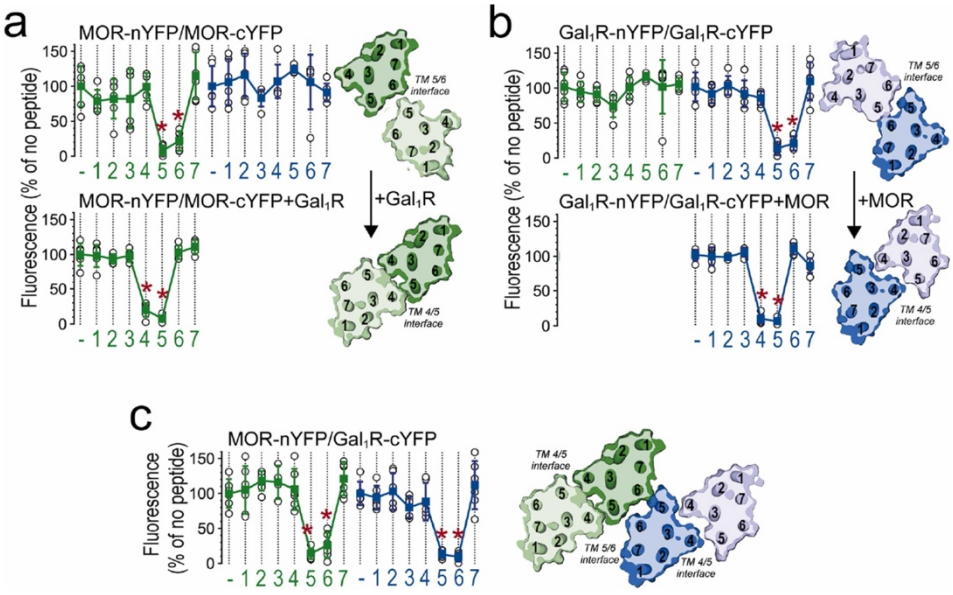


*Figure 5. TM interfaces of MOR and Gal1R homomers and heteromers in BiFC experiments. Results from BiFC experiments in HEK-293T cells co-transfected with MOR-nYFP and MOR-cYFP (**a**), Gal1R-nYFP and Gal1R-cYFP (**b**) or MOR-nYFP and Gal1R-cYFP (**c**), in the absence (-) or the presence of the indicated TM peptides (TMPs) (at 4 μM; numbered 1–7) from MOR (green symbols and plots) or Gal1R (blue symbols and plots), and in the absence or the presence of the co-transfected non-fused Gal1R or MOR (lower graphs in a and b, respectively); fluorescence values (in means ± S.D.) are expressed as the percentage of the fluorescence in the absence (-) of the indicated TMPs (n = 6, with triplicates); * represent significantly lower values as compared to control values (p < 0.001; one-way ANOVA followed by Dunnett's multiple comparison tests). The schemes in **a** and **b** illustrate the corresponding interfaces of the MOR-MOR (**a**) and Gal1R-Gal1R (**b**) homomers in the absence (upper) and presence (lower) of Gal1R and MOR, respectively. The scheme in c illustrates the computational model of the MOR-Gal1R heterotetramer built using the experimental interfaces predicted in panels **a–c** (TM 5/6 for heterodimerization and TM 4/5 for homodimerization; see text).*

Fluorescence was then measured in the absence or presence of synthetic peptides with the amino acid sequence of all TMs of both receptors (TM1 to TM7 of MOR and Gal1R). The group at UB could first demonstrate that fluorescence of MOR-nYFP/MOR-cYFP was only reduced in the presence of TM5 and TM6 peptides of MOR (**Figure 5a, upper graph**) and fluorescence of Gal1R-nYFP/Gal1R-cYFP was reduced by TM5 and TM6 peptides of Gal1R (**Figure 5b, upper graph**), pointing to the involvement of the TM 5/6 interface in the MOR-MOR and Gal1R-Gal1R homomers. The formation of Gal1R homodimers in living cells is also supported by literature (Wirz *et al.*, 2005). Notably, when MOR-nYFP and MOR-cYFP were co-transfected with non-fused Gal1R, fluorescence was only significantly decreased by TM4 and TM5 peptides of MOR (**Figure 5a, lower graph**), and when Gal1R-nYFP and Gal1R -cYFP were co-transfected with non-fused MOR, fluorescence was decreased by TM4 and TM5 peptides of Gal1R (**Figure 5b, lower graph**). Thus, the interface for both MOR-MOR and Gal1R-Gal1R homodimers changed in the presence of the other non-fused receptor from a TM 5/6 to a TM 4/5 interface (**Figure 5a,b**). Finally, fluorescence of MOR-nYFP/Gal1R-nYFP was significantly reduced by TM5 and TM6 peptides of both MOR and Gal1R (**Figure 5c**), pointing to a TM 5/6 interface for the MOR-Gal1R heteromer. These data reveal TM 5/6 as the most stable interface for MOR-MOR and Gal1R-Gal1R homomers, but also for the MOR-Gal1R heteromeric interface. Significantly, the results suggest a competition for the TM 5/6 interface and indicate an obligatory homodimeric structure of MOR and Gal1R, for which their interface changes to a less favorable TM 4/5 interface in the MOR-Gal1R heteromer.

## Interface change in MOR stabilizes a different conformation of its binding pocket

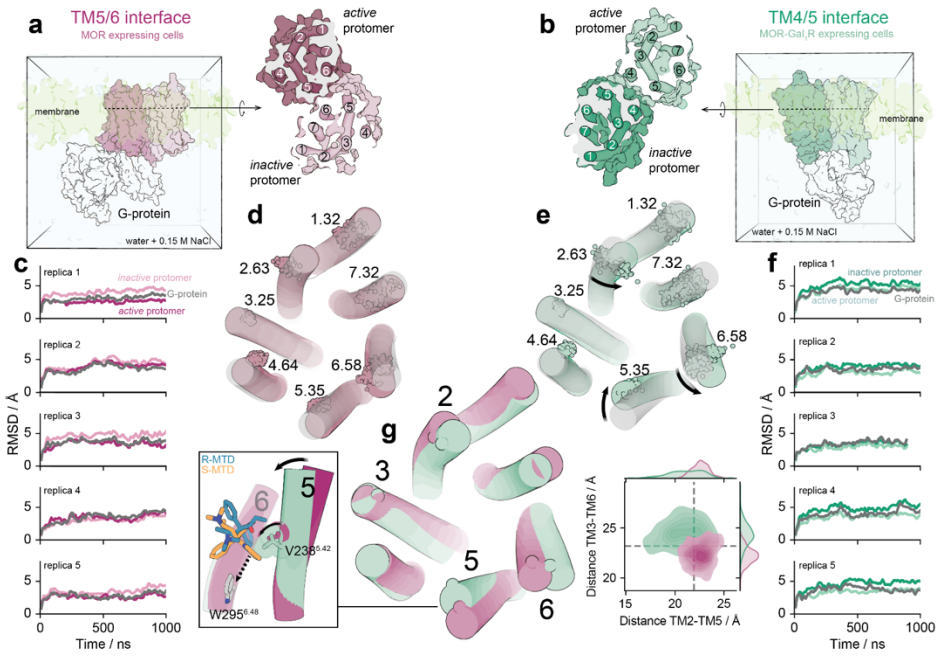


*Figure 6. MD simulations of the MOR-MOR heteromer. (**a-b**) Parallel to the membrane and extracellular views of the MOR-MOR heteromer, constructed via the TM 5/6 (**a**) or TM 4/5 (**b**) interface, as explained in METHODS. (**c-f**) Influence of the inactive MOR on the conformation of active MOR protomer in the TM 5/6 (**c-d**) and TM 4/5 (**e-f**) interfaces as devised by five replicas of unbiased 1 μs MD simulations. The stability of the complexes was analyzed via rmsd of inactive and active MOR protomers and the G-protein (**c, f**). Superimposition of a representative TM bundle of active MOR, and the evolution of the Ca atoms (spheres) of the extracellular amino acids at the Ballesteros-Weinstein position 1.32, 2.63, 3.25, 4.64, 5.35, 6.58, and 7.32, during the MD simulations of the MOR-MOR heteromer, modelled in the TM 5/6 (**d**) and TM 4/5 (**e**) interfaces, to the cryo-EM structure of MOR bound to fentanyl (8EF5, in light colour). Black arrows represent movements of the extracellular part of the helices relative to the fentanyl-bound structure. The xy plane is as defined by the Orientations of Proteins in Membranes (OPM) (Lomize et al., 2006). (**g**) Superimposition of representative TM bundles of active MOR in the TM 5/6 (purple) and TM 4/5 (green) interfaces. Contour plots of the distances between N129$^{2.63}$ in TM2 and E231$^{5.35}$ in TM5 (distance TM2-TM5) and between C142$^{3.25}$ in TM2 and K305$^{6.58}$ in TM 6 (distance TM2-TM6) during the MD simulations. Distributions of these distances are shown in the axes. These results show that, in contrast to the TM 5/6 interface, TM5 moved the extracellular part inward (black arrow) in the TM 4/5 interface. This movement relocated the position of the key V238$^{5.42}$ (black arrow), and the phenyl ring of (S)-MTD toward W295$^{6.48}$ (dashed arrow).*

The difference in the pharmacodynamic profile of (S)-MTD in presence or absence of Gal1R might be then due to the change in MOR homomeric interfaces. Thus, we hypothesized that the MOR-MOR homodimer interacting via the TM 4/5 interface disables (S)-MTD to activate MOR. To test this hypothesis, we performed five replicas of unbiased 1 μs MD simulations of the MOR-MOR homodimer, constructed via both the TM 5/6 (not interacting with Gal1R) and TM 4/5 (interacting with Gal1R) interfaces, in complex with Gi (see METHODS). The stability of the different protein elements in the simulations was monitored, showing that no large structural rearrangements were happening (**Figure 6c,f**). Nonetheless, when observed from the extracellular site, significant differences were spotted on the TM 4/5 interface active receptor when compared to the reference structure (the cryo-EM structure of MOR bound to fentanyl) (**Figure 6d,e**). In contrast to the TM 5/6 interface, TM5 of the active Gi-bound protomer moved the extracellular part of TM5 inward in the TM 4/5 interface (**Figure 6g**). Importantly, this movement of TM5 relocated the position of the key V238$^{5.42}$ (**Figure 6g, inset**).

**Molecular mechanism by which (S)-MTD acts as an MOR antagonist in the MOR-Gal1R heteromer**

We found the potential molecular mechanism behind the lower abuse liability of (S)-MTD, involving the interaction between MOR and Gal1R. The presence of Gal1R reconfigures the MOR-MOR homodimer, inducing a small conformational change on its binding pocket. **Figure 7** summarizes these findings. (R)- and (S)-MTD binding modes are considerably different despite being almost structurally identical. Both molecules have the charged amine and the the -CO-CH2-CH3 moiety located similarly, but the orientation of the phenyl rights is the opposite (**Figure 7a,b)**. In the context of the heteromer, the MOR-MOR TM 5/6

interface (**Figure 7c**), W295$^{6.48}$ is only partially restricted (depicted as flexible ellipses) by the phenyl ring of (S)-MTD because the dynamic behavior of the ligand is not fully constrained by the partner protomer (depicted as flexible arrows). In contrast, in the TM 4/5 interface (**Figure 7d**), the inward movement of V238$^{5.42}$ fully constrained (depicted as a single arrow) the phenyl ring of (S)-MTD, maintaining W295$^{6.48}$ in the inactive conformation (depicted as a single ellipse). (R)-MTD binding mode triggers the activation of the receptor, and while (S)-MTD is less able in a TM 5/6 interface (MOR expressing cells), it is totally unable in the TM 4/5 interface (MOR-Gal1R expressing cells), acting as a competitive antagonist (occupying the binding pocket but unable to activate the receptor).

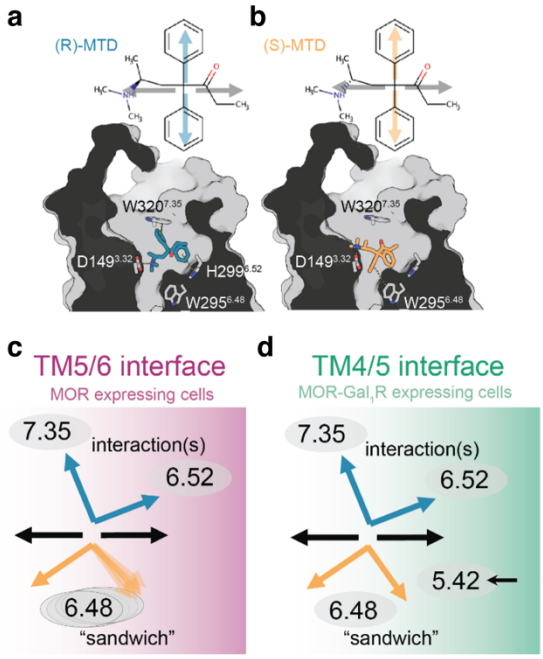


*Figure 7. Summary of the molecular findings. (a-b) Schematic 2D representation of (R)- and (S)-MTD. Grey arrows represent groups of the ligand located toward the conserved protonated amine (left) and toward the -CO-CH2-CH3 moiety (right). The phenyl groups of methadone are depicted by either blue (R)- or orange (S)- arrows. Docking and MD-simulated models (**Figures 3-4**) of (R)- and (S)-MTD bound to the MOR. (continues)*

*The phenyl rings, in a "V" shaped conformation, point up to interact with H299$^{6.52}$ and W320$^{7.35}$ in (R)-MTD, and point down to interact with W295$^{6.48}$ in (S)-MTD.* **(c-d)** *In the TM 5/6 interface the phenyl ring of (S)-MTD (flexible arrows) partially restricts the conformation of W295$^{6.48}$ (flexible ellipses), whereas in the TM 4/5 interface V238$^{5.42}$ restricts the conformation of the phenyl ring (single arrow) and in consequence W295$^{6.48}$ (single ellipse) in the inactive conformation.*

### 5.1.3 Discussion

(R,S)-MTD is a United States Drug Enforcement Adninistration (DEA) Schedule II controlled medication with known abuse liability that is prescribed for pain management and treatment of OUD. However, the individual contributions of its enantiomers to its abuse liability and clinical efficacy are not well understood. We found that both (R)-MTD and (S)-MTD produced full agonistic effects on analgesia but only (R)-MTD was reliably self-administered. These findings are in agreement with results from recent studies indicating that (S)-MTD does not lead to reinforcing effects, physical dependence nor withdrawal signs in rats (Henningfield *et al.*, 2022) and that it lacks opioid effects, or withdrawal signs and symptoms in humans (Fava *et al.*, 2022), suggesting that the abuse liability of (R,S)-MTD is mediated by (R)-MTD and not by (S)-MTD. Indeed, our data indicate that (S)-MTD can attenuate the abuse liability of (R)-MTD under some conditions.

The following study hence presents the involvement of a GPCR heteromer in the addictive liability of opioids. This brings the opportunity of finding alternative therapies to the standard opioid treatment, with less adverse effects. For instance, apart from the use of (S)-MTD for the treatment of pain, a strategy could be to target Gal1R, or the complex. In the previous studies on the MOR-Gal1R heteromer, we provided in vitro evidence in mammalian transfected cells and in situ and in vivo evidence in the rat VTA for a heteromer-dependent allosteric interaction by which Gal1R ligands decrease the affinity of MOR ligands and antagonize MOR-

mediated G-protein activation, signaling and dopaminergic activation (Moreno *et al.*, 2017; Cai *et al.*, 2019). Therefore, development of small molecule agonists that target the Gal1R in the MOR-Gal1R heteromer represents a promising approach to counteract the unwanted dopaminergic effects of opioids while preserving or even potentiating their analgesic effects at the spinal level, as previously described (Hua *et al.*, 2004). Thus, a combination treatment of MOR agonists and Gal1R ligands might potentially be beneficial for pain avoiding addiction.

## 5.1.4 Supplementary Material

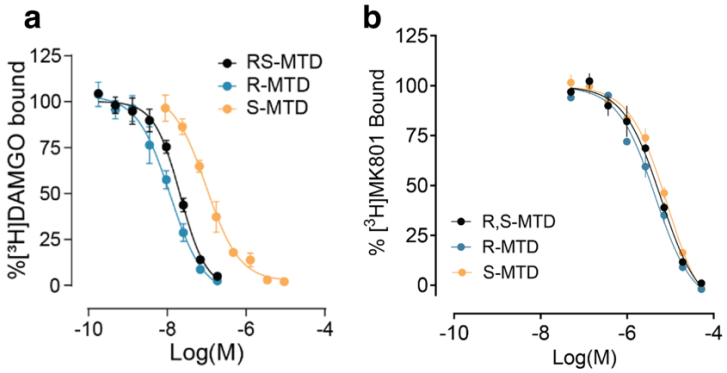


*Supplementary Figure 1. Competition binding assays of (S)-MTD (orange), (R)-MTD (blue), or (R,S)-MTD (black) versus* ***(a)*** *[3H]DAMGO and* ***(b)*** *[3H]MK801.*

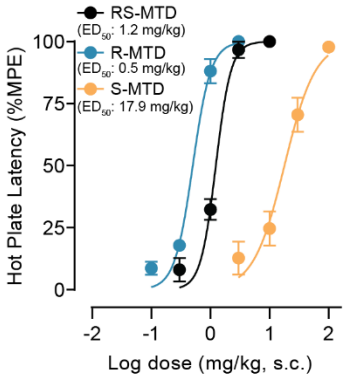


*Supplementary Figure 2. Dose response curves of hotplate latency for (R,S)-MTD (black), (R)-MTD (blue) and (S)-MTD (orange).*

# 6 CHAPTER III

*Receptor heteromerization alters G-protein binding*

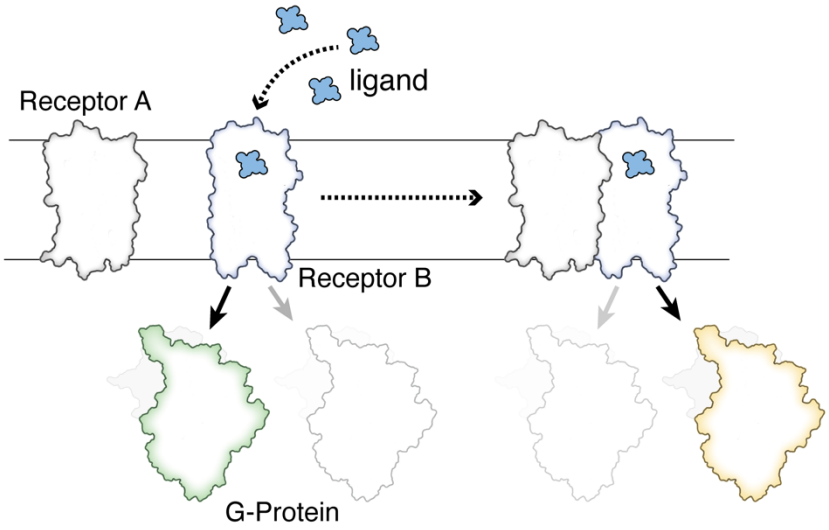

GPCRs can couple to four classes of G-proteins: Gi/o, Gq, Gs/olf, and G12/13. The coupling preference varies between receptors, some receptors being more promiscuous than others (as analyzed in Figure 1 of (Sandhu *et al.*, 2022)). A vast number of studies have tried to unravel the determinants of GPCR-G-protein coupling selectivity, which still presents a challenge. Examples of these studies involve structure solution (Liu *et al.*, 2021; Alegre *et al.*, 2021; Huang *et al.*, 2022), combination of structural and bioinformatics analysis (Flock *et al.*, 2017), and others (Jelinek *et al.*, 2021; Okashah *et al.*, 2019; Jang *et al.*, 2023). In the last few years, some publications massively studied combinations of GPCR-G-protein couplings (Inoue *et al.*, 2019; Avet *et al.*, 2022), unified in this meta-analysis (Hauser *et al.*, 2022), and recently in combination with Machine Learning methods (Masuho *et al.*, 2023).

G-protein selectivity and promiscuity might include other factors such as disordered regions like the C-terminus or intracellular loops (Sadler *et al.*, 2023), or membrane composition, which has been shown to modify the preference of the $\beta_2$ adrenergic receptors to bind Gi or Gs subtypes (Strohman *et al.*, 2019). It is, in fact, Gi coupling that has cardioprotective effects (Xiao *et al.*, 1999), so tuning the G-protein coupling pattern can be relevant therapeutically.

In addition to these factors, GPCR heteromerization can determine changes in G-protein binding, however, how heteromerization can modify the recruitment of signaling G-proteins is not completely understood. In this chapter we have studied the mechanisms by which heteromerization facilitates non-canonical Gal1R signaling to Gs in the presence of MOR, in the MOR-Gal1R heteromer (Case Study #3); and 5-$HT_{2A}$R signaling through non-canonical Gi/o coupling rather than canonical Gq/11 coupling, in the $CB_1$R-5-$HT_{2A}$R heteromer (Case Study #4).

## 6.1 **Case Study #3.** MOR induces a G-protein selectivity switch on Gal1R.

Published as **co-first author** in

De Oliveira, P. A.[1], Moreno, E.[1], Casajuana-Martin, N.[1], Casadó-Anguera, V., Cai N-S., Camacho-Hernandez, G. A., Zhu, H., Bonifazi, A., Hall, M. D., Weinshenker, D., Newman, A. H., Logothetis, D. E., Casadó, V., Plant, L. D., Pardo, L., Ferré, S. **Preferential Gs protein coupling of the galanin Gal1 receptor in the *μ*-opioid-Gal1 receptor heterotetramer**. *Pharmacological Research. 182* (2022)

[1]These authors contributed equally

### 6.1.1 Introduction

It has been suggested that a common quaternary structure of a GPCR heteromer is a heterotetramer constituted by a dimer of dimers, one of them coupled to Gs/olf (or Gs) and the other to Gi/o (or Gi). This assembly provides the framework for the canonical Gs-Gi antagonistic interaction at the adenylyl cyclase (AC) level (type III allosterism or allosterism through the effector) (Ferré *et al.*, 2022).

MOR is a Gi-coupled receptor and constitutes the main target for both the analgesic and unwanted side effects of opioids (see above). Numerous studies have provided significant insights about the structural information and signaling properties of MOR and, although controversial, its capability to form homo/heterodimers (as shown in CHAPTER II). Prior to the discovery of MOR-Gal1R heteromers, other studies suggested the existence of heteromerization of MOR with different GPCRs, including the MOR-δ opioid receptor, claimed as a main target for the analgesic effects of opioids (Gomes *et al.*, 2016). Gal1R has also been described as preferentially coupled to Gi and potentially to Gq/11 proteins (Lang *et al.*,

2015). Gal1R localizes to several regions of the central nervous system and mediates many functions related to the neuromodulatory role of the neuropeptide galanin (Lang *et al.*, 2015). The cryo-electron microscopy (cryo-EM) structure of Gal1R in its monomeric form bound to galanin and coupled to Gi was recently solved (Duan *et al.*, 2022; Jiang and Zheng, 2022). Similar to MOR, there is compelling evidence for the ability of Gal1R to homomerize (Wirz *et al.*, 2005) and to form heteromers with several different GPCRs other than MOR (Fuxe *et al.*, 2012).

The goal of the present study is to further complement the current knowledge on the quaternary structure and function of the MOR-Gal1R heteromer. The results demonstrated a tetrameric structure, but unexpectedly, constituted by a MOR homodimer coupled to Gi and a Gal1R homodimer coupled to Gs. The latter (Gal1R-Gs) was never described before in literature. The MOR-Gal1R heterotetramer provides the framework for the canonical Gs-Gi antagonist interaction at the AC level, and we found that the heteromerization-dependent switch of the coupling of Gal1R from Gi to Gs involves a change in its homodimeric interface.

## 6.1.2 Results

**The heterotetrameric structure of MOR-Gal1R is confirmed with TIRF**

Complementing the results of BiFC shown in CHAPTER II, the group at the Northeastern University in Boston determined the preferential number and composition of protomers in the MOR-Gal1R heteromer, by counting the number of protomers assembled at the surface of live HEK-293 T cells using Total Internal Reflection Fluorescence (TIRF) miscroscopy. To do that, monomeric teal fluorescent protein 1 (mT) was fused to the C-terminus of Gal1R and monomeric cherry (mC) to the C-terminus of MOR

(mT-Gal1R and mC-MOR, respectively) to allow for high-resolution, high signal-to-noise TIRF imaging. First, they expressed mT-Gal1R alone in HEK293T cells and used photobleaching to determine the number of fluorescence-tagged protomers that formed each fluorescent particle. Approximately 75% of the fluorescent particles had two-photobleaching steps, indicating the preferential formation of Gal1R-Gal1R homodimers (**Figure 1a,b**). The remaining particles were monomeric, and no higher-level oligomers were observed. Similar results (preferential formation of MOR-MOR homodimers) were obtained when mC-MOR was expressed alone (**Figure 1c**). Furthermore, they incubated cells with peptides TM4, TM5, TM6 or TM7 of MOR. In agreement with the results obtained with BiFC (see CHAPTER II), TM 5 and TM6, but not TM4 or TM7, altered the composition of the fluorescent particles to primarily monomeric, indicating a significant involvement of TM5 and TM6 helices in the formation of the MOR-MOR interface. As expected, mT-Gal1 receptor homodimers were not disrupted following incubation of the cells with these MOR peptides (**Figure 1b**).

Next, they studied colocalized fluorescent particles formed when mC-MOR and mT-Gal1R were expressed together in the same cells (**Figure 1d,e**). The majority of the colocalized particles were tetramers composed by two protomers each of MOR and Gal1R, heteromers of homomers. The selective disruption of these complexes with peptides TM5 and TM6, but not TM4 or TM7, peptides of MOR is in complete agreement with our previous finding with BiFC experiments (CHAPTER II) indicating that the interface of the MOR-Gal1R heteromer also involves the TM5 and TM6 helices of the MOR. Notably, particles studied following incubation of the cells with TM4 of MOR were trimeric, containing a single MOR protomer colocalized with a Gal1R-Gal1R homodimer, also confirming the key role

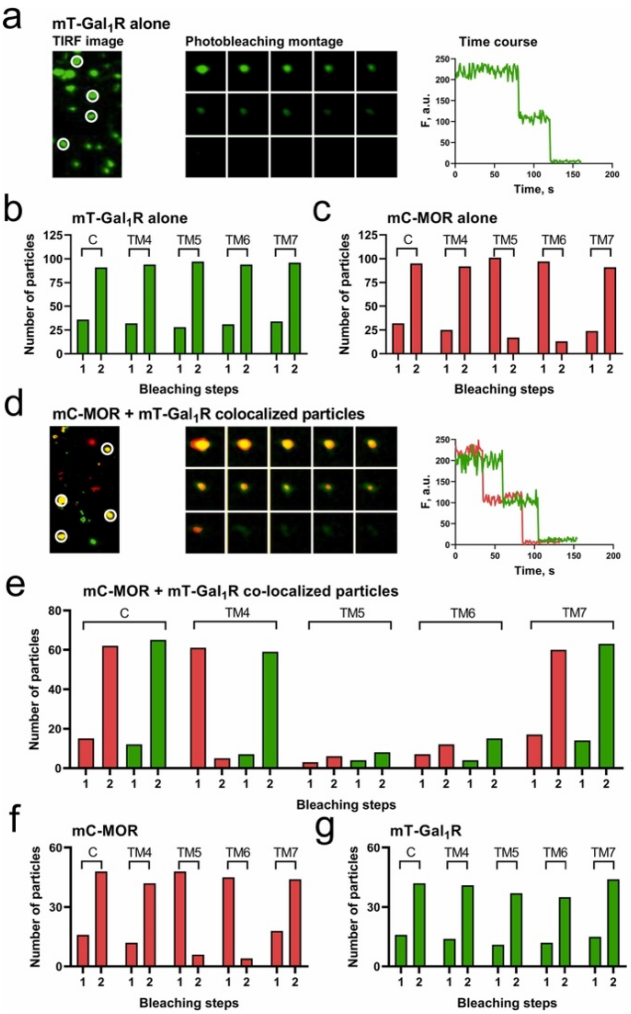


*Figure 1. Heterotetrameric structure of the MOR-Gal1R heteromer in TIRF experiments.* ***(a)*** *In the left panel, representative TIRF image showing fluorescent particles formed by mT-Gal1R in HEK-293 T cells; in the middle and right panels, example of a single mT-Gal1R particle with the time course for the change in fluorescence intensity (arbitrary units) showing two-step photobleaching. (****b-c)*** *Results summarizing the number of bleaching steps for mT-Gal1R or mC-MOR expressed separately and studied in the absence (C, control) or presence of the indicated MOR TM peptides (at 1 μM).* ***(d)*** *In the left panel, representative TIRF image showing fluorescent particles formed by mT-Gal1R (green), mC-MOR (red) separate and colocalized (yellow); in the middle and right panels, example of a single colocalized particle with the time course for two-photobleaching steps each for mT-Gal1R and mC-MOR, indicating a heterotetramer.* ***e.*** *Result summarizing the composition of colocalized particles studied in the absence (C, control) or presence of the indicated MOR TM peptides (at 1 μM).* ***(f-g)*** *Analysis of the non-colocalized mC-MOR and mT-Gal1R particles from cells expressing both receptors studied in the absence (c, control) or presence of the indicated MOR TM peptides (at 1 μM). Data represent particle counts from 4 to 6 cells per condition studied.*

for TM4 in the MOR-MOR homodimer (TM 4/5 interface) of the heterotetramer (**Figure 1e**). Finally, we assessed the stoichiometry of mCherry-tagged MOR particles that were not colocalized with Gal1R in cells co-transfected with mT-Gal1R and mC-MOR. In agreement with the stoichiometry of isolated mC-MOR (**Figure 1c**), these assemblies were primarily dimeric but were disrupted when cells were incubated with TM5 and TM6 but not TM4 or TM7 of MOR (**Figure 1f**). The isolated mT-Gal1Rs also preferentially formed dimers, and as expected these complexes were not disrupted by incubation with TM peptides of MOR (**Figure 1g**). Altogether, these data confirm the previous results from BiFC experiments (CHAPTER II) and demonstrate that, in HEK-293T co-transfected cells, the MOR-Gal1R heteromer is a heterotetramer, a heteromer of MOR-MOR and Gal1R-Gal1R homomers, in which homodimerization occurs via the TM 4/5 interface and heteromerization occurs via the TM 5/6 interface.

**Molecular basis for the interface change**

The observed changed in the interface preference of the MOR and Gal1R homodimers was analyzed by computational methods. Sequence alignments of key regions were extracted from the GPCRdb (Isberg *et al.*, 2016; Kooistra *et al.*, 2021), and structures for the complexes were built following the protocol in METHODS (*Building dimers* section). Both MOR and Gal1R belong to the same subfamily of GPCRs (peptide receptors) and albeit not sharing a very high sequence identity (22%), they have a rather similar structure (1-1.3 Å of global RMSD in structure superimposition, **Suppl. Figure 1**). Therefore, structure comparison was rather straightforward.

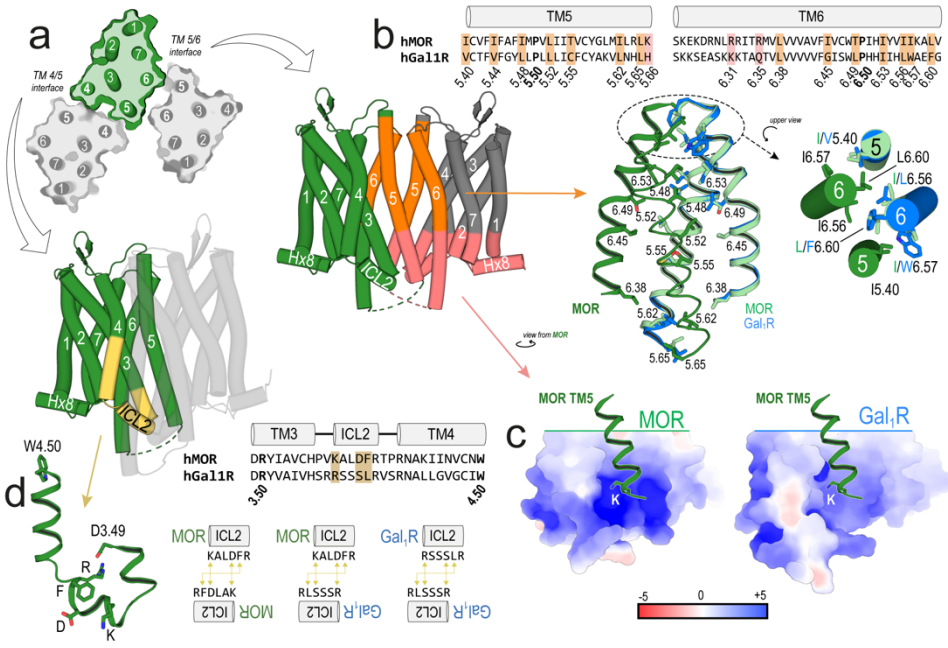


*Figure 2. Sequence analysis of the MOR-MOR, MOR-Gal1R, and Gal1R-Gal1R interactions at the TM 5/6 (a-c) and TM 4/5 (a,d) interfaces.* ***(a)*** *Schematic representation of the proposed interfaces in upper and side views, in which a reference MOR protomer is shown in green and the interacting protomer in gray.* ***(b)*** *Sequence alignment of TMs 5 and 6 of MOR and Gal1R (top panels). In the alignment, residues are highlighted in orange and pink in accordance to the areas that are then further detailed. View of the extensive network of hydrophobic interactions at the TM 5/6 interface (orange-colored cylinders).* ***(c)*** *Electrostatic surface potentials of the intracellular domain (pink-colored cylinders) of MOR (left panel) and Gal1R (right panel) protomers, calculated using the APBS program with the nonlinear Poisson-Boltzmann equation and contoured at ±5kT/e (negatively and positively charged surface areas are colored red and blue, respectively).* ***(d)*** *Detailed view of the TM3-ICL 2-TM4 domain of MOR (6DDF) (left panel; blow-up of the yellow-colored cylinders) and its sequence alignment with Gal1R (right panel). Yellow arrows indicate interactions on structure, and correspond to those residues in the alignment.*

The first reported MOR crystal structure (4DKL) (Manglik *et al.*, 2012) was used as a template for the TM 5/6 interface. The interface of the homodimer is extensive and highly packed, which involves almost all the residues facing the membrane. However, the most significant differences between MOR and Gal1R on this interface are rather in the extracellular and intracellular areas. In the extracellular part (**Figure 2b**), Gal1R shows aromatic residues Trp at 6.57 and Phe at 6.60, which correspond to the

respective hydrophobic Ile and Leu in MOR. We hypothesize that the stronger aromatic-hydrophobic than hydrophobic-hydrophobic interactions at this extracellular locus might explain the experimentally observed more favorable TM 5/6 interface of MOR-Gal1R. In the intracellular part (**Figure 2c**), Arg6.31 and Arg6.35 of MOR make this part of receptor more positive than Lys6.31 and Gln6.35 of Gal1R in TM 6. Thus, there is a repulsion between Lys5.66 in TM 5 of MOR and the interacting MOR protomer in the MOR-MOR heterodimer that is less pronounced with Gal1R in the MOR-$Gal_1$R heteromer. This slight repulsion at this intracellular locus might also contribute to the observed more favorable TM 5/6 interface of MOR-$Gal_1$R.

The TM 4/5 dimeric interface observed in the oligomeric structure of the $\beta_1$-adrenergic receptor (4GPO) (Huang *et al.*, 2013) mainly occurs via ICL 2 (**Figure 2d**). The characteristic signature of the two-turn α-helix conformation of ICL2 is the Arg (or polar in other GPCRs) residue interacting with the negative charge of the (E/D)RY motif in TM3. This structure shows the presence of the KDF residues at the face of the ICL 2 helix pointing toward ICL2 of the interacting protomer, which correspond to RSL in $Gal_1$R (highlighted with yellow rectangles in the sequence alignment, **Figure 2d**). The constructed molecular models of the TM 4/5 interface reveal: favorable ionic Lys-Asp and Asp-Lys interactions and an aromatic-aromatic Phe-Phe interaction in the MOR-MOR homodimer; charged Arg-Ser and Ser-Arg hydrogen bonds and a hydrophobic-hydrophobic Leu-Leu interaction in the Gal1R-Gal1R homodimer; and a charged Lys-Ser hydrogen bond, an ionic Asp-Arg interaction, and an aromatic-hydrophobic Phe-Leu interaction in the MOR-$Gal_1$R heterodimer. These interactions show the feasibility of the proposed TM 4/5 interface for the MOR-MOR and Gal1R-Gal1R homodimers.

**Promiscuous G-protein coupling of Gal1R in the MOR-Gal1R heteromer**

Fluorescence complementation and bioluminescence techniques were used to delve further into the signaling properties of the MOR-Gal1R heterotetramer. With BRET (see METHODS), fusing RLuc to MOR or Gal1R and mVenus variant of YFP to the α subunit of a G-protein, we can analyze the effect of agonists in their ability to change the basal luminescence values, as an indirect measure of ligand-induced G-protein activation. MOR-RLuc or Gal1R-RLuc and Gi-YFP, Gq-YFP or Gs-YFP constructs were transiently co-transfected to HEK-293T cells, and concentration-response curves of MOR agonists methadone and fentanyl and Gal1R ligands M617 and M40 were analyzed for $EC_{50}$ and $E_{max}$ values (**Figure 3**). As expected from previous studies indicating a selective functional coupling of MOR to Gi/o proteins (Williams *et al.*, 2013; Che and Roth, 2021), both methadone and fentanyl promoted Gi, but not Gq/11 (Gq) or Gs, activation (**Figure 3a-c**) with no significant differences between their $EC_{50}$ values (**Figure 3d**). Also as expected, the Gal1R agonists M617 and M40 (Lang *et al.*, 2015) promoted activation of Gi and no activation of Gs (**Figure 3e,g,h**). Also less expected was that both agonists promoted Gq protein activation (**Figure 3f**). Until now it was generally assumed that Gal1R signaling was always regulated in a pertussis toxin-sensitive manner, mediated via Gi/o proteins, while Gal2R was predominantly coupling to Gq proteins (reviewed in ref. (Lang *et al.*, 2015)). The direction of the concentration-response curves of Gal1R ligands was opposite to that of the MOR ligands. In BRET experiments it is usually expected that ligands induce an increase in BRET values, because of a ligand-induced approximation of the donor and acceptor chromophores (Galés *et al.*, 2006). However, RET between two

chromophores also depends on their relative orientation (orientation factor or κ2) (Müller *et al.*, 2013), which could drive the qualitatively different ligand-induced RET response between the full or complemented RLuc fused to Gal1R and YFP fused to the corresponding Gα.

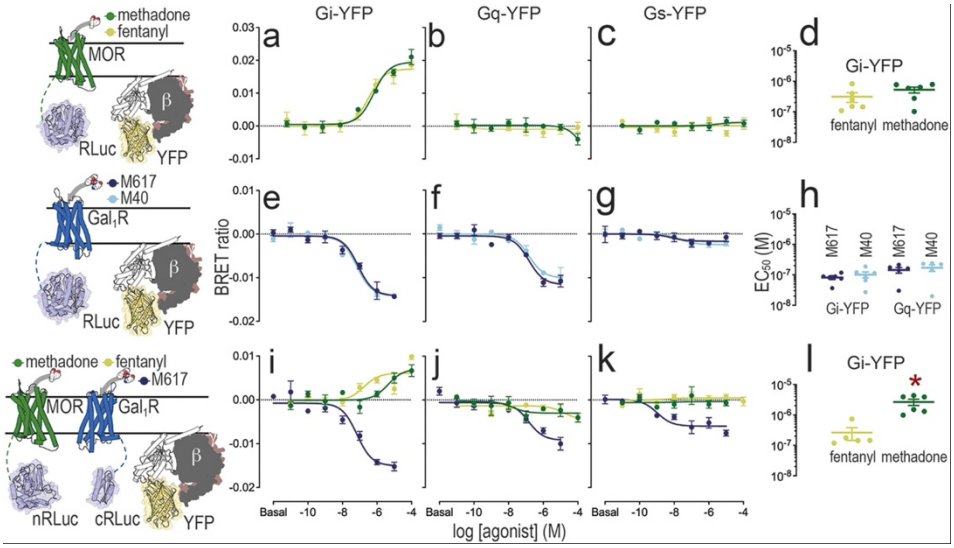


***Figure 3. G-protein coupling of MOR, Gal1R and the MOR-Gal1R heteromer in BRET and CODA-RET experiments. (a-c)*** *Representative concentration-response curves of methadone (dark green) and fentanyl (light green) of BRET experiments from HEK-293T cells co-transfected with MOR-RLuc and the α subunit of Gi (**a**), Gq (**b**) or Gs (**c**) fused to YFP. **e-g**. Representative concentration-response curves of M617 (dark blue) and M40 (light blue) of BRET experiments from HEK-293T cells co-transfected with Gal1R-RLuc and the α subunit of Gi (**e**), Gq (**f**) or Gs (**g**) fused to YFP. **i-k**. Representative concentration-response curves of methadone (dark green), fentanyl (light green) and M617 (dark blue) of CODA-RET experiments from HEK-293T cells co-transfected with MOR-nRLuc, Gal1R-cRLuc and the α subunit of Gi (**i**), Gq (**j**) or Gs (**k**) fused to YFP. d and h. $EC_{50}$ values of the BRET experiments with MOR-RLuc (**d**) or Gal1R-RLuc (**h**) (in means ± S.E.M.; n = 6 in all experiments, with triplicates). **l**. $EC_{50}$ values of the CODA-RET experiments with MOR-nRLuc and Gal1R-cRLuc (n = 5–6, with triplicates). The $EC_{50}$ values of fentanyl and methadone were significantly different in the CODA-RET (*: $p < 0.01$; two-tailed paired t test), but not in the BRET experiments.*

Next, both heteromerization and G-protein coupling was explored simultaneously with CODA-RET (see METHODS). MOR fused to nRLuc (MOR-nRLuc) and Gal1R fused to cRLuc (Gal1R-cRLuc) were co-transfected with Gi-YFP, Gq-YFP or Gs-YFP constructs (**Figure 3i-l**).

Again, the MOR agonists methadone and fentanyl only promoted activation of Gi (**Figure 3i-k**). However, in the MOR-Gal1R heteromer, the $EC_{50}$ values for methadone were about 10 times higher than for fentanyl (**Figure 3l**), which agrees with previous results demonstrating a specific decrease in the potency of methadone in the MOR-Gal1R heteromer (Cai *et al.*, 2019). Remarkably, in the MOR-Gal1R heteromer, M617 promoted not only Gi and Gq, but also significant Gs activation (with $EC_{50}$ values of 59.0 ± 20.1 nM for Gi, 154.1 ± 25.9 nM for Gq, and 58.7 ± 29.1 nM for Gs) (**Figure 3i-k**). Consistent with the results from the BRET assay, the direction of the M617 concentration-response curve was opposite to that of methadone and fentanyl. In summary, the results from the CODA-RET assay indicate Gal1R is capable of coupling to Gi, Gq and Gs upon heteromerization with MOR.

**Gal1R will preferentially couple Gs in MOR-Gal1R expressing cells**

The group at UB then investigated the preferred endogenous G-protein subtypes coupling to Gal1R and MOR in HEK-293T cells transfected with either receptor alone or together. They assessed this by analyzing the effects of agonists on basal and forskolin-induced cAMP formation (see METHODS) (**Figure 4a-e**). In cells transfected with MOR alone, the endogenous agonist endomorphin-1 (0.5 $\mu$M) was unable to modify cAMP levels relative to baseline (**Figure 4b**, no Gs-coupled) and significantly decreased forskolin-induced cAMP (**Figure 4b**, Gi-coupled). Similarly, in cells expressing Gal1R alone, galanin, M617 or M40 (each at 0.5 $\mu$M) did not modify the basal levels of cAMP (**Figure 4a**, no Gs-coupled) and significantly decreased cAMP formation induced by forskolin (**Figure 4a**, Gi-coupled). Thus, both MOR and Gal1R, when expressed by themselves, signal via their cognate Gi protein. Importantly, a complete signaling switch of Gal1R was observed in cells co-transfected with both

Gal1R and MOR. In this case, Gal1R agonists not only failed to decrease forskolin-induced cAMP (**Figure 4c**, left panel, no Gi-coupled), but they promoted a significant increase of cAMP formation relative to basal levels (**Figure 4c**, left panel, Gs-coupled).

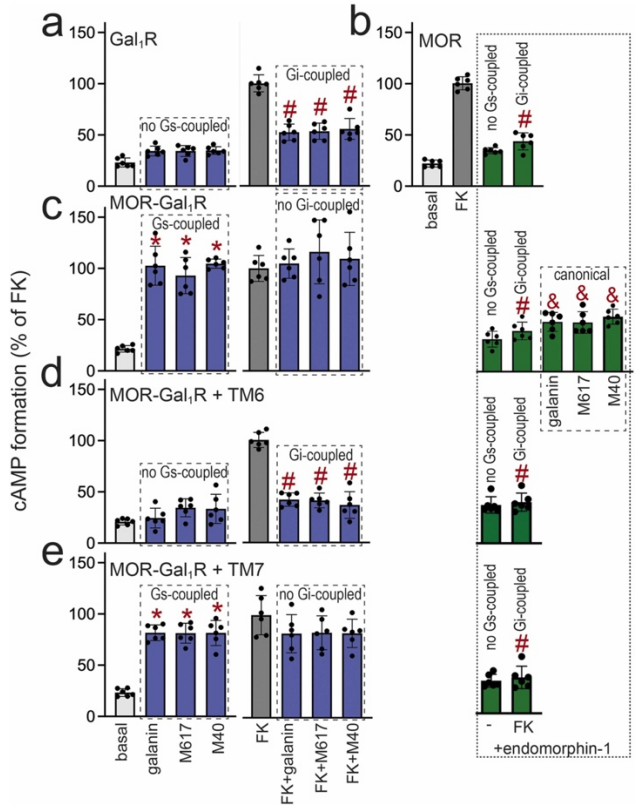


*Figure 4. Preferential Gs protein coupling of Gal1R when co-expressed with MOR in cAMP formation experiments. Formation of cAMP in HEK-293T cells transfected with Gal1R-YFP (**a**) MOR-RLuc (**b**) or both (**c-e**) upon exposure of forskolin (FK; 0.5 µM), galanin ligands (galanin, M617 or M40; all at 0.5 µM; blue bars within dashed frames) and endomorphin-1 (0.5 µM; green bars within dotted frame) alone or combined, in the absence (**a-c**) and presence (**d,e**) of the indicated TM peptides (TM6 or TM7; 4 µM) from MOR. "Gs-coupled" or "no-Gs-coupled" indicates the ability to increase or not cAMP formation when administered alone; "Gi-coupled" or "no-Gi-coupled" indicates the ability to decrease or not FK-induced cAMP formation; "canonical" indicates the ability of endomorphin-1 to counteract galanin-, M617- or M40-induced cAMP formation. Values are means ± S.D. (n = 6 with triplicates in all experiments) of the percentage of FK-induced cAMP formation and analyzed statistically with one-way ANOVA, followed by Tukey's multiple comparison test (*: p < 0.001, compared with basal; #: p < 0.001, compared with FK; &: p < 0.001, compared with galanin, M617 or M40 when administered alone).*

These results strongly suggested that heteromerization with MOR switches the preferential G-protein coupling of the Gal1R from Gi to Gs. By contrast, MOR kept its preferential coupling to Gi proteins in this configuration (**Figure 4c**, right panel, no Gs-coupled and Gi-coupled). These data suggest that the MOR-Gal1R heteromer constitutes an additional example of a Gs-Gi-coupled heterotetramer, with MOR and Gal1R homodimers coupled to Gi and Gs, respectively, and providing the frame that sustains a canonical Gs-Gi antagonist interaction at the AC level. In agreement, in cells co-transfected with both receptors, MOR agonists inhibited the cAMP-promoting effect of Gal1R agonists upon simultaneous exposure, revealing the canonical Gs-Gi antagonist interaction (**Figure 4c**, right panel, canonical). We next showed that the preferential Gs coupling of the Gal1R is, in fact, a property of the MOR-Gal1R heteromer. In the presence of the TM6 peptide of MOR, which disrupts the heteromeric interface, Gal1R agonists switched from inducing cAMP production (Gs-coupled) back to inhibiting forskolin-induced cAMP formation (Gi-coupled) (**Figure 4e**, left panel). In contrast, incubation with the TM7 peptide of MOR, which does not disrupt heteromer formation, had no such effect. The MOR agonist endomorphin-1 remained Gi-coupled in the presence of these peptides (**Figure 4d,e**, right panels).

**The G-protein subtype coupling to Gal1R depends on its homomeric interface**

To elucidate the molecular mechanism underlying the preferential Gs coupling of Gal1R in the MOR-Gal1R heteromer, we constructed computational models of Gal1R-Gal1R homodimers, built via the TM 4/5 and TM 5/6 interfaces, bound to Gi, Gs, and Gq (see METHODS) (**Figure 5**). Sequence alignment of C-terminal residues of the sixteen Gα subunits revealed a specific sequence of 13 extra Gs residues that is absent in the

other G-protein subtypes (**Figure 5a**). These extra residues are localized in the hgh4 loop, between HG and H4 helices, in the α-helical domain of the G-protein. Noticeably, in the model, the additional length of hgh4 of Gs clashes with the G-protein unbound Gal1R protomer in the TM 5/6 interface (**Figure 5b**, upper panel) but it is tolerated in the TM 4/5 interface (**Figure 5b**, lower panel). The shorter hgh4 loop of Gi (**Figure 5c**), Gq (**Figure 5d**) or Go (not shown) permits their binding to the Gal1R-Gal1R homodimer in the TM 5/6 interface. To experimentally validate this hypothesis, the group at NIDA/NIH created a mutant Gs in which these extra 13 residues were removed and a mutant Gi in which these residues were added in the corresponding hgh4 locus (see Methods in the original publication). Both mutants were fused to YFP and used in BRET experiments in cells co-transfected with Gal1R-RLuc, in the absence of MOR, and either the mutant Gs-YFP or the mutant Gi-YFP or the corresponding wild-type (WT) constructs (**Figure 5e**). As predicted, the Gal1R agonist M617 activated the mutant Gs (with short hgh4), since it could bind to the TM 5/6 interface (due to the absence of MOR) of the Gal1R-Gal1R homodimer, while M617 promoted a much weaker activation of mutant Gi as compared to WT Gi (with long and short hgh4, respectively), since it could not properly bind to the TM 5/6 interface of the Gal1R-Gal1R homodimer. These computational and experimental results indicate that the ability of Gs to couple to the Gal1R-Gal1R homodimer is determined by the change in its homomeric interface induced by heteromerization with MOR.

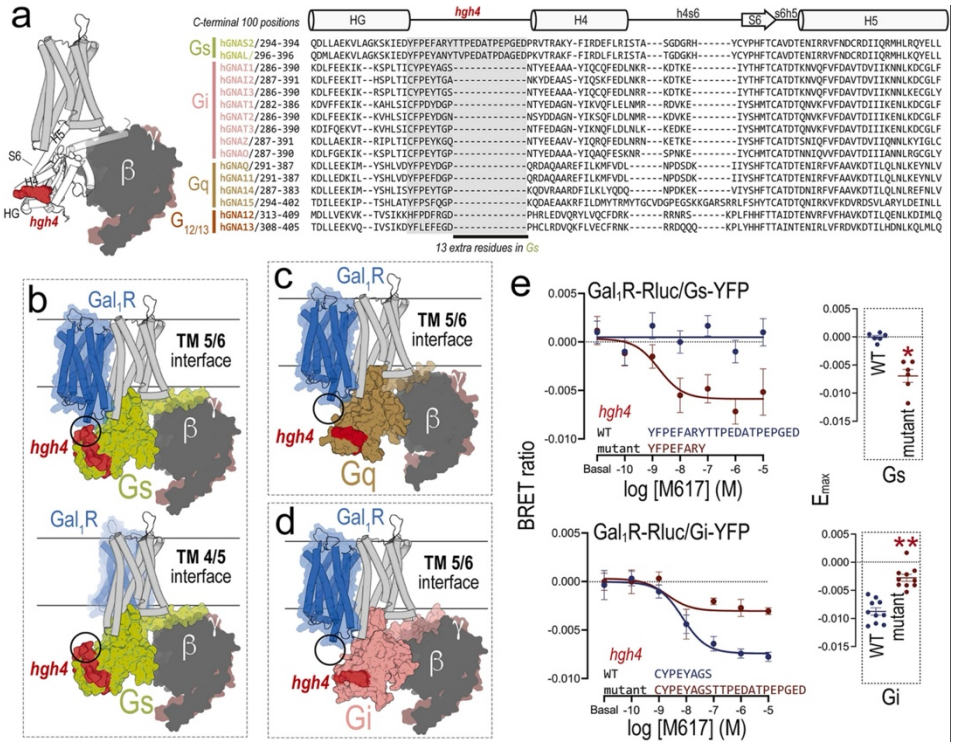


*Figure 5. Dimeric interface-dependent hindering role of the hgh4 loop of the Gαs subunit in its ability to couple to Gal1R.* ***(a)*** *Sequence alignment of the C-terminal 100 amino acids of the sixteen Gα subunits, as described in GproteinDb (Kooistra et al., 2021; Flock et al., 2015). The 13 extra residues of the hgh4 loop (in red), between HG and H4 helices of the Gαs subunits (see scheme on the left panel), that are absent in the other G-protein subtypes, are highlighted in grey. (**b-d**). Computational models of the Gal1R-Gal1R homodimer, constructed using the TM 5/6 interface (**b**, upper panel; **c**; **d**) or the TM 4/5 (**b**, lower panel) interface, in complex with Gs (**b**), Gi (**c**), and Gq (**d**). The encircled area shows the clash of the 13 extra residues of Gs with the G-protein unbound protomer in the TM 5/6 interface.* ***(e)*** *Representative concentration-response curves of the M617 agonist of BRET experiments from HEK-293T cells co-transfected with Gal1R-RLuc and WT Gs fused to YFP (blue line; left panel) or a mutant $G\alpha_s$ (with the extra 13 residues being removed) fused to YFP (red curve; left panel); or cells co-transfected with Gal1R-RLuc and WT Gi fused to YFP (blue curve; middle panel) or a mutant $G\alpha_i$ (with the extra 13 residues being added) fused to YFP (red curve; middle panel). In the right panel (**e**), comparison of $E_{max}$ values of the BRET experiments between WT and mutant α-subunits (in means ± S.E.M.; n = 6 in all experiments, with triplicates). The $E_{max}$ values between WT and mutant α-subunits were significantly different (*: $p < 0.05$, **: $p < 0.01$; two-tailed paired t test).*

### 6.1.3 Discussion

The present study reports converging evidence, using different methodologies, for a predominant homodimeric structure of both MOR and Gal1R, and for their preference to form functional heterotetramers coupled to Gs and Gi proteins that antagonistically interact at the level of the effector AC. The results therefore support the previously hypothesized view of the GPCR heterotetramer composed of two different GPCR homodimers respectively coupled to Gs and Gi proteins and AC as a common functional macromolecular complex (Ferré, 2015), more recently conceptualized as a G-protein-coupled receptor-effector macromolecular membrane assembly (GEMMA) (Ferré *et al.*, 2022) (see INTRODUCTION).

TIRF microscopy with TMPs confirmed the MOR-Gal1R quaternary structure (presented in CHAPTER II). In the previous chapter, the rearrangement in the homodimeric interfaces had a significant impact in the efficacy of (S)-methadone, unraveling a potential mechanism for the decreased addictive liability of methadone. In this case study, the heteromerization-induced change in the homomeric interface had a significant functional consequence: a switch in the G-protein coupling of Gal1R, from Gi to Gs, without modifying the G-protein preference of the MOR.

Previous studies with other GPCRs reported changes in their functional properties when heteromerizing. For instance, the switch is observed in G-protein coupling of serotonin 5-$HT_{2A}$ receptor from Gq to Gi proteins upon heteromerization with the cannabinoid $CB_1$ receptor (Viñals *et al.*, 2015) (the molecular mechanism will be presented in Case Study #4) or the disappearance of the pronounced constitutive activity of the adenosine

$A_{2A}$ receptor when forming heteromers with the adenosine $A_1$ receptor or the dopamine $D_2$ receptor, but not with the cannabinoid $CB_1$ receptor (Köfalvi *et al.*, 2020). However, to our knowledge, this is the first study to unveil the molecular mechanism behind a heteromerization-dependent change in GPCR function, which we demonstrate is a facilitation of Gs coupling upon a switch in the Gal1R homomeric interface.

## 6.1.4 Supplementary Material

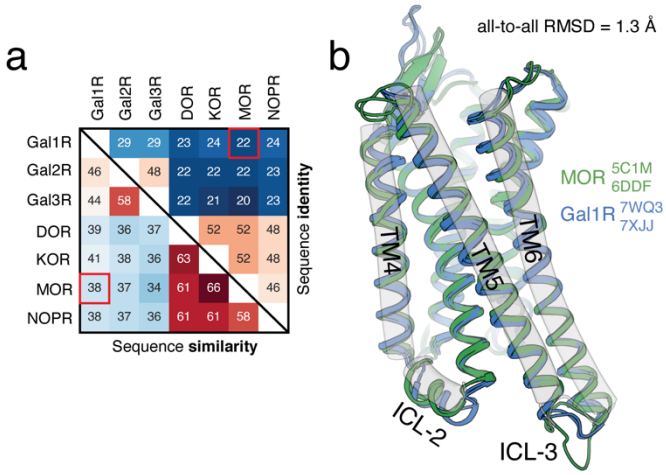


*Supplementary Figure 1. Sequence and structure comparison of MOR and Gal1R. (a) Sequence similarity and identity matrix, with all the members of the galanin and opioid receptor families. (b) Structure superposition of two structures per receptor family (PDB codes shown in figure), highlighting the areas used for the Molecular basis for the interface change section, indicating how similar these two receptors are structurally.*

## 6.2 Case Study #4. The C-tail of functional cannabinoid receptor 1 ($CB_1R$) facilitates the G-protein class-switch of serotonin 5-$HT_{2A}$ receptor (5-$HT_{2A}R$) in the $CB_1R$-5-$HT_{2A}R$ heteromer.

It will be published as **co-author** in

Botta, J.[1], Chunilal, V.[1], Casajuana-Martin, N.[1], Bondar, A., D'augello, I., Llinas del Torrent, C., Howell, L. A., Contino, M-A., Guzmán, M., Lazar, J., Pardo, L., McCormick, P. J. **The C-tail of functional cannabinoid receptor 1 ($CB_1R$) facilitates the G-protein class-switch of serotonin 5-$HT_{2A}$ receptor (5-$HT_{2A}R$) in the $CB_1R$-5-$HT_{2A}R$ heteromer**. *Science Signaling,* submitted.

[1]These authors have contributed equally

### 6.2.1 Introduction

$CB_1R$-5-$HT_{2A}R$ complexes are among the few oligomers wherein their expression in native tissues and physiological relevance has been demonstrated, meeting all the recently proposed criteria to define genuine GPCR heteromers (Gomes *et al.*, 2016): (i) co-localization and physical interaction as determined by in vitro proximity-based biophysical techniques and in situ proximity ligation assay to detect protein–protein interactions in native tissues, (ii) specific biochemical signatures of heteromers distinct from those of the protomers, (iii) mice expressing heteromerization-deficient receptors, and (iv) selective disruption of the complexes by TMPs (Guinart *et al.*, 2020; Gallo *et al.*, 2022; Botta *et al.*, 2019; Viñals *et al.*, 2015).

As it was mentioned in the discussion of Case Study #3, co-expression of both receptors led 5-$HT_{2A}R$ to signal through Gi/o instead of Gq/11,

whereas cells expressing only 5-$HT_{2A}$R retained their canonical Gq/11 coupling signature (Viñals *et al.*, 2015). Here, we aim to study the mechanism by which heteromerization facilitates 5-$HT_{2A}$R to bind the non-canonical Gi/o protein. This is relevant because the $CB_1$R-5-$HT_{2A}$R heteromer is responsible for the cognitive side effects of $\Delta^9$-tetrahydrocannabinol (THC) (Viñals *et al.*, 2015), which is the principal psychoactive constituent of the Cannabis sativa plant (more commonly known as marijuana). The $CB_1$R–5-$HT_{2A}$R heteromer is, therefore, the consequence of an explicit molecular mechanism of THC to dissociate beneficial antinociceptive response and detrimental amnesic effects, hence defining it as a novel therapeutic target. A heteromer-disrupting ligand would allow the use of Cannabis to fight pain while avoiding side effects (Gallo *et al.*, 2022). Based on their promising implications as alternative pain treatments and in the safe use of cannabinoid-based therapies, we provide an in-depth mechanistic perspective on how they function.

## 6.2.2 Results

**Mutants that impede activation of the receptor to study its functionality in vitro**

To uncover the mechanisms driving the function of the $CB_1$R-5-$HT_{2A}$R heteromer, we first rationally designed a series of 5-$HT_{2A}$R and $CB_1$R mutants that were either unable to undergo agonist-induced receptor activation or to efficiently couple to G-proteins (**Figure 6a,b**). Most class A GPCRs contain the PIF motif that transmits the signal from the orthosteric ligand binding site to the G-protein binding site (see INTRODUCTION) (Zhou *et al.*, 2019; Weis and Kobilka, 2018). In particular, the interaction of agonists with TM5 triggers an inward

movement of TM5 at P5.50, a rotation of TM3 at I3.40, and an outward movement of TM6 at $F^{6.44}$ (Rasmussen *et al.*, 2011). Accordingly, we designed Ala substitution 5-$HT_{2A}$R and $CB_1$R mutants, aiming to impede receptor activation via mutation of the hydrophobic amino acid of the PIF motif (5-$HT_{2A}$R $I163A^{3.40}$ and $CB_1$R $V204A^{3.40}$). Upon receptor activation, the cytoplasmic end of TM6 moves outward opening an intracellular cavity to accommodate the C-terminal α5 helix of the Gα subunit (Rasmussen *et al.*, 2011; Weis and Kobilka, 2018). The Gα protein family possesses a highly conserved Leu residue at position i-2, relative to the final amino acid, that forms hydrophobic-hydrophobic interactions with highly conserved hydrophobic amino acids at positions 6.33 and 6.37 of the receptor. Thus, to impede the efficient coupling of the G-protein to either 5 $HT_{2A}$R or $CB_1$R, we engineered the $L325A^{6.37}$ mutant in 5-$HT_{2A}$R (the presence of $A321^{6.33}$ in the sequence impedes Ala mutation at this position) and the $L341A^{6.33}$ and $L345A^{6.37}$ mutants in $CB_1$R. Moreover, class A GPCRs contain a conserved (E/D)$R^{3.50}YX_5P\Phi X\Omega$ motif, in which Pro starts the conserved two-turn α-helix conformation of ICL 2, the aromatic Ω interacts with the negative charge of the (E/D)RY motif, and the hydrophobic Φ forms hydrophobic-hydrophobic interactions with hydrophobic residues at the β1 and β3 strands and α5 helix of Gα. Accordingly, we also performed the $I181A^{ICL2}$ and $L22_{2A}{}^{ICL2}$ mutants of 5 $HT_{2A}$R and $CB_1$R, respectively.

The group at the Queen Mary University of London tested 5-$HT_{2A}$R mutants for their ability to mobilize intracellular calcium $[Ca^{2+}]_i$, canonical secondary messenger downstream of the Gq/11-coupled receptor (Day *et al.*, 2002), and $CB_1$R mutants for their ability to reduce forskolin (FK)-induced cAMP production as a Gi-coupled receptor (Howlett and Fleming, 1984). 5-$HT_{2A}$R $I163A^{3.40}$ failed to mobilize $[Ca^{2+}]_i$ after 2,5-Dimethoxy-4-

iodoamphetamine (DOI) administration in transiently transfected HEK 293 cells (**Figure 6c**), confirming the importance of the hydrophobic amino acid of the PIF motif in aminergic receptors (Sansuk *et al.*, 2011). Interestingly, the analogous V204A$^{3.40}$ substitution in $CB_1R$ had no impact on cAMP signaling of the WIN 55212-2 (WIN) agonist (**Figure 6d**). GPCRs activated by signaling molecules derived from lipid species, such as cannabinoid, sphingosine-1-phosphate ($S_1P$), and lysophosphatidic acid (LPA) receptors, lack Pro5.50 of the PIF motif and the initial agonist-induced receptor activation is via a conformational toggle or trigger switch of the side chain at position 3.36 (Pellissier *et al.*, 2009; S. Liu *et al.*, 2022; Maeda *et al.*, 2021; Krishna Kumar *et al.*, 2019). 5-$HT_{2A}$R I181A$^{ICL2}$ nearly abolishing DOI-induced $[Ca^{2+}]_i$ release (~25% $E_{max}$, WT vs. I181A$^{ICL2}$) and decreasing ~100 fold DOI's $EC_{50}$ ($pEC_{50}$ ~9.0 and 7.0 for WT vs. I181A$^{ICL2}$, respectively) (**Figure 6c**). This agrees with previous results for $\alpha_{1B}$ adrenergic receptor, thyrotropin-releasing hormone receptor, histamine $H_1$ receptor and 5-$HT_{2A}$R (Garća *et al.*, 2017; Moreno *et al.*, 2016; Carrillo *et al.*, 2004). By contrast, $CB_1R$ L222A$^{ICL2}$ (homologous to 5-$HT_{2A}$R I181A$^{ICL2}$) had no effect on $CB_1R$ function (**Figure 6d**), suggesting that interactions between ICL2 and the hydrophobic pocket are less important for Gi coupling of this receptor (Krishna Kumar *et al.*, 2019). Alternatively, L341A$^{6.33}$ and L345A$^{6.37}$ mutants significantly impact $CB_1R$ function, with the Ala substitution at position 341$^{6.33}$ sufficient to banish WIN-induced receptor signaling (**Figure 6d**). In agreement, using a different non-classical $CB_1R$ agonist (CP55940), it has been shown that $CB_1R$ L341$^{6.33}$ mutants retain ligand binding but prevent Gi/o coupling. Moreover, it was also assessed whether double substitutions could fully block $CB_1R$ by designing double mutants. As shown in **Suppl. Figure 1**, none of the constructs were more effective than the single mutants alone. For 5-

$HT_{2A}R$, the $L325A^{6.37}$ mutant also impaired 5-$HT_{2A}R$ signaling (**Figure 6c**), with a rightward shift in DOI-induced potency and nearly reaching half $E_{max}$ in comparison to the WT receptor.

The mutational data indicate different structural determinants between 5-$HT_{2A}$ and $CB_1$ receptors driving receptor activation and/or G-protein coupling. Based on these findings, the 5-$HT_{2A}R$ single mutants $I163A^{3.40}$ and $I181A^{ICL2}$, which gave complete or 100-fold $Ca^{2+}$ signal inhibition, respectively, and the $CB_1R$ single mutants $L341A^{6.33}$ and $L345A^{6.37}$, which gave complete or partial cAMP release inhibition, respectively, were selected for further detailed characterization. First, the homogeneous distribution of all mutants across the cell-surface was validated (**Suppl. Figure 2a**). In addition, a similar behavior was observed when 5-$HT_{2A}R$ was stimulated with the endogenous ligand serotonin (5-HT), corroborating the lack of ligand/mutant bias (**Suppl. Figure 2b**). Next, the group at the Queen Mary University of London studied the effects of these mutations in 5-$HT_{2A}R$-$CB_1R$ dimerization, using the NanoBiT technology (see CASE STUDY #1). Nanoluciferase-mediated luminescence was observed in HEK-293 cells co-expressing 5-$HT_{2A}R$ fused to a long portion (LgBiT) and $CB_1R$ fused to a short portion (SmBiT) of nanoluciferase, which was decreased in the presence of the previously reported synthetic TM5 TMP (Viñals *et al.*, 2015) and was unaltered by TM7 (negative control) (**Figure 6e**). When we introduced the $I163A^{3.40}$ and $I181A^{ICL2}$ substitutions in 5-$HT_{2A}R$-LgBiT and the $L341A^{6.33}$ and $L345A^{6.37}$ in $CB_1R$-SmBiT, none of the mutations affected receptor oligomerisation, with the luminescent readouts significantly higher compared with when each construct was expressed alone and with those of the WT forms (**Figure 6f**).

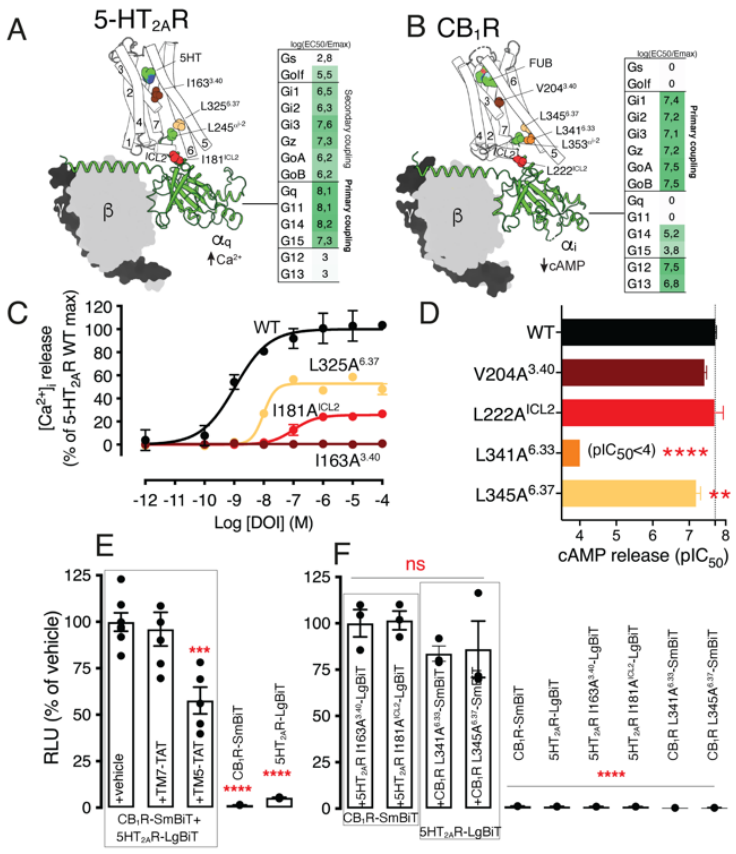


*Figure 6. Molecular design and functional validation of 5-HT2A and CB1 receptor mutants*. *(**a,b**) Cryo-EM structures of active 5-HT$_{2A}$R in complex with Gq/11 (PDB id 7RAN) (**a**) and active CB$_1$R in complex with Gi (6N4B). The G-protein coupling pattern for each receptor is depicted as according to (Hauser et al., 2017). (**b**). 5HT and MDMB-Fubinaca (FUB) agonists (green surfaces), I163$^{3.40}$ in 5-HT$_{2A}$R and V204$^{3.40}$ in CB$_1$R of the PIF motif (brown), L341$^{6.33}$ in CB$_1$R (orange) and L325$^{6.37}$ in 5-HT$_{2A}$R and L345$^{6.37}$ in CB$_1$R (yellow) that interact with L245 in $\alpha_q$ and L353 in $\alpha_i$ at position i-2 relative to the final amino acid of Gα (green), and I181$^{ICL2}$ in 5 HT$_{2A}$R and L22$_{2A}^{ICL2}$ in CB$_1$R (red) that interact with the β1 and β3 strands and α5 helix of Gα are shown. **(c)** Representative dose-response [Ca$^{2+}$]$_i$ release curves for the 5-HT$_{2A}$R mutants. **(d)** Mean pIC50 ± SEM (n≥3) forskolin-induced (7.5μM) cAMP release inhibition for the CB$_1$R mutants upon WIN 55212-2 stimulation. Statistical significance was evaluated by one-way analysis of variance (ANOVA) followed by Bonferroni post hoc tests (**p ≤0.01, ****p ≤0.0001). **(e)** HEK 293 cells co-expressing 5-HT$_{2A}$R-LgBiT and CB$_1$R-SmBiT (or the individual constructs alone) were pre-treated with vehicle, TM7-TAT or TM5-TAT peptides (4 μM) prior to the addition of Furimazine and subsequent luminescence recording. Data are mean ± SEM (n≥3). Statistical significance was evaluated by one-way ANOVA followed by Bonferroni post hoc test, indicating significant differences over vehicle treated cells or for each receptor pair compared to its corresponding individual constructs (***p ≤ 0.0001, ****p ≤ 0.0001, ns; non-significant). **(f)** Dimerization of 5-HT$_{2A}$ and CB$_1$ receptor mutants. Treatments, sample size and analysis as in **(e)**.*

**Two-Photon Polarisation Microscopy reveals a G-protein class switch**

To examine the heteromer-driven non-canonical binding of heterotrimeric Gi/o proteins upon agonist binding to 5-$HT_{2A}$R, the group at the Queen Mary University of London employed the recently developed two-photon polarization microscopy (2PPM) technique to directly visualize receptor:G-protein interactions (Bondar and Lazar, 2017; Lazar *et al.*, 2011). 2PPM allows visualization of G-protein activation due to the accompanying changes in orientational freedom of fluorescent labels attached to the investigated Gα subunits. Fluorescent labels in non-activated Gα subunits (present in heterotrimeric complexes with Gβ and Gγ subunits) generally display higher values of linear dichroism (LD; differences between images acquired with two distinct linear polarizations of excitation light) than in activated, monomeric Gα subunits. Thus, HEK 293 cells were transfected with constructs encoding the Gi1 protein subunits (GAP43-eCFP-$G\alpha_{i1}$, Gβ1, Gγ2) and the receptors (5-$HT_{2A}$R and/or $CB_1$R-eYFP) (**Figure 7**). In the presence of only $CB_1$R-eYFP, the eCFP-tagged $G\alpha_{i1}$ subunit showed a $\log_2(r_{max})$ value that was significantly reduced ($p<0.001$) upon stimulation with WIN (10 μM) (**Figure 7b**), as expected from its canonical Gi/o coupling. Accordingly, DOI (100 nM) administration did not induce LD changes in cells expressing only $CB_1$R-eYFP ($p=0.79$), indicating ligand selectivity (**Figure 7c**). Similarly, in the presence of only 5-$HT_{2A}$R, the eCFP-tagged $G\alpha_{i1}$ subunit shows no statistical differences ($p=0.52$) in $\log_2(r_{max})$ before and after stimulation with DOI (**Figure 7a**), showing the lack of Gi/o coupling to 5-$HT_{2A}$R. However, in cells expressing both 5-$HT_{2A}$R and $CB_1$R-eYFP, DOI-stimulation led to a significant decrease ($p<0.001$) in $\log_2(r_{max})$ of the eCFP-tagged $G\alpha_{i1}$ subunit, consistent with 5-$HT_{2A}$R-mediated non-canonical Gi binding in $CB_1$R-5-$HT_{2A}$R heteromers

(**Figure 7d**). Finally, the designed 5-$HT_{2A}$R mutants were used to test whether receptor trans-activation or G-protein class switch occurs. In cells co-transfected with $CB_1$R-eYFP and the 5-$HT_{2A}$R I181A$^{ICL2}$ mutant, designed to avoid G-protein binding, the eCFP-tagged $G\alpha_{i1}$ subunit showed no statistical differences (p=0.79) in $\log_2(r_{max})$ between cells unstimulated and stimulated with DOI (100 nM) (**Figure 7e**). These results indicate that the $G\alpha_{i1}$ protein can bind stimulated 5-$HT_{2A}$R, but only in the presence of $CB_1$R and the efficiency of 5-$HT_{2A}$R-mediated binding of $G\alpha_{i1}$ appears lower than the efficiency of $G\alpha_{i1}$ binding to $CB_1$R.

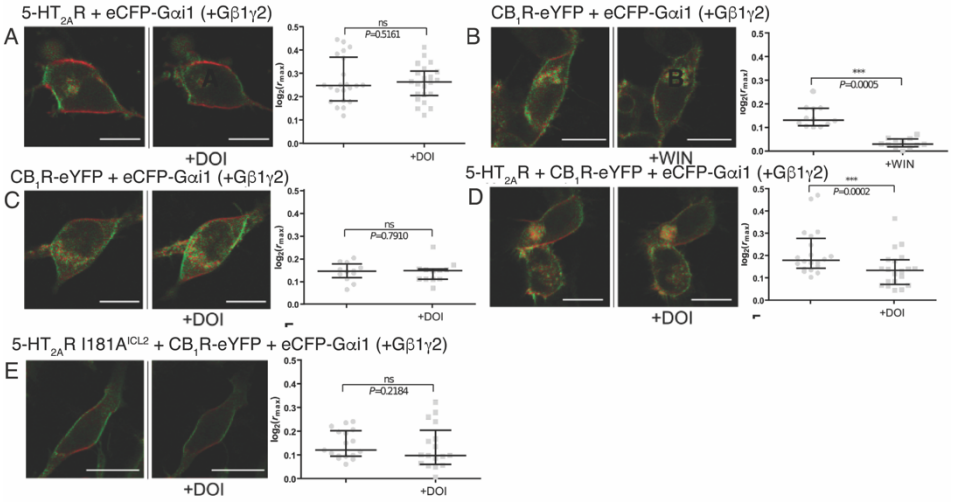


*Figure 7. Two photon polarization microscopy reveals a singular 5-$HT_{2A}$R-$CB_1$R heteromer-driven Gi coupling. HEK 293 cells were transfected with GAP43-eCFP-$G\alpha_{i1}$, Gβ1 and Gγ2 subunits, as well as with 5-$HT_{2A}$R (**a**), $CB_1$R-eYFP (**b** and **c**), 5-$HT_{2A}$R and $CB_1$R-eYFP (**d**) or 5-$HT_{2A}$R I181A$^{ICL2}$ and $CB_1$R-eYFP (**e**). Images show representative cells before and after treatment with DOI (100 nM) or WIN (10 μM) as indicated. Color bars indicate the range of dichroic ratios shown in the images. Scale bars are 10 μm. Graphs show linear dichroism (values of log2(rmax)) of individual cells (individual data points), along with the median and 25th and 75th percentiles. Statistical significance over treatments was evaluated by Wilcoxon signed rank test. (***p ≤ 0.001). ns: non-statistically significant.*

**Binding of Gi/o to 5-$HT_{2A}$R requires a functional interacting $CB_1$R protomer**

In previous studies, it was described that, in addition to a Gq/11 to Gi/o switch in 5-$HT_{2A}$R coupling, co-stimulation of the $CB_1$R-5-$HT_{2A}$R heteromer with both agonists does not produce an additive effect (known as negative cross-talk) (Viñals *et al.*, 2015; Guinart *et al.*, 2020; Gallo *et al.*, 2022). Thus, the group at the Queen Mary University of London next determined signaling after WT and mutant receptor activation by measuring decrease in FK-induced cAMP (**Figure 8**). In cells transiently co-expressing both $CB_1$R and 5-$HT_{2A}$R, DOI and WIN stimulation resulted in a reduction in FK-induced cAMP accumulation, confirming 5-$HT_{2A}$R-mediated Gi/o signaling (**Figure 8a**). As expected, simultaneous addition of DOI and WIN did not evoke an additive effect (negative cross-talk). It is important to note the specificity of DOI and WIN effects, as the decrease of FK-induced cAMP was blocked by their corresponding selective antagonist, MDL 100907 (MDL) and Rimonabant (RIM), respectively (**Figure 8a**). Next, we sought to address whether this pharmacological fingerprint of the $CB_1$R-5-$HT_{2A}$R heteromer depends on the presence of functional 5-$HT_{2A}$R (**Figure 8b,c**) and $CB_1$R (**Figure 8d,e**). As expected, inactivation of 5-$HT_{2A}$R by the I163A$^{3.40}$ (**Figure 8b**) or I181A$^{ICL2}$ (**Figure 8c**) mutants abolished DOI-induced cAMP inhibition; and stimulation with WIN did not significantly decrease FK-induced cAMP on the L341A$^{6.33}$ mutation of $CB_1$R (**Figure 6d**), whereas there is a small decrease, in comparison to the WT receptor, for the L345A$^{6.37}$ mutation (**Figure 6e**), supporting the inability of $CB_1$R to trans-activate 5-$HT_{2A}$R. Interestingly, DOI did not signal via Gi/o coupling when WT 5-$HT_{2A}$R was co-transfected with either inactive L341A$^{6.33}$ (**Figure 6d**) or L345A$^{6.37}$ (**Figure 6e**) mutants of $CB_1$R, stressing again that binding of Gi/o to 5$HT_{2A}$R requires a fully

functional interacting $CB_1R$ protomer and that this non-canonical signaling is not achieved through 5-$HT_{2A}R$ trans-activating $CB_1R$. Altogether, this evidence indicates that for the DOI-induced cAMP release inhibition in cells expressing $CB_1R$-5-$HT_{2A}R$ heteromers, two functional protomers are required. In addition, our results point against trans-activation in either direction, providing evidence of a Gi/o class switch underneath 5-$HT_{2A}R$ and raising the possibility of simultaneous recruitment of heterotrimeric Gi/o proteins to the hetero-receptor complexes after simultaneous activation.

**5-$HT_{2A}R$ and $CB_1R$ form homodimers in the $CB_1R$-5-$HT_{2A}R$ heteromer**

So far, it has been shown that the 5-$HT_{2A}R$ G-protein class switch only occurs when interacting with a fully functional $CB_1R$ (**Figure 7**), thus both 5-$HT_{2A}R$ and $CB_1R$ must be capable of adopting an active conformation able to bind G-proteins (**Figure 8**). These results gave rise to the question whether a higher oligomeric quaternary structure may take place, as simultaneous binding of two G-proteins to a GPCR heterodimer cannot occur due to steric clashes (Franco *et al.*, 2021). As mentioned, and presented in previous chapters, dimer of dimers have been identified at the plasma membrane of different cell types, including $A_{2A}R$-$D_2R$ (Navarro, Cordomí, Casadó-Anguera, *et al.*, 2018), 5-$HT_{2A}R$-mGlu2R (Moreno *et al.*, 2016), $A_1R$-$A_{2A}R$ (Navarro *et al.*, 2016), or MOR-Gal1R (Case Studies #2 and #3) heteromers. To determine the preferential number of protomers in the $CB_1R$-5-$HT_{2A}R$ heteromer, the group at the Queen Mary University of London sought to combine NanoLuc BiLC with BRET. Using their previously cloned and validated LgBiT and SmBiT NanoLuc complementary fragments at the N-terminus of both $CB_1R$ and 5-$HT_{2A}R$ (Botta *et al.*, 2019), they developed a NanoBRET variant. This

involved use of a red-shifted fluorophore for attachment onto the haloalkane dehalogenase linker (HaloTag®) (Machleidt *et al.*, 2015).

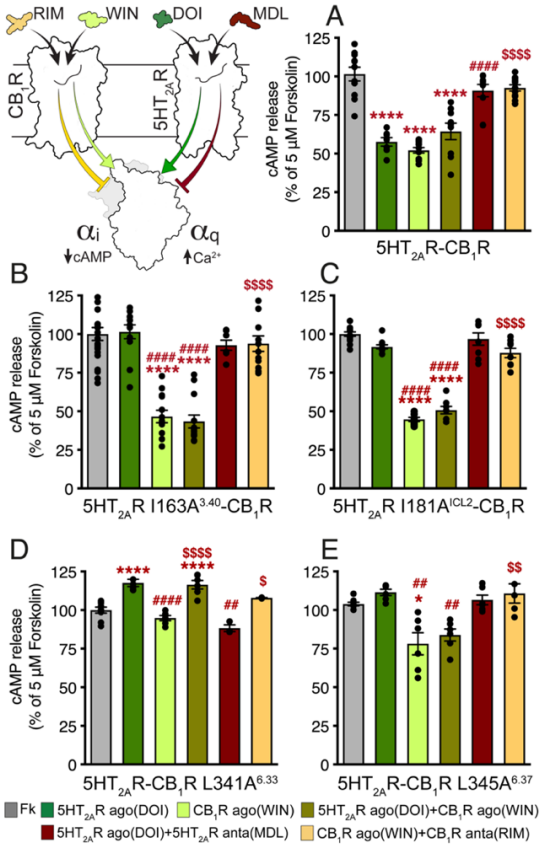


***Figure 8. Cross-talk in cAMP signalling requires both functional 5-HT$_{2A}$R and CB$_1$R protomers (a)*** *cAMP signalling in cells expressing WT CB$_1$R-5-HT$_{2A}$R heteromers.* ***(b,c)*** *Effect of the 5-HT$_{2A}$R mutants 5-HT$_{2A}$R I163A3.40 (**b**) and 5-HT$_{2A}$R I181A$^{ICL2}$ (**c**) in 5-HT$_{2A}$R-CB$_1$R heteromer-driven cAMP signalling. D,E Effect of the CB$_1$R mutants CB$_1$R L341A$^{6.33}$ (**d**) and CB$_1$R L345A$^{6.37}$ (**e**) in CB$_1$R-5-HT$_{2A}$R heteromer-driven cAMP signalling cross-talk. Data information: HEK 293 cells co-expressing different receptor combinations (see X axis in each panel) were pre-incubated for 20 min with vehicle, the 5-HT$_{2A}$R antagonist MDL (1 µM) or the CB$_1$R antagonist RIM (1 µM) prior to the stimulation with the 5-HT$_{2A}$R agonist DOI (100 nM), the CB$_1$R agonist WIN (100 nM) or both 5-HT$_{2A}$R and CB$_1$R agonist (DOI+WIN, 100 nM each). cAMP changes were monitored for 1-hour post-agonist addition using the pGloSensor™-22F. Values are mean ± SEM (n≥3) of percentage of activation normalised to forskolin (5 µM) maximal signal. Statistical significance was evaluated by one-way ANOVA followed by Bonferroni post hoc test showing significant effects over basal activation levels (*p ≤ 0.05, ****p ≤ 0.0001), over DOI (##p ≤ 0.01, ####p ≤ 0.0001) or over WIN ($p ≤ 0.05, $$p ≤ 0.01, $$$$p ≤ 0.0001).*

Thus, they used the LgBiT-$CB_1R$ and SmBiT-5-$HT_{2A}R$ interactinG-proteins as a donor (NanoBiLC BRET donor) and the acceptor was generated by cloning the HaloTag® enzyme to the N-terminal domain of both $CB_1$ (Halo-$CB_1R$) and 5-$HT_{2A}$ (Halo-5-$HT_{2A}R$) receptors (**Figure 9a**). Cells co-expressing the NanoBiLC BRET donor and Halo $CB_1R$ or Halo-5-$HT_{2A}R$ were incubated in the presence of the HaloTag®NanoBRET™ 618Ligand (590 and 618 nm excitation and emission, respectively) before performing the NanoBiLC BRET assays. As predicted, a robust and sustained increase in energy transfer was detected from the $CB_1R$-5-$HT_{2A}R$ heterodimer towards both $CB_1$ and 5-$HT_{2A}$ acceptor pairs (**Figure 9a**), indicating architectures composed of at least two protomers of the same receptor with one protomer of the other receptor (LgBiT-$CB_1R$:SmBiT-5-$HT_{2A}R$:Halo-$CB_1R$ or LgBiT-$CB_1R$:SmBiT-5-$HT_{2A}R$:Halo-5-$HT_{2A}R$). Importantly, the detected BRET was not due to random collision, as a saturating concentration (100 nM) of the acceptor HaloTag®NanoBRET™ 618 Ligand was always present in the imaging buffer (see Methods). Our results indicate that both $CB_1$ and 5-$HT_{2A}$ receptors form homodimers when forming $CB_1R$-5-$HT_{2A}R$ heteromers .

These results indicate that $CB_1R$-5-$HT_{2A}R$ heteromers are consistent with a tetrameric architecture composed of dimers of dimers in complex with two G-proteins. Knowledge of the stoichiometry is fundamental, but the knowledge of the molecular interfaces by which the protomers interact is key to understand the quaternary arrangement of the protomers in the heterotetramer. Previous studies have used TMPs to identify the TM interfaces involved in $CB_1R$-5-$HT_{2A}R$ heterodimerization (TM5/6) (Viñals *et al.*, 2015) and $CB_1R$ homodimerization (TM4) (Köfalvi *et al.*, 2020). **Figure 9b** shows a molecular model of the $CB_1R$-5-$HT_{2A}R$ heterotetramer constructed from these experimentally determined interfaces (TM5/6 for

heteromerization and TM4 for $CB_1R$ homodimerization) and predicting, but not experimentally determined, a symmetrical TM4 for $5\text{-}HT_{2A}R$ homodimerization. The existence of a $CB_1R\text{-}5\text{-}HT_{2A}R$ heterotetramer implies two internal interacting protomers of the heterodimer and two external protomers to which the G-proteins bind. The fact that binding of $G_{i/o}$ to $5\text{-}HT_{2A}R$ requires a functional interacting $CB_1R$ protomer capable of undergoing ligand activation and to bind $G_{i/o}$, is a property associated with this specific quaternary structure, which positions both G-proteins in proximity. Alteration of this quaternary structure blocks the crosstalk between G-proteins.

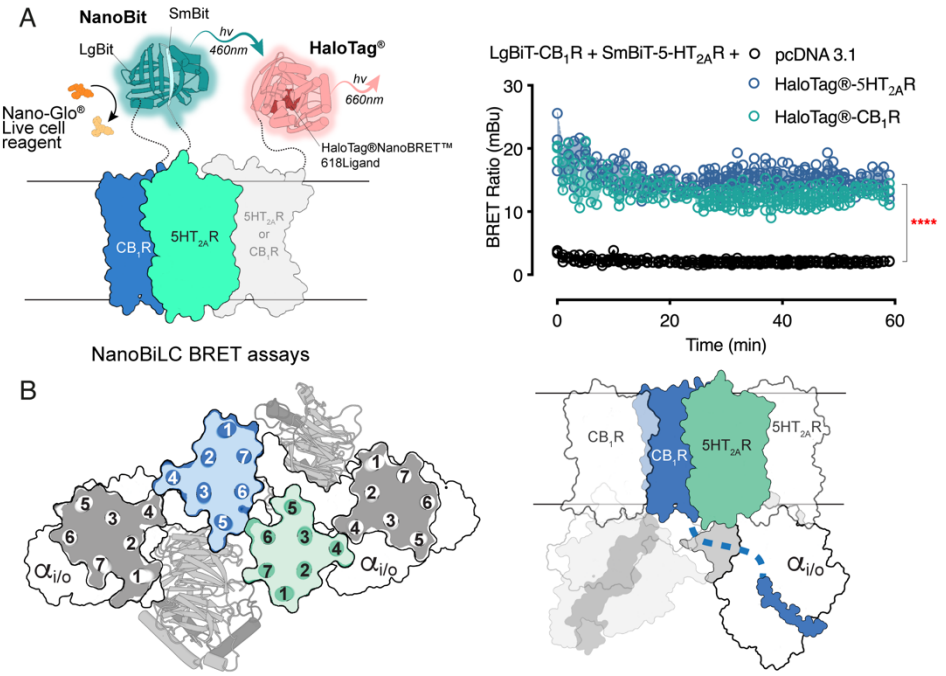


*Figure 9. Higher quaternary organization in $5\text{-}HT_{2A}\text{-}CB_1$ receptor heteromers. (a) NanoBiLC BRET assay to assess higher oligomeric structures (see illustration on left panel). Cells co-transfected with the SmBiT-5-$HT_{2A}$R:LgBiT-$CB_1$R NanoBiT® positive pair (BRET donor) together with HaloTag®-5-$HT_{2A}$R, HaloTag®-$CB_1$R or empty vector (pcDNA3.1) were labelled with the HaloTag®NanoBRET™618 Ligand (BRET acceptor). BRET signals were continuously recorded for 1 hour immediately after Furimazine addition (see Methods). Data are mean ± SEM (n≥3). One-way ANOVA with repeated measures followed by Bonferroni post hoc test indicates significant differences over BRET donor only expressing cells (****p ≤ 0.0001). (continues)*

*(b) The schemes illustrate extracellular and parallel to the membrane views of the computational model of the $CB_1R$-5-$HT_{2A}R$ heteromer built using the TM 5/6 interface for heteromerization and TM4 for 5-$HT_{2A}R$ and $CB_1R$ homodimerization. The proposed interaction between the last 23 amino acids of the internal $CB_1R$ protomer (in blue) and the $\alpha_{i/o}$ subunit of Gi/o bound to the external 5-$HT_{2A}R$ protomer is shown.*

**The G-protein switch involves the $CB_1R$ C-terminus**

The C-terminal domain of GPCRs contain important regulatory sites that enable interactions with intracellular signaling effectors and is relevant in the formation of GPCR oligomers (Navarro *et al.*, 2010). In particular, the C-terminus of $CB_1R$ (60 amino acids long from the end of Hx-8) contains a significant number of negatively charged Asp/Glu and phosphorylatable Ser and Thr amino acids that could cause the prevailing Gi/o-mediated signaling of 5-$HT_{2A}R$ in the $CB_1R$-5-$HT_{2A}R$ heteromer. To test this hypothesis, the group at the Queen Mary University of London engineered a $CB_1R$ mutant lacking the last 23 amino acids (IKSTVKIAKVTMSVSTDTSAEAL were removed, $CB_1R^{\Delta 23}$). Compared to WT $CB_1R$, $CB_1R^{\Delta 23}$ retained Gi/o-binding (10-fold potency reduction in WIN-mediated cAMP release inhibition) but did not couple to β-arrestin 2 in a NanoBiT assay (**Figure 10a,b**). These results are in line with previous observations where removal of the last 13 amino acids of the carboxy-terminus of $CB_1R$ (TMSVSTDTSAEAL) or Ala-mutation of four phosphorylation sites in these amino acids (underlined) prevent agonist-induced internalization (Daigle *et al.*, 2008). The influence of the C-tail of $CB_1R$ in favouring a Gq/11 to Gi/o switch in 5-$HT_{2A}R$ coupling was studied by measuring Gq/11 dependent $[Ca^{2+}]i$ release at different $CB_1R^{\Delta 23}$:5-$HT_{2A}R$ ratios (**Figure 10c**). Clearly, in contrast to WT $CB_1R$, co-expression of $CB_1R^{\Delta 23}$ with 5-$HT_{2A}R$ retained canonical Gq/11 dependant $Ca^{2+}$ release upon 5 $HT_{2A}R$ activation. It is important to note that this effect is not caused by the lack of two Gi proteins being recruited by the heteromer because $CB_1R^{\Delta 23}$ displays Gi/o signalling (**Figure 10d**).

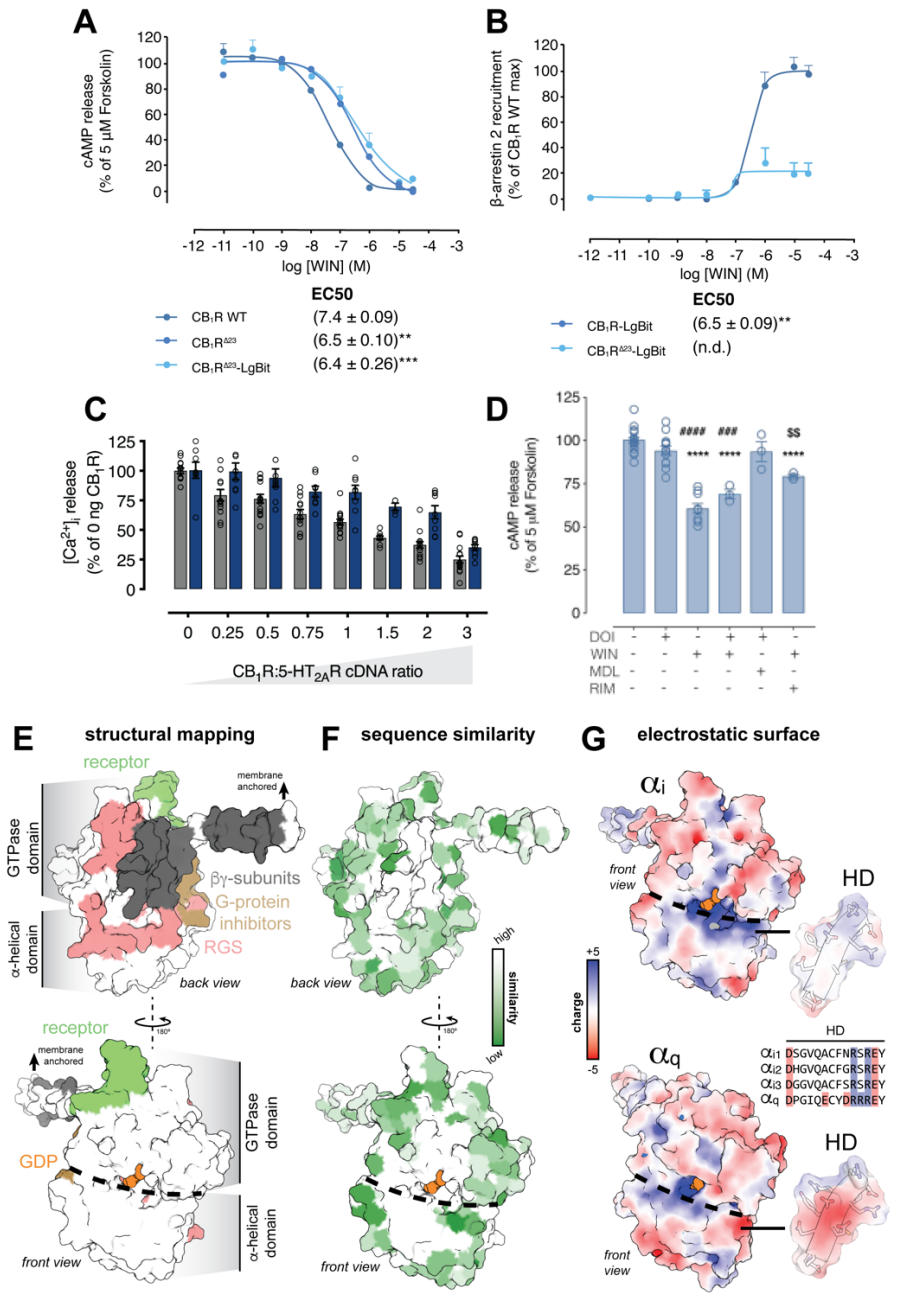


*Figure 10. The CB1R C-tail facilitates the G-protein class-switch.* **(a)** *CB1RΔ23 shows a decrease in the EC50 on cAMP accumulation assays, and* **(b)** *loses almost entirely its ability of recruiting β-arrestin 2. (continues)*

*(c) Intracellular $Ca^{2+}$ release in HEK 293 co-expressing a fix concentration of WT 5-$HT_{2A}$R and increasing concentrations of WT $CB_1$R or $CB_1R^{\Delta 23}$, stimulated with a saturating concentration (100 nM) of the 5-$HT_{2A}$R agonist DOI (n ≥ 3). Statistical significance was evaluated by two-way ANOVA followed by Bonferroni post hoc tests (*p ≤ 0.05, **p ≤ 0.01, ***p ≤ 0.0001, ****p ≤ 0.0001).* ***(d)*** *Effect of the $CB_1R^{\Delta 23}$ mutant in 5-$HT_{2A}$R-$CB_1$R heteromer-driven cross talk in cAMP. cAMP levels were evaluated as in* ***Figure 8****, with the exception that WIN was applied at 1 μM to reach $CB_1R^{\Delta 23}$ maximal occupancy. Values are mean ± SEM (n≥3) of percentage of activation normalised to forskolin maximal signal (cAMP). Statistical significance was evaluated by one-way ANOVA followed by Bonferroni post hoc test showing significant effects over basal activation levels (**p ≤ 0.01, ****p ≤ 0.0001), over DOI (###p ≤ 0.001, ####p ≤ 0.0001) or over WIN ($$p ≤ 0.01, $$$$p ≤ 0.0001).* ***(e-f)*** *Molecular surface of the α-subunit of the G-protein, viewed from two orientations, coloured by amino acids that interact with the receptor and βγ subunits (adapted from 7EZM and 8GHV), regulators of G-protein signalling (RGS) (adapted from 1SHZ and 1AGR), or the G-protein inhibitor YM-254890 (adapted from 3AH8) (**e**); and by sequence similarity between Gi/o and Gq/11, calculated from a 2D sequence alignment scored with the BLOSUM62 matrix (**f**). GDP in the binding site is shown as spheres. The position of the interface between α -helical and GTPase domains of the α-subunit is shown by a broken black line. G Electrostatic surface potentials of $\alpha_i$ and $\alpha_q$ (front view of panels E-F), calculated using the APBS program with the nonlinear Poisson-Boltzmann equation and contoured at ±5kT/e (negatively and positively charged surface areas are coloured red and blue, respectively). Detailed view of the HD helix of the α-helical domain in αi and αq and sequence alignment of HD to show that two negatively charged amino acids of αq are absent in αi.*

Instead, and in agreement to our hypothesis, $CB_1R^{\Delta 23}$ fails to achieve the optimal interactions via its C-tail and thus occludes Gi/o binding to the agonist-bound 5-$HT_{2A}$R protomer, as DOI did not inhibit FK-induced cAMP release in cells expressing both WT 5-$HT_{2A}$ and $CB1^{\Delta 23}$ receptors (**Figure 10d**).

We propose that the last 23 amino acids of the carboxy terminus of $CB_1$R interact with the α-subunit of the Gi/o-bound 5-$HT_{2A}$R to favor the switch from Gq/11 to Gi/o in 5-$HT_{2A}$R coupling. To computationally predict the $\alpha_{i/o}$ domain that interacts with these 23 amino acids, we first analyze molecular surfaces of $\alpha_{i/o}$ that interact with other proteins such as the receptor, the βγ subunits, regulators of G-protein signalling (RGS), or G-protein inhibitors. We assume that the carboxy terminus of $CB_1$R will not compete with these proteins for binding (back view in **Figure 10e**), so the molecular surface (front view) shaped by helices H3-H5 of the GTPase domain and HD-HG of the α-helical domain, as named by Flock et al.

(Flock *et al.*, 2015), are putative binding sites for the C-tail. Molecular surfaces of $\alpha_{i/o}$ and $\alpha_{q/11}$ colored by the conservation pattern (**Figure 10f**) and by the electrostatic potential (**Figure 10g**) are depicted. Clearly, the nucleotide binding cleft is highly conserved, but significant differences are observed in the HD and HG helices of the α-helical domain.

**Blind peptide docking and MD simulations show a putative interaction site for $CB_1R$ C-terminus on Gi/o**

We aim to predict the putative interaction points of the $CB_1R$ C-tail on the surface of the G-proteins, thus we used HPEPDOCK (Zhou, Li, *et al.*, 2018; Zhou, Jin, *et al.*, 2018), which can predict the binding mode of a peptide onto the surface of a protein (see METHODS). Thus, the 23-amino acids long peptide of $CB_1R$ C-tail (IKSTVKIAKVTMSVSTDTSAEAL) was docked onto $\alpha_{i/o}$ and $\alpha_{q/11}$ proteins. The structures of the Uniprot sequences P63096 of $\alpha_{i/o}$ and P50148 of $\alpha_{q/11}$ were obtained from the AlphaFold Protein Structure Database (Jumper *et al.*, 2021).

**Figure 11a** shows the best scored docking solutions of these 23 amino acids of the C-tail of $CB_1R$ bound to $\alpha_{i/o}$ and $\alpha_{q/11}$ that were not conflicting with other Gα interaction partners (**Figure 10e**). The C-tail of $CB_1R$ binds favorably at the interface between the α-helical and GTPase domains in $\alpha_{i/o}$, whereas it is not as favorable in the analogous area of $\alpha_{q/11}$. We hypothesize that the positive electrostatic surface potential at the interface between the α-helical and GTPase domains in $\alpha_{i/o}$, which is negative in $\alpha_{q/11}$ (**Figure 11b**), is responsible for the favorable binding of the negatively charged Asp466 and Glu470 (ST<u>D</u>TSA<u>E</u>AL) of the C-tail of $CB_1R$. Principally, helix HD of $\alpha_{q/11}$ is negative, due to the presence of two negatively charged Glu143 and Asp146 that are absent in $\alpha_{i/o}$ (see inset in **Figure 10g**). The stability of the docking models of the C-tail of $CB_1R$

to the interface between the α-helical and GTPase domains was evaluated by MD simulations. Complexes were introduced into a dodecahedron box, filled with TIP3P water molecules and counterions to ensure a neutral charge of the system. The main idea behind this approach is that the C-tail can favorably interact with $\alpha_{i/o}$, but not with $\alpha_{q/11}$. Starting from similar snapshots (see inset in **Figure 11b**) of the C-tail bound to $\alpha_{i/o}$ and $\alpha_{q/11}$, three replicas of 1 μs unrestrained MD trajectory show that the C-tail remains stable at the interface between the α-helical and GTPase domains only in $\alpha_{i/o}$ (**Figure 11b**), in agreement with our hypothesis.

Importantly, in the proposed quaternary structure of $CB_1R$-5-$HT_{2A}R$ heteromer (**Figure 9b**), the C-tail of the internal $CB_1R$ protomer points toward the $\alpha_{i/o}$ subunit of Gi/o bound to the external 5-$HT_{2A}R$ protomer (**Figure 9b**). This explains the fact that the last 23 amino acids of $CB_1R$ are key to favour the Gq/11 to Gi/o switch in 5-$HT_{2A}R$, since $CB_1R^{\Delta 23}$, lacking these amino acids, cannot trigger the G-protein switch in 5-$HT_{2A}R$ (**Figure 10**).

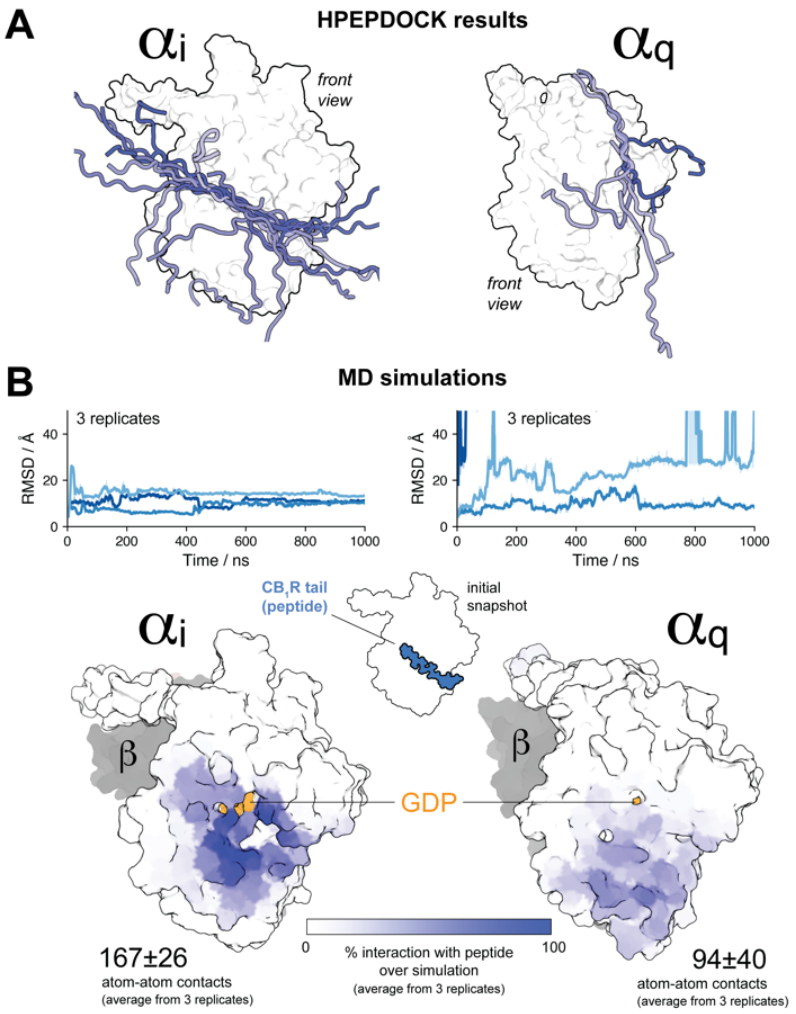


*Figure 11. The $CB_1R$ C-tail predicted to be more stable and more affine to $\alpha_i$ than $\alpha_q$.* ***(a)*** *Blind docking of the last 23 residues of the C-tail of $CB_1R$ on $\alpha_i$ and $\alpha_q$, performed with the HPEPDOCK webserver (Zhou, Jin, et al., 2018). 100 docking models were retrieved by only the poses that were not in conflict with the structural mapping in* ***Figure 10e*** *are shown.* ***(b)*** *Three replicate runs of 1 μs unrestrained MD simulations of $\alpha_i$ and $\alpha_q$ in complex with similar initial snapshots of the $CB_1R$ C-tail (see inset). The stability of the peptide was evaluated by the root mean-square deviation (rmsd) of the peptide heavy atoms. The interactions of the peptide with the α-subunit surface were also monitored. The darker the color, the more interactions have been stablished along the simulation.*

### 6.2.3 Discussion

We have shown here for the first time that confining $CB_1R$ into an inactive-like conformation, through mutant receptors that either block agonist-induced receptor activation or G-protein coupling, suffices to banish its allosteric effect on 5-$HT_{2A}R$ in the $CB_1R$-5-$HT_{2A}R$ heterotetramer. Thus, our results reveal that, in addition to the protein-protein transmembrane interface, disordered regions of the receptor and G-proteins also have a key component behind these allosteric interactions.

In conclusion, the data presented here on MOR-Gal1R (Case Study #3) and $CB_1R$-5-$HT_{2A}R$ (Case Study #4) heteromers, along with previous studies, support that the architecture of oligomers are key to their functional significance.

## 6.2.4 Supplementary Material

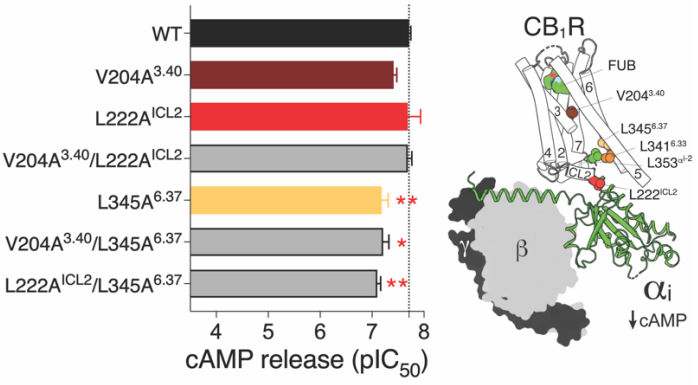


*Supplementary Figure 1. Functional validation of CB1 receptor mutants. Mean pIC50 ± SEM (n≥3) forskolin-induced (7.5μM) cAMP release inhibition for the $CB_1R$ mutants upon WIN 55212-2 stimulation. Statistical significance was evaluated by one-way analysis of variance (ANOVA) followed by Bonferroni post hoc tests (*p ≤0.05, **p ≤0.01).*

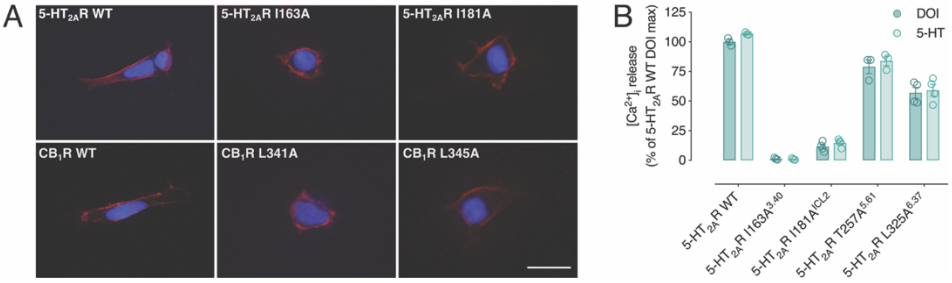


*Supplementary Figure 2. (**a**) Wildtype and mutant receptor surface expression monitored in HEK 293 cells. (**b**) Functional studies of the 5-HT2AR mutants, tested with both the agonist DOI and the endogenous ligand serotonin (5-HT).*

# 7 CHAPTER IV

*Receptor heteromerization alters the functional selectivity of ligands.*

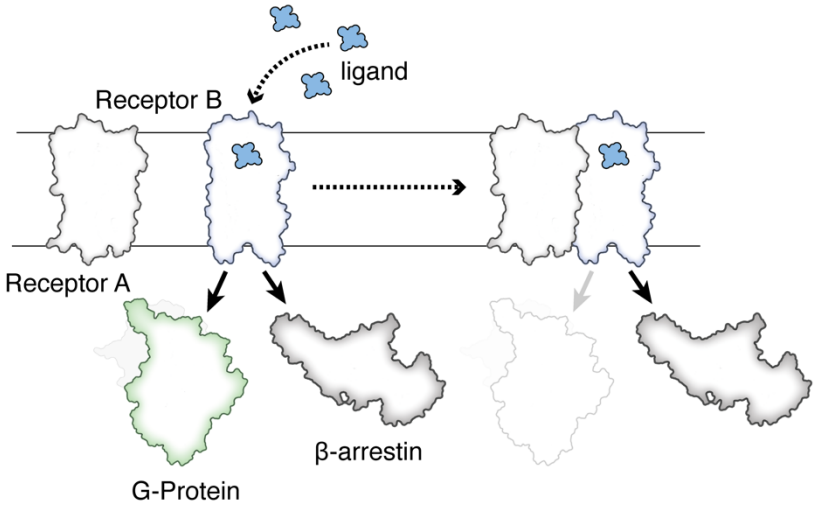

From the plethora of stimuli that GPCRs can recognize, the intracellular consequences are mainly mediated through G-proteins and β-arrestins.(Hilger, 2021). Generally, endogenous molecules show a balanced behavior in terms of activating one pathway over the other. However, there are certain synthetic molecules that can trigger specific conformations that favor the recruitment of the receptor by a β-arrestin instead of the coupling of a G-Protein, or vice versa, known as biased agonism or functional selectivity (Smith *et al.*, 2018). The preference of one pathway over the other can be tuned through a molecule, but it can also be influenced by interaction with other receptors. In a recent publication, Liu and colleagues demonstrated how the platelet-activating factor receptor shows a preference for G-protein signaling when oligomerizing (J. Liu *et al.*, 2022). In Case Study #5, a combination of both a $D_3R$ selective molecule (a bitopic ligand) and the interaction with $D_1R$, will functionally bias $D_3R$ signaling.

## 7.1 **Case Study #5.** Pharmacological targeting of the dopamine $D_1$-$D_3$ receptor heteromer.

Published as **co-first author** in

Moreno, E.[1], Casajuana-Martin, N.[1], Coyle, M., Campos Campos B., Galaj, E., Llinas del Torrent, C., Seyedian, A., Rea, W., Cai N-S., Bonifazi, A., Florán, B., Zheng-Xiong, X., Guitart, X., Casadó, V., Newman, A. H., Bishop, C., Pardo, L., Ferré., S. **Pharmacological targeting of G-protein-coupled receptor heteromers**. *Pharmacological Research*. 185 (2022)

[1]These authors contributed equally

### 7.1.1 Introduction

Classically, the psychomotor activity induced by stimulation of the dopaminergic system has been considered secondary to co-activation of segregated $D_1R$ and $D_2R$, respectively expressed by the GABAergic striato-nigral and striato-pallidal neurons (Starr *et al.*, 1987; Ferré, Giménez-Llort, *et al.*, 1994). The discovery of $D_3R$ and their predominant localization in striato-nigral neurons of the ventral striatum (Schwartz *et al.*, 1998), and the demonstration of functional and molecular interactions between striatal $D_1R$ and $D_3R$ disclosed a more direct cooperation between D1-like and D2-like receptors, the $D_1R$-$D_3R$ heteromer (Marcellino *et al.*, 2008; Fiorentini *et al.*, 2008; Guitart *et al.*, 2019, 2014).

Upregulation of otherwise sparsely expressed $D_3R$ in the dorsal striatum seems to be a main neurochemical mechanism associated with a side effect of chronic dopamine replacement therapy for Parkinson's disease known as L-DOPA-induced dyskinesia (LID) (Bordet *et al.*, 1997; Cote *et al.*, 2014; Cote and Kuzhikandathil, 2015; Lanza *et al.*, 2021; Farré *et al.*, 2015). It was then suggested that this implies an increase in $D_1R$-$D_3R$ heteromers with the concomitant synergistic effect secondary to $D_1R$ and

$D_3R$ co-activation (Ferré *et al.*, 2010). This hypothesis was strongly supported by results of experiments with a rat model of LID, which consists of analysis of abnormal involuntary movements in the rat with unilateral dopamine denervation and chronic L-DOPA treatment (Lundblad *et al.*, 2002). Hence, LID-like behavior in rats could be elicited by a $D_1R$ agonist and by a preferential $D_3R$ agonist, and co-administration of threshold doses of both agonists induced a synergistic effect (Lanza *et al.*, 2018). Furthermore, the development of LID-like behavior could be significantly attenuated by the specific genetic suppression of $D_3R$ in the $D_1R$-expressing cells of the dorsal striatum while L-DOPA efficacy was preserved (Lanza *et al.*, 2021).

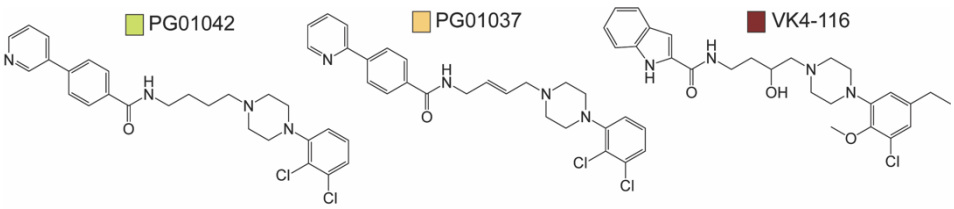


*Scheme 1. Structures of PG01042, PG01037, and VK4-116.*

These studies highlight $D_1R$-$D_3R$ heteromers in the dorsal striatum as promising pharmacological targets for LID. In fact, it was previously demonstrated the efficacy of two similar phenylpiperazine derivatives and very selective $D_3R$ ligands, PG01037 and PG01042 (see **Scheme 1**), in reducing LID-like behavior in rats (Kumar *et al.*, 2009; Riddle *et al.*, 2011). However, the two compounds demonstrated a very different pharmacological profile in cells transfected with $D_3R$. While PG01037 behaved as an antagonist of $D_3R$ agonist-induced AC inhibition and mitogenesis, PG01042 behaved as an agonist at inhibiting AC and as a weak partial agonist at activating mitogenesis (Riddle *et al.*, 2011). Therefore, the conundrum of how these two selective $D_3R$ ligands could

be pharmacologically different in vitro and yet promote the same in vivo pharmacological response had to be resolved. The results of the present study imply that the ability of both PG01037 and PG01042 to counteract LID-like behavior in rats can be explained by their ability to counteract $D_1R$-mediated signaling in the $D_1R$-$D_3R$ heteromer by means of different allosteric mechanisms. Moreover, the inability of another phenylpiperazine derivative and selective $D_3R$ ligand, VK4–116 (**Scheme 1**) (Kumar *et al.*, 2016), to counteract and even potentiate LID-like behavior in rats was associated with its inability to counteract $D_1R$ signaling and its ability to specifically promote β-arrestin recruitment by the $D_1R$-$D_3R$ heteromer.

Computational models of these ligands bound to $D_3R$ alone and upon oligomerization with the $D_1R$ provided potential molecular mechanisms involved in the $D_1R$-$D_3R$ heteromerization-dependent differential pharmacological effects of these three $D_3R$ ligands. Therefore, the present study strongly supports $D_1R$-$D_3R$ heteromers, and not $D_1R$ or $D_3R$, as main therapeutic targets in LID.

### 7.1.2 Results

**Behavioral profile of PG01042, PG01037 and VK4-116 in L-DOPA-induced dyskinetic rats**

The group at Binghamton University aim to test the behavioral profile of PG01042, PG01037 and VK4-116 compounds in reducing established LID in hemi-parkinsonian rats. Rats were monitored for development and expression of rodent dyskinesia using the AIMs (abnormal involuntary movements) rating scale, which has been validated pharmacologically through the administration of known anti-dyskinetic compounds (Dekundy *et al.*, 2007). Rats were placed in clear plexiglass cylinders (20 cm in

diameter x 25 cm in height) after L-DOPA injection and a trained observer, blind to experimental condition, rated axial, limb, and orolingual (ALO) behaviors beginning 10 min post-injection. ALO behaviors were rated for 60 s every 10 min for a total duration of 180 min, a procedure previously described (Dekundy *et al.*, 2007; Bishop *et al.*, 2012). For further details on the procedure the reader is referred to the Methods section in the original publication.

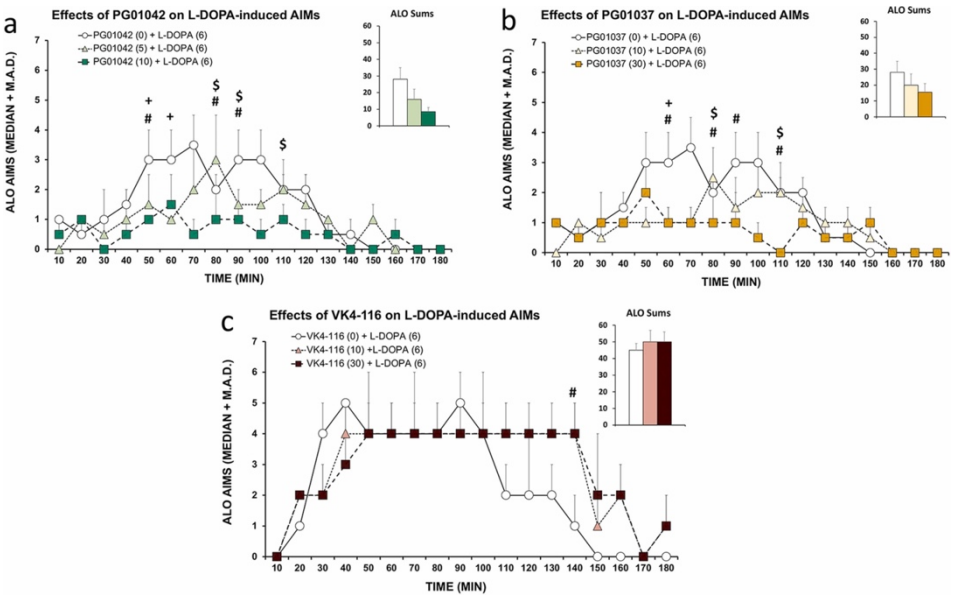


***Figure 1. Differential effects of PG01042, PG01037, and VK4–116 on L-DOPA-induced dyskinesia.*** *In* ***a*** *within-subjects, counterbalanced design, hemiparkinsonian rats previously rendered dyskinetic were treated with the $D_3R$ ligands (**a**) PG01042 (0, 5, 10 mg/kg; i.p.), (**b**) PG01037 (0, 10, 30 mg/kg; i.p.), or (**c**) VK4–116 (VK; 0, 10, 30 mg/kg; i.p.) prior to administration of L-DOPA (6 mg/kg; s.c.). Rats were rated for Axial, Limb and Orolingual (ALO) abnormal involuntary movements (AIMs) every 10 min for 180 min post-injection. AIMs time course and ALO sums are expressed as median + median absolute deviation (M.A.D.). Data were analyzed by non-parametric Friedman ANOVAs with Wilcoxon Match Pairs post-hoc tests. $^{+}$ $p < 0.05$ for Vehicle versus low dose, $^{\#}$ $p < 0.05$ for vehicle versus high dose, $^{\$}$ $p < 0.05$ for low dose versus high dose.*

The effects of the compounds of interest on ALO AIMs induced by repeated treatment with L-DOPA in rats with unilateral 6-OHDA-induced lesion of the left medial forebrain bundle (MFB) (an alternative LID model, see details in original publication) is shown in **Figure 1**. Several time-dependent and compound-dependent effects were revealed. With PG01042 (**Figure 1a**), rats receiving the low dose (5 mg/kg) demonstrated significantly less ALO AIMs than vehicle-treated rats at the 50 and 60 min timepoints while the high dose (10 mg/kg) attenuated LID expression relative to vehicle in rats at 50, 80 and 90 min-time points. Statistical differences were also found between the low and high doses at 80, 90, and 110 min timepoints. For PG01037 (**Figure 1b**), timepoint analyses revealed a significant suppressive effect of the low dose (10 mg/kg) on ALO AIMs 60 min following L-DOPA. The high dose of PG01037 (30 mg/kg) significantly reduced LID expression relative to vehicle treatment at the 60, 80, 90, and 110 min timepoints. Further, differences between AIMs expression in rats receiving the high vs low dose were found at 80 and 110 min such that the high dose significantly alleviated ALO AIMs more than the low dose. Interestingly, VK4–116 did influence severity of AIMs at a single late timepoint (140 min), but in the opposite direction (**Figure 1c**). Analysis revealed that the high dose of VK4–116 (30 mg/kg) increased ALO AIMs relative to vehicle ($p < 0.05$).

In conclusion, PG01042 and PG01037 show beneficial effects as these can counteract the LID phenotype in rats, whereas VK4-116 not only is unable but it has detrimental effects. However, it has been previously shown that in cells transfected only with $D_3R$ (Kumar *et al.*, 2009; Riddle *et al.*, 2011; Grundt *et al.*, 2005), PG01042 behaved as an agonist at inhibiting AC, and PG01037 and VK4–116 behaved as effective antagonists. This pharmacological profile in $D_3R$ cells disagrees with the

beneficial effects of PG01042 (agonist) and detrimental effect of VK4-116 (antagonist) on L-DOPA-induced dyskinesia (**Figure 1**). To solve this disagreement, it is necessary to analyze the pharmacological properties of these compounds in the $D_1R$-$D_3R$ heteromer.

**The heteromeric structure of $D_1R$-$D_3R$**

Before determining the signaling signatures of the $D_1R$-$D_3R$ heteromer, we need to explore its quaternary structure. It has been previously proposed a symmetrical TM 5/6 interface of the $D_1R$-$D_3R$ heteromer, based on the disrupting effects of TM5 and TM6 peptides of the $D_1R$ on BiFC and functional experiments (Guitart *et al.*, 2014, 2019). The group at UB performed additional BiFC experiments with TM peptides of both $D_1R$ and $D_3R$. HEK-293 T cells were co-transfected with $D_1R$ and $D_3R$ separately fused to complementary halves of YFP (N-terminal, $D_3R$-nYFP, or C-terminal, $D_1R$-cYFP). Confirming a symmetrical TM 5/6 interface, a statistically significant fluorescence decrease with TM5 and TM6 of both $D_1R$ and $D_3R$, but not with TM4 or TM7 peptides, was observed (**Figure 2a, b**).

The computational model of the $D_1R$-$D_3R$ heteromer was built using the $D_1R$ inactive state model (see METHODS, **Figure 6**). ECL2 of $D_1R$ is of particular interest because it is directly involved in the TM 5/6 interface, and before drawing any conclusions on the influence of $D_1R$ on its partner $D_3R$ protomer, it needed to be properly modelled and accommodated in the dimeric structure. In **Figure 2c,d**, the stability of the complex in the three unrestrained 1 $\mu$s MD simulations is monitored. The overall RMSF shows the high stability of the 7TM domains, and although the $D_1R$ ECL2 is slightly more flexible, it maintains the helical structure and the fold

towards $D_3R$ (**Figure 2c**). When monitoring the RMSD over simulation time, the overall stability can also be observed (**Figure 2d**).

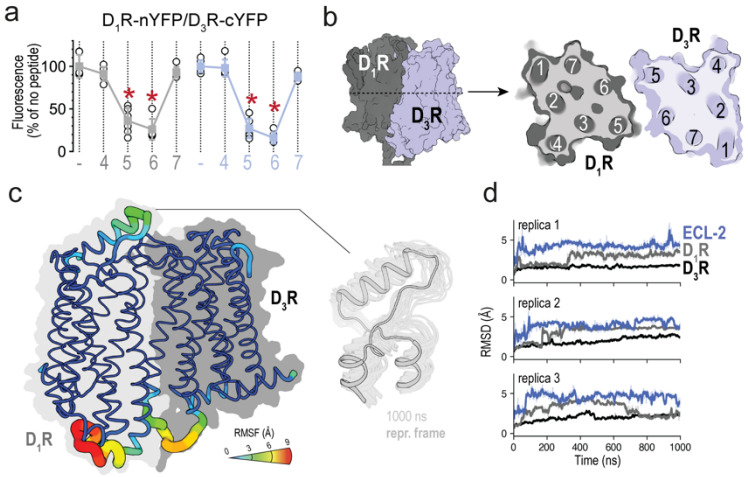


*Figure 2. The heteromeric structure of $D_1R$-$D_3R$. **(a)** Results from BiFC experiments in HEK-293 T cells co-transfected with $D_1R$-nYFP and $D_3R$-cYFP in the absence (-) or the presence of the indicated TM peptides (at 4 μM) from $D_1R$ (gray symbols and plots) or $D_3R$ (blue symbols and plots). Fluorescence values (in means ± S.D.) are expressed as the percentage of the fluorescence in the absence (-) of the indicated TM peptides (n = 6, with triplicates); ***: $p < 0.001$ versus control values (one-way ANOVA followed by Dunnett's post hoc comparisons). **(b)** The schemes illustrate extracellular and parallel to the membrane views of the computational model of the $D_1R$-$D_3R$ heteromer built using the TM 5/6 interface. **(c)** Average root-mean-square fluctuation (RMSF) of the $D_1R$-$D_3R$ heteromer is shown in the bottom panel. RMSF accounts for the average fluctuation of the structure along the simulation. A close-up of the ECL 2 is shown for one of the replicas. **(d)** RMSD vs simulation time plots are shown per replica for $D_1R$ and $D_3R$ and for the ECL2.*

## Effect of PG01042, PG01037 and VK4-116 on G-protein-dependent signaling

To analyze the properties of PG01042, PG01037, and VK4–116 in the $D_1R$-$D_3R$ heteromer, the group at UB first measured cAMP production in HEK-293 T cells co-transfected with $D_1R$, a Gs-coupled receptor, and $D_3R$, a Gi-coupled receptor. In agreement with previous results in cells with only $D_3R$, the agonist PG01042 significantly counteracted the effect of forskolin, both at 10 and 100 nM, with the highest concentration (100 nM)

being almost as effective as a high dose (30 nM) of the $D_3$R-agonist pramipexole (at 30 nM) ($D_3$Rago, **Figure 3a**). On the other hand, PG01037 and VK4–116 were not able to decrease cAMP, as anticipated from their antagonist profile (at 10 and 100 nM) (**Figure 3a**). We next analyzed possible allosteric interactions in the $D_1$R-$D_3$R heteromer by comparing the effect of simultaneously adding the $D_1$R agonist SKF81297 (at 30 nM) ($D_1$Rago) and PG01037 or VK4–116 in cells transfected only with $D_1$R (**Figure 3b**) with those transfected with $D_1$R and $D_3$R (**Figure 3c**). As expected, none of the selective $D_3$R ligands had any effect in SKF81297-induced cAMP production in cells transfected with only $D_1$R. In contrast, PG01042 significantly counteracted the SKF81297-mediated increase of cAMP, the canonical Gs-Gi antagonistic interaction at the AC level (type III allosterism, see INTRODUCTION). As expected, the canonical antagonistic interaction between SKF81297 and the PG01042 agonist was dependent on $D_1$R-$D_3$R heteromerization, since it was absent in cells only transfected with $D_1$R (**Figure 3b**) and in $D_1$R-$D_3$R transfected cells in the presence of the disrupting TM6 peptide (**Figure 3d**), but not in the presence of the control TM7 peptide (**Figure 3e**). Another previously described allosteric property of the $D_1$R-$D_3$R heteromer is cross-antagonism, by which a $D_3$R antagonist blocked $D_1$R-mediated signaling (Guitart *et al.*, 2014) (type I allosterism, see INTRODUCTION). Thus, cross-antagonism requires a direct $D_1$R-$D_3$R interaction since antagonists do not signal on their own. Interestingly, PG01037, but not VK4–116, blocked the SKF81297-mediated increase of cAMP (**Figure 3c**). The cross-antagonism of PG01037 was absent in cell expressing only $D_1$R and in the presence of the disruptive TM6 peptide of $D_1$R (**Figure 3d**), but not with the TM7 control peptide.

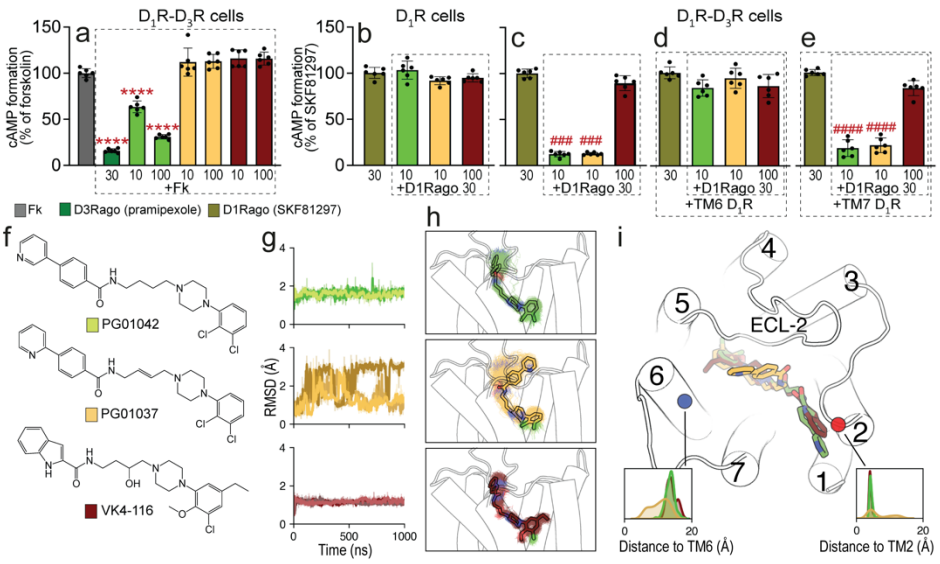


***Figure 3. Differential effects of PG01042, PG01037, and VK4–116 on G-protein-dependent signaling in HEK-293 T cells transfected with $D_3R$ and $D_1R$. (a-e)*** *Results from cAMP formation experiments in HEK-293T cells transfected with $D_1R$-Rluc cDNA (1 µg) with or without $D_3R$-YFP cDNA (1.5 µg) ($D_1R$-$D_3R$ cells and $D_1R$ cells, respectively). In a, cells are treated with the D2-like receptor agonist pramipexole ($D_3$Rago; 30 nM for 10 min) or the $D_3R$ ligands PG01042, PG01037 and VK4–116 (all at 10 or 100 nM for 15 min) before forskolin (Fk, 0.5 µM). In b-e, cells are pre-treated or not with $D_1R$ TM6 or TM7 peptides (4 µM for 4 h) and treated with PG01042 (10 nM), PG01037 (10 nM) and VK4–116 (100 nM) for 15 min before the $D_1R$ agonist SKF81297 (30 nM; $D_1$Rago). Values of cAMP formation are shown as mean ± S.D. (n = 6) and expressed as percentage of Fk-treated or $D_1$Rago-treated cells in each condition (100% represents 80–100 pmols cAMP/106 cells). ****: p < 0.0001 versus FK; ### and ####: p < 0.001 and p < 0.0001 versus $D_1$Rago, respectively (one-way ANOVA followed by Tukey's post hoc comparisons).* ***(f)*** *Chemical structures of PG01042 (green), PG01037 (orange) and VK4–116 (purple).* ***(g)*** *RMSD vs time plots of the ligands' heavy atoms and (h) representative structures (solid sticks) and evolution (lines) of the ligands in complex with $D_3R$ (white cylinders, only the initial structure is shown) as devised from three replicas of unbiased 1 µs MD simulations.* ***(i)*** *Distribution of the distances between the center of mass of the terminal ring in the second pharmacophore unit of these ligands and $N352^{6.58}$ in TM6 (blue dot) and $G93^{2.68}$ in TM2 (red dot). The second pharmacophore unit of PG01042 and VK4–116 remained stable at the ECD near TM2, whereas this part of PG01037 favors its interaction with TM6.*

To understand the pharmacological differences among PG01042, PG01037, and VK4–116 at the molecular level, we first performed three replicas of unbiased 1 µs MD simulations of the $D_3R$ monomer in the presence of these compounds (**Figure 3g-i**). These phenylpiperazine

compounds contain a primary and a second pharmacophore, linked by a spacer, which bind at the orthosteric binding pocket and at a secondary binding site (at the extracellular domain, ECD), respectively. RMSD of the simulations (**Figure 3g**) show that PG01042 and VK4–116 remained highly stable bound to the orthosteric and at a secondary pocket located at the extracellular part of TM2 (**Figure 3i**). In contrast, the second pharmacophore unit of PG01037 is unstable near TM2 and moves toward TM6 as shown by the large RMSD values and the probability density plots. This change is not due to the differential double bond located at the spacer (**Suppl. Figure 1**) but the hydrogen bond interaction between PG01037 and $Asn^{6.58}$ in TM6. These different binding modes prompt a different conformation of the ECD and TM6, which might therefore explain the respective presence and absence of cross-antagonism with PG01037 and VK4–116 binding.

**Effect of PG01042, PG01037 and VK4-116 on β-arrestin**

The ability of PG01042, PG01037, and VK4–116 to promote β-arrestin recruitment was evaluated in HEK-193T cells transiently transfected only with $D_3R$ (**Figure 4a**) and co-transfected with both $D_1R$ and $D_3R$ (**Figure 4b,c**). The full $D_3R$ agonist pramipexole significantly recruited β-arrestin in cell transfected with only $D_3R$, but neither PG01037 or PG01042 (10 nM) or VK4–116 (100 nM) were effective (**Figure 4a**). Notably, in cells co-expressing $D_1R$ and $D_3R$, a significant β-arrestin recruitment was selectively obtained with VK4–116, at 10 and 100 nM, which was ~60% the effect of a high concentration (30 nM) of pramipexole (**Figure 4b**). Neither PG01037 or PG01042, at 10 or 100 nM promoted a significant β-arrestin recruitment in $D_1R$-$D_3R$ transfected cells. We also compared the effect of the three ligands (at 10 nM) alone and in combination with pramipexole (30 nM) on β-arrestin recruitment from cells expressing $D_3R$

versus cells co-expressing $D_1R$ and $D_3R$ (**Suppl. Figure 2**). PG01042 and PG01037 counteracted the effect of pramipexole in cells expressing $D_3R$ or both $D_1R$ and $D_3R$, while VK4–116 only significantly counteracted pramipexole in $D_3R$ cells (**Suppl. Figure 2**). Thus, VK4–116 antagonizes $D_3R$ agonist-induced β-arrestin recruitment in $D_3R$-expressing cells, but it behaves as a β-arrestin biased agonist in cells co-expressing $D_1R$, inducing β-arrestin-recruitment when administered alone or combined with pramipexole. The experiments of VK4–116 on β-arrestin-recruitment in cells co-expressing $D_1R$ and $D_3R$ were repeated in the presence of TM6 and TM7 peptides of $D_1R$ (**Figure 4c**). Clearly, the ability of VK4–116 to promote β-arrestin recruitment was specifically lost in the presence of the disruptive peptide TM6 of $D_1R$, but not in the presence of the control peptide TM7 (**Figure 4c**). This indicates that β-arrestin recruitment induced by VK4–116 is dependent on $D_1R$-$D_3R$ heteromerization. Therefore, we can conclude that in the $D_1R$-$D_3R$ heteromer, PG01042 prompts a conformation of $D_3R$ that permits Gi binding (G-protein-biased agonism), PG01037 prompts a conformation of $D_3R$ that permits high complementarity with $D_1R$ (cross antagonism), and VK4–116 prompts a conformation of $D_3R$ that permits β-arrestin recruitment (β-arrestin-biased agonist).

The mechanism of agonist-induced receptor activation and G-protein binding is accurately characterized (see INTRODUCTION). Nonetheless, the mechanisms of agonist-induce β-arrestin recruitment and β-arrestin-biased agonism are not fully characterized. Significant advances have shown several signatures recently reviewed by Bock & Bermudez (Bock and Bermudez, 2021). First, bitopic ligands with extended binding modes toward the ECD might modulate binding pocket closure leading to ligand bias (Bermudez and Bock, 2019). Second, in the analogous dopamine D2

receptor (D2R), the movement of residues Ile184$^{ECL2}$ (McCorvy *et al.*, 2018) and Phe189$^{5.38}$ (Sanchez-Soto *et al.*, 2020) has been related to arrestin-biased agonism. Third, the interactions of biased agonists such as formoterol or salmeterol with amino acids in the orthosteric binding site of β1- or β2- adrenergic receptors, respectively, are different from the interactions of full agonists (Lee *et al.*, 2020; Masureel *et al.*, 2018). And fourth, the polar network in the receptor core can also act as a biased signaling switch, adopting conformations that can activate β-arrestin but not G-protein signaling (Wingler *et al.*, 2020). Because PG01037, PG01042, and VK4–116 are bitopic ligands interacting with amino acids at the ECD, we explored the conformation of the ECD and orientation of Ile183$^{ECL2}$ (homologous to Ile184$^{ECL2}$ in D2R), in MD simulations of the $D_3$R monomer. Our simulations show no significant differences in the conformation of Ile183$^{ECL2}$ among the ligands (**Suppl. Figure 3**), in agreement with the experimental data indicating that β-arrestin recruitment is dependent on $D_1$R-$D_3$R heteromerization (**Figures 4a-c**).

Thus, to understand the ability of VK4–116 to recruit β-arrestin we needed to perform similar MD simulations on the $D_1$R-$D_3$R heteromer. MD simulations of the $D_1$R-$D_3$R heteromer, modelled via the TM5/6 interface (**Figure 2**), show that $D_1$R significantly influences the conformation of $D_3$R, mainly moving the extracellular part of TMs 5, 6, and 7 (**Figure 4d**). Importantly, the movement of TM5 relocated ECL2 and the position of the key Ile183$^{ECL2}$ (**Figure 4e**). Thus, in contrast to the simulations of the $D_3$R protomer (**Suppl. Figure 3**), the VK4–116 biased agonist influences the conformation of Ile183$^{ECL2}$ in the $D_1$R-$D_3$R heteromer, relative to the other ligands and apo-$D_3$R (**Figure 4f**). The ethyl group of VK4–116 forms a hydrophobic interaction with Ile183$^{ECL2}$, as also proposed for biased agonists of $D_2$R (McCorvy *et al.*, 2018), which is absent in the other

ligands. This specific interaction of VK4–116 with Ile183$^{ECL2}$ moves inward the side chains conformations of Phe188$^{5.38}$ and Ser192$^{5.42}$ (**Figure 4g**). This causes a polar hydrogen bond network, via specific water molecules, between Ser192$^{5.42}$ and Thr115$^{3.37}$, as observed in angiotensin II type 1 receptor in complex with the biased agonist RTV023 (Wingler *et al.*, 2020). This binding mode of VK4–116 to the $D_1$R-$D_3$R heteromer may underlie its unique pharmacological properties as a biased agonist.

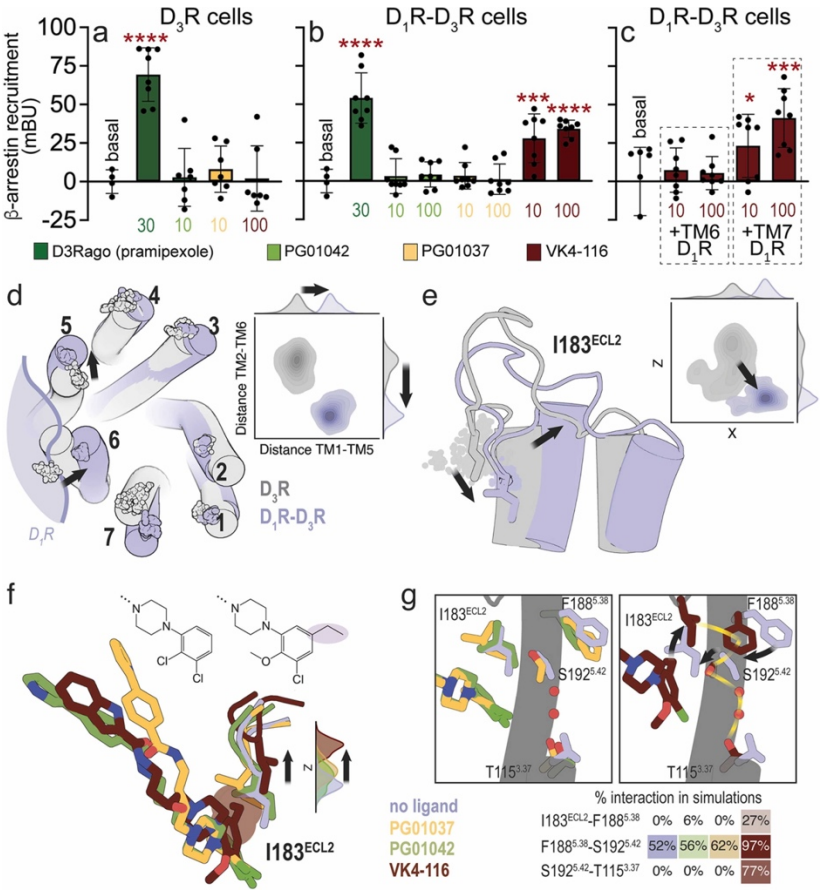


*Figure 4. Differential effects of PG01042, PG01037, and VK4–116 on β-arrestin recruitment in HEK-293 T cells transfected with $D_3$R and $D_1$R. (a-c)* *Results from β-arrestin recruitment experiments in HEK-293 T cells transfected with β-arrestin-1-Rluc cDNA (0.5 µg), $D_3$R-YFP cDNA (1 µg cDNA) with or without $D_1$R cDNA (1.5 µg cDNA) (D1R-D3R cells and D3R cells, respectively). (continues)*

*In **(a-b)**, cells are treated for 10 min with the $D_2$-like receptor agonist pramipexole (D3Rago; 30 nM) or the $D_3R$ ligands PG01042, PG01037 and VK4–116 (10 or 100 nM). In (c), cells are pre-treated or not with $D_1R$ TM6 or TM7 peptides (4 μM for 4 h) and with VK4–116 (10 or100 nM) for 15 min before the D1R agonist SKF81297 (30 nM; $D_1$Rago). Coelenterazine H (5 μM) was added before pramipexole or the selective $D_3R$ ligands for 7 min and β-arrestin-1 recruitment was measured by BRET (see Material and Methods in original publication). Values are mean ± S.D. (n = 8). *, *** and ****: $p < 0.05$, $p < 0.001$ and $p < 0.0001$ versus basal, respectively (one-way ANOVA followed by Dunnett's post hoc comparisons). (d) Evolution of the Cα atoms (spheres) of $Y32^{1.35}$ in TM1, $L89^{2.64}$ in TM2, $I101^{3.23}$ in TM3, $F170^{4.62}$ in TM4, $F188^{5.38}$ in TM5, $H354^{6.60}$ in TM6, and $P362^{7.32}$ in TM7 during three replicas of unbiased 1 μs MD simulations of the $D_3R$ monomer (gray) and the $D_1R$-$D_3R$ heteromer (blue) with no ligand bound. Contour plots of the distances between $Y32^{1.35}$ in TM1 and $F188^{5.38}$ in TM5 (distance TM1-TM5) and between $L89^{2.64}$ in TM2 and $H354^{6.60}$ in TM6 (distance TM2-TM6) during the MD simulations. Distributions of these distances are shown in the axes. **(e)** Evolution of $I183^{ECL2}$ (spheres), and contour plots and distributions of X,Z coordinates corresponding to the Cβ atom of $I183^{ECL2}$ during MD simulations. Black arrows represent the movements of $D_3R$ in the $D_1R$-$D_3R$ heteromer (blue) relative to the $D_3R$ protomer (gray). **(f)** Detailed view of $I183^{ECL2}$ of $D_3R$ in the $D_1R$-$D_3R$ heteromer during MD simulations with no ligand bound (blue) and PG01042 (green), PG01037 (orange) and VK4–116 (red) bound to $D_3R$. Distributions of the Z coordinate corresponding to the Cα atom of $I183^{ECL2}$ during MD simulations. The ethyl group of VK4–116 that triggers the upward movement of $I183^{ECL2}$ is highlighted. **(g)** Detailed views of $I183^{ECL2}$, $F188^{5.38}$, $S192^{5.42}$, and $T115^{3.37}$ of $D_3R$ in the $D_1R$-$D_3R$ heteromer during MD simulations with no ligand bound (blue) and PG01042 (green), PG01037 (orange) and VK4–116 (red) bound to $D_3R$. Frequency contacts (%) between side-chain residues, color-coded according to the ligand bound to $D_3R$, as calculated with the GetContacts software (https://getcontacts.github.io/). Black arrows represent the movements of these side chains of $D_3R$ relative to the unliganded $D_3R$ (blue). The xy plane is as defined by the Orientations of Proteins in Membranes (OPM) (Lomize et al., 2012).*

### 7.1.3 Discussion

In the present study we provide evidence for the three different types of allosteric interactions (see INTRODUCTION) in the $D_1R$-$D_3R$ heteromer involving three structurally related selective $D_3R$ ligands, all of them disclosed by the disruptive TM6 peptide of the $D_1R$:

- The cross-antagonism of PG01037, its ability to block SKF81297-induced AC activation, represents a type I allosterism.
- On the other hand, PG01042 promotes the same effect by a canonical Gs-Gi antagonistic interaction at the AC level, which represents a type III allosterism.

- Finally, the ability of VK4–116 to signal as a β-arrestin-biased agonist when the $D_3R$ heteromerizes with the $D_1R$, represents a ligand-independent type II allosterism.

Computational analysis provided possible explanations for the molecular mechanisms of the cross-antagonism of PG01037 and the β-arrestin functionally selective agonism of VK4–116 in the $D_1R$-$D_3R$ heteromer. We found a specific instability of the second pharmacophore unit of PG01037 near TM2 and its movement toward TM6 of the $D_3R$, which promotes a different conformation of TM6, which could favor the four-helix bundle interaction involving TM5 and TM6 of both receptors in the $D_1R$-$D_3R$ heteromeric interface, previously suggested to provide a mechanism for cross-antagonism in GPCR heteromers (Franco et al., 2021a). MD simulations of the $D_1R$-$D_3R$ heteromer, modelled via the TM5/6 interface, showed that $D_1R$ significantly influences the conformation of $D_3R$, mainly by moving the extracellular part of TMs 5, 6, and 7. The movement of TM5 of the $D_3R$ significantly changes the position of a key Ile residue of ECL2 ($Ile183^{ECL2}$), with which VK4–116, but not PG01037 and PG01042, can specifically interact and promote conformational changes that have been previously associated with biased β-arrestin agonism (See Results and ref. (Wingler *et al.*, 2020)).

The present study constitutes a proof of concept of the significant pharmacological role of GPCR heteromers. We can establish that, to be therapeutically effective in LID, $D_3R$ ligands should be either $D_3R$ antagonists (such as PG01037) or G-protein-biased $D_3R$ agonists (such as PG01042), specifically, at the $D_1R$-$D_3R$ heteromer. Thus, VK4–116 is an antagonist at the non-heteromerized $D_3R$, but its specific ability to behave as a β-arrestin-biased agonist at the $D_1R$-$D_3R$ heteromer might impede its potential antidyskinetic effect. Hence, when evaluating the role

of new $D_3R$ ligands as putative antidyskinetic agents, their pharmacological profile in cells expressing $D_1R$-$D_3R$ heteromers should be determined. In general, the present study implies that when suspecting its pathogenetic role, a GPCR heteromer, and not its individual GPCR units, should be considered as a main target for drug development.

## 7.1.4 Supplementary Material

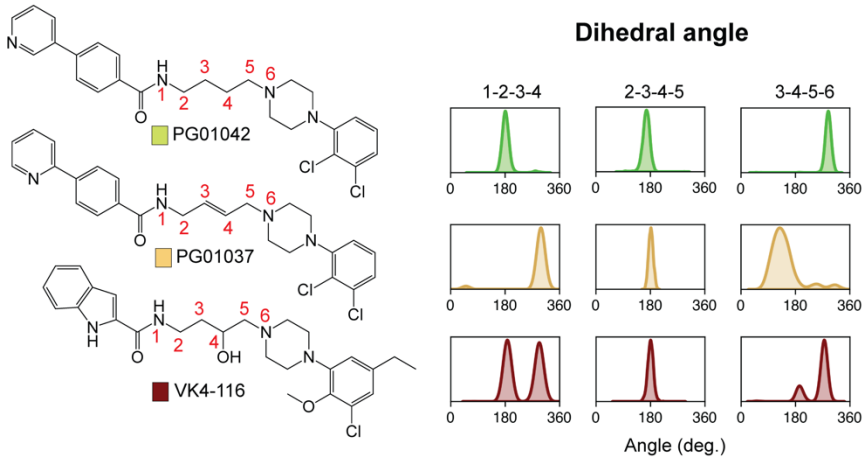


***Supplementary Figure 1. Distribution of dihedral angles of PG01042, PG01037, and VK4-116 in the simulations of their complexes with $D_3R$.*** *The dihedral angles are calculated for the chain linking both pharmacophore units. Each plot accounts for the accumulated distribution of the three replicates. Atoms involved in the angles are referenced in red in the 2D structures.*

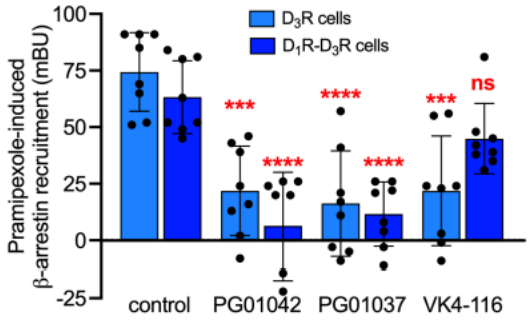


***Supplementary Figure 2. Differential effects of PG01042, PG01037, and VK4-116 on pramipexole-induced β-arrestin recruitment in HEK-293T cells transfected with $D_3R$ alone or with $D_1R$.*** *Results from β-arrestin recruitment experiments in HEK-293T cells transfected with β-arrestin-1-Rluc cDNA (0.5 µg),$D_3R$-YFP cDNA (1 µg cDNA) with or without $D_1R$ cDNA (1.5 µg cDNA) ($D_1R$-$D_3R$ cells and $D_3R$ cells, respectively). Cells are treated for 10 min with the D2-like receptor agonist pramipexole (30 nM) or the$D_3R$ ligands PG01042, PG01037 and VK4-116 (10 nM). Coelenterazine H (5 µM) was added before pramipexole or the selective $D_3R$ ligands for 7 minutes and β-arrestin-1 recruitment was measured by BRET (see Material and Methods). Values are mean ± S.D. (n = 8). ***, **** or ns: $p < 0.001$, $p < 0.0001$ or not significant ($p > 0.05$) versus corresponding $D_3R$ or $D_1R$-$D_3R$ cells only treated with pramipexole (control) (one-way ANOVA followed by Dunnett's post hoc comparisons).*

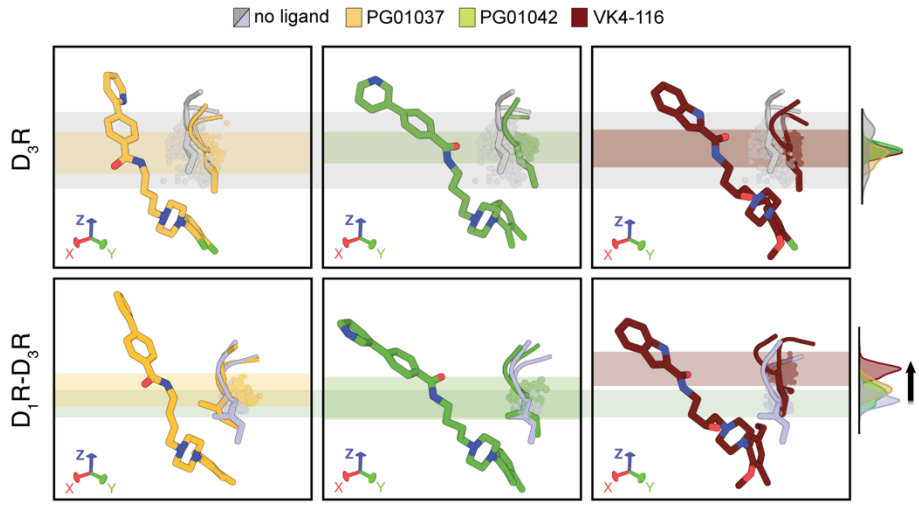


***Supplementary Figure 3. Comparison of $D_3R$ I183 behavior in MD simulations with the $D_3R$ monomer and $D_1R$-$D_3R$.*** *View of I183 of $D_3R$ during MD simulations with no ligand bound (gray if monomer, light blue if $D_1R$-$D_3R$) and PG01042 (green), PG01037 (orange) and VK4-116 (red) bound to $D_3R$. Distributions of the Z coordinate corresponding to the Ca atom of $I183^{ECL2}$ during MD simulations. The range of the Z coordinate during the MD simulations are shown by the rectangles, color-coded according to the ligand bound. No significant differences in the position of $I183^{ECL2}$ between ligands are observed.*

# 8 CONCLUSIONS

Protein-protein interactions play an essential role in coordinating cell machinery. GPCRs are not an exception to this rule, and can engage protein-protein interactions with each other, by forming complexes constituted by the same (homo) or different (hetero) receptor protomers, for increased diversification and complexity of signaling. Along the lines of this thesis, we have explored several key allosteric mechanisms at the molecular level.

The conclusions can be summarized as follows:

1. The dimerization dynamics of the $A_{2A}R$-$D_2R$ heteromer are influenced by the three studied antipsychotic drugs. Clozapine decreases heteromer formation by means of a bulky aromatic moiety, which points towards the TMs 4 and 5 on $D_2R$ influencing the dimer interface. Aripiprazole and haloperidol increase the formation of heteromer by means of its extended binding mode, that stabilizes a conformation of ECL2 of $D_2R$ that makes the dimeric interface more energetically favorable.

2. The presence of Gal1R influences the pharmacodynamic properties of (S)-methadone on MOR, which explain the lower addictive liability observed in treatment with racemic methadone. This pharmacological difference is due to a rearrangement of the MOR/MOR homodimeric interface induced by the interaction with Gal1R. The dimeric rearrangement modifies the shape of the MOR binding pocket. This different pocket decreases the affinity and efficacy of (S)-methadone, but not (R)-methadone.

3. The presence of MOR modifies the G-protein coupling pattern of Gal1R in the MOR-Gal1R heterotetramer. The computational and experimental results indicate that the ability of Gs to couple to the Gal1R-Gal1R homodimer, instead of canonical Gi/o, is determined by the change in its

homomeric interface from TM5/6 to TM4/5 induced by heteromerization with MOR.

4. The presence of $CB_1R$ modifies the G-protein coupling preference of 5-$HT_{2A}R$. We have shown that $CB_1R^{\Delta 23}$, lacking the last 23 amino acids of the C-terminal domain, cannot trigger the Gq/11 to Gi/o switch in 5-HT2AR coupling. Computational models suggest that the C-tail of CB1R plays an important role by binding at the interface between the α-helical and GTPase domains of $\alpha_{i/o}$ in the Gi/o-bound 5-$HT_{2A}R$ for the heteromer specific signaling.

5. $D_1R$ modifies the functional selectivity of a series of $D_3R$ selective compounds by forming $D_1R$-$D_3R$ heteromers. The presence of $D_1R$ alters the $D_3R$ binding pocket, particularly ECL2 and TMs 5 and 6. This change allows VK4-116 to switch from an antagonist in $D_3R$ to a β-arrestin biased agonist in $D_1R$-$D_3R$.

Finally, this thesis has shown the benefits of integrating computational studies in experimental research to increase understanding of observed phenomena and guide future experiments (**Figure 1**).


*Figure 1. Taken from (Sperger et al., 2016).*

## 8.1 List of publications

### *Included in the thesis*

1. Botta, J.[1], Chunilal, V.[1], Casajuana-Martin, N.[1], Bondar, A., D'augello, I., Llinas del Torrent, C., Howell, L. A., Contino, M-A., Guzmán, M., Lazar, J., Pardo, L., McCormick, P. J. **The C-tail of functional cannabinoid receptor 1 ($CB_1R$) facilitates the G-protein class-switch of serotonin 5-$HT_{2A}$ receptor (5-$HT_{2A}R$) in the $CB_1R$-5-$HT_{2A}R$ heteromer**. *Science Signaling*, submitted.

2. Levinstein, M.[1], de Oliveira, P. A.[1], Casajuana-Martin, N.[1], Quiroz, C., Budinich, R., Rais, R., Rea, W., Ventriglia, E., Llopart, N., Casadó-Anguera, V., Moreno, E., Walther, D., Glatfelter, G., Weinshenker, D., Zarate, C., Casado, V., Baumann, M., Pardo, L., Ferré, S., Michaelides, M. **Unique pharmacodynamic properties and low abuse liability of the *μ*-opioid receptor ligand (S)-methadone**. *Molecular Psychiatry*, in press (2023)

3. Valle-León, M.[1], Casajuana-Martin, N.[1], Llinas del Torrent, C., Argerich, J., Gómez-Acero, L., Sahlholm, K., Ferré, S., Pardo, L., Ciruela, F. **Unique Effect of Clozapine on Adenosine $A_{2A}$-Dopamine $D_2$ Receptor Heteromerization.** *Biomedicine & Pharmacotherapy*, 160, 114327 (2023)

4. De Oliveira, P. A.[1], Moreno, E.[1], Casajuana-Martin, N.[1], Casadó-Anguera, V., Cai N-S., Camacho-Hernandez, G. A., Zhu, H., Bonifazi, A., Hall, M. D., Weinshenker, D., Newman, A. H., Logothetis, D. E., Casadó, V., Plant, L. D., Pardo, L., Ferré, S. **Preferential Gs protein coupling of the galanin Gal1 receptor in the *μ*-opioid-Gal1 receptor heterotetramer**. *Pharmacological Research*, 182, 106322 (2022)

5. Moreno, E.[1], Casajuana-Martin, N.[1], Coyle, M., Campos Campos B., Galaj, E., Llinas del Torrent, C., Seyedian, A., Rea, W., Cai N-S., Bonifazi, A., Florán, B., Zheng-Xiong, X., Guitart, X., Casadó, V., Newman, A. H., Bishop, C., Pardo, L., Ferré., S. **Pharmacological targeting of G-protein-coupled receptor heteromers**. *Pharmacological Research,* 185, 106476 (2022)

[1]These authors contributed equally

## *Others*

6. Llinas del Torrent, C., Raïch, I., Gonzalez, A., Lillo, J., Casajuana-Martin, N., Franco, R., Pardo, L. & Navarro, G. **Allosterism in the adenosine $A_{2A}$ and cannabinoid $CB_2$ heteromer**. *British Journal of Pharmacology*, in press (2024)

7. Llinas del Torrent, C., Raïch, I., Gonzalez, A., Casajuana-Martin, N., Lillo, J., Rebassa, J. B., Ferreiro-Vera, C., Sánchez de Medina, V., Franco, R., Navarro, G., Pardo, L. **The Leu/Val$^{6.51}$ side chain of cannabinoid receptors regulates the binding mode of the alkyl chain of $\Delta^9$-tetrahydrocannabinol.** *Journal of Chemical Information and Modelling*, 63, 5927-5935 (2023)

8. Casajuana-Martin, N., Navarro, G., Gonzalez, A., Llinas del Torrent, C., Gómez-Autet, M., Quintana-García, A., Franco, R., Pardo, L. **A single point mutation blocks the entrance of ligands to the cannabinoid $CB_2$ receptor**. *Journal Chemical Information and Modeling*, 62, 5771-5779 (2022)

9. Sarasola, L. I., Llinas del Torrent, C., Pérez-Arévalo, A., Argerich, J., Casajuana-Martin, N., Chevigné, A., Fernández-Dueñas, V., Ferré, S., Pardo, L., Ciruela, F. **The ADORA1 mutation linked to early-onset Parkinson's disease alters adenosine $A_1$-$A_{2A}$ receptor heteromer formation and function**. *Biomedicine & Pharmacotherapy*, 156, 113896 (2022)

10. Pulido, D., Casadó-Anguera, V., Gómez-Autet, M., Llopart, N., Moreno, E., Casajuana-Martin, N., Ferré, S., Pardo, L. **Heterobivalent Ligand for the Adenosine $A_{2A}$–Dopamine $D_2$ Receptor Heteromer**. *Journal of Medicinal Chemistry*, 65, 616–632 (2022)

11. Navarro, G., Gonzalez, A., Sánchez-Morales, A., Casajuana-Martin, N., Gómez-Ventura, M., Cordomí, A., Busqué, F., Alibés, R., Pardo, L., Franco, R. **Design of Negative and Positive Allosteric Modulators of the Cannabinoid $CB_2$ Receptor Derived from the Natural Product Cannabidiol**. *Journal of Medicinal Chemistry*, 64, 9354–9364 (2021)

12. Cierco-Jimenez, R., Casajuana-Martin, N., García-Recio, A., Alcántara, L., Pardo, L., Campillo, M., Gonzalez, A. **The mutational landscape of human olfactory G-protein-coupled receptors**. *BMC Biology*, 19, 21 (2021)

13. Navarro, G., Gonzalez, A., Campanacci, S., Rivas-Santisteban, R., Reyes-Resina, I., Casajuana-Martin, N., Cordomí A., Pardo, L., Franco, R. **Experimental and computational analysis of biased agonism on full-length and a C-terminally truncated adenosine $A_{2A}$ receptor**. *Computational and Structural Biotechnology Journal*, 18, 2723-2732 (2020)

14. Llinas del Torrent, C., Casajuana-Martin, N., Pardo, L., Tresadern, G., Pérez-Benito, L., **Mechanisms Underlying Allosteric Molecular Switches of Metabotropic Glutamate Receptor 5**. *Journal of Chemical Information and Modelling*, 59, 2456–2466 (2019)

15. Pérez-Benito, L., Casajuana-Martin, N., Jimenez-Rosés, M., van Vlijmen, H., Tresadern G. **Predicting Activity Cliffs with Free-Energy Perturbation**. *Journal of Chemical Theory and Computation*, 15, 1884–1895 (2019)

# 9 REFERENCES

Abraham,M.J. et al. (2015) GROMACS: High performance molecular simulations through multi-level parallelism from laptops to supercomputers. SoftwareX, 1–2, 19–25.

Albizu,L. et al. (2010) Time-resolved FRET between GPCR ligands reveals oligomers in native tissues. Nature Chemical Biology 2010 6:8, 6, 587–594.

Alegre,K.O. et al. (2021) Structural basis and mechanism of activation of two different families of G-proteins by the same GPCR. Nature Structural & Molecular Biology 2021 28:11, 28, 936–944.

Alexander,S.P.H. et al. (2019) THE CONCISE GUIDE TO PHARMACOLOGY 2019/20: G-protein-coupled receptors. Br J Pharmacol, 176, S21–S141.

Altschul,S.F. et al. (1990) Basic local alignment search tool. J Mol Biol, 215, 403–410.

Aranda-Garcia,D. et al. (2022) Simulating Time-Resolved Dynamics of Biomolecular Systems. Comprehensive Pharmacology, 2, 115–134.

Avet,C. et al. (2022) Effector membrane translocation biosensors reveal G-protein and Parrestin coupling profiles of 100 therapeutically relevant GPCRs. Elife, 11.

Bai,M. et al. (1998) Dimerization of the extracellular calcium-sensing receptor (CaR) on the cell surface of CaR-transfected HEK293 cells. Journal of Biological Chemistry, 273, 23605–23610.

Ballesteros,J.A. and Weinstein,H. (1995) Integrated methods for the construction of three-dimensional models and computational probing of structure-function relations in G-protein-coupled receptors. Methods in Neurosciences, 25, 366–428.

Bayly,C.I. et al. (1993) A well-behaved electrostatic potential based method using charge restraints for deriving atomic charges: The RESP model. Journal of Physical Chemistry, 97, 10269–10280.

Beaulieu,J.M. and Gainetdinov,R.R. (2011) The physiology, signaling, and pharmacology of dopamine receptors. Pharmacol Rev, 63, 182–217.

Berger,O. et al. (1997) Molecular dynamics simulations of a fluid bilayer of dipalmitoylphosphatidylcholine at full hydration, constant pressure, and constant temperature. Biophys J, 72, 2002–2013.

Bermudez,M. and Bock,A. (2019) Does Divergent Binding Pocket Closure Drive Ligand Bias for Class A GPCRs? Trends Pharmacol Sci, 40, 236–239.

Bernstein,G. et al. (2019) Characterization of the Safety and Pharmacokinetic Profile of d -Methadone, a Novel N -Methyl- d -Aspartate Receptor Antagonist in Healthy, Opioid-Naive Subjects: Results of Two Phase 1 Studies. J Clin Psychopharmacol, 39, 226–237.

Bishop,C. et al. (2012) Serotonin transporter inhibition attenuates l-DOPA-induced dyskinesia without compromising l-DOPA efficacy in hemi-parkinsonian rats. European Journal of Neuroscience, 36, 2839–2848.

Bock,A. and Bermudez,M. (2021) Allosteric coupling and biased agonism in G-protein-coupled receptors. FEBS Journal, 288, 2513–2528.

Bonaventura,J. et al. (2015) Allosteric interactions between agonists and antagonists within the adenosine A2A receptordopamine D2 receptor heterotetramer. Proc Natl Acad Sci U S A, 112, E3609–E3618.

Bondar,A. and Lazar,J. (2017) The G-protein Gi1 exhibits basal coupling but not preassembly with G-protein-coupled receptors. J Biol Chem, 292, 9690.

Bordet,R. et al. (1997) Induction of dopamine D3 receptor expression as a mechanism of behavioral sensitization to levodopa. Proc Natl Acad Sci U S A, 94, 3363–3367.

Borroto-Escuela,D.O. et al. (2014) The G-protein-coupled receptor heterodimer network (GPCR-HetNet) and its hub components. Int J Mol Sci, 15, 8570–8590.

Botta,J. et al. (2019) Design and development of stapled transmembrane peptides that disrupt the activity of G-protein-coupled receptor oligomers. J Biol Chem, 294, 16587–16603.

Brogi,S. et al. (2014) Discovery of GPCR ligands for probing signal transduction pathways. Front Pharmacol, 5, 119795.

Bushdid,C. et al. (2014) Humans can discriminate more than 1 trillion olfactory stimuli. Science (1979), 343, 1370–1372.

Cai,N.S. et al. (2019) Opioid-galanin receptor heteromers mediate the dopaminergic effects of opioids. Journal of Clinical Investigation, 129, 2730–2744.

Callaway,E. (2015) The revolution will not be crystallized: A new method sweeps through structural biology. Nature, 525, 172–174.

Capponi,A.M. and Catt,K.J. (1980) Solubilization and characterization of adrenal and uterine angiotensin II receptors after photoaffinity labeling. Journal of Biological Chemistry, 255, 12081–12086.

Carrillo,J.J. et al. (2004) Multiple Interactions between Transmembrane Helices Generate the Oligomeric α1b-Adrenoceptor. Mol Pharmacol, 66, 1123–1137.

Casiraghi,M. (2023) Biophysical investigations of class A GPCRs. Biochimie, 205, 86–94.

Changeux,J.P. and Edelstein,S.J. (2005) Allosteric mechanisms of signal transduction. Science (1979), 308, 1424–1428.

Che,T. and Roth,B.L. (2021) Structural Insights Accelerate the Discovery of Opioid Alternatives. https://doi.org/10.1146/annurev-biochem-061620-044044, 90, 739–761.

CHEN,K.K. (1948) Pharmacology of methadone and related compounds. Ann N Y Acad Sci, 51, 83–97.

Chen,Q. et al. (2021) Structures of rhodopsin in complex with G-protein-coupled receptor kinase 1. Nature 2021 595:7868, 595, 600–605.

Chen,T.W. et al. (2013) Ultrasensitive fluorescent proteins for imaging neuronal activity. Nature 2013 499:7458, 499, 295–300.

Cherezov,V. et al. (2007) High-resolution crystal structure of an engineered human β2-adrenergic G-protein-coupled receptor. Science (1979), 318, 1258–1265.

Christopoulos,A. (2014) Advances in G-protein-Coupled Receptor Allostery: From Function to Structure. Mol Pharmacol, 86, 463–478.

Ciruela,F. et al. (2010) Lighting up multiprotein complexes: Lessons from GPCR oligomerization. Trends Biotechnol, 28, 407–415.

Cote,S.R. et al. (2014) Overexpression of the dopamine D3 receptor in the rat dorsal striatum induces dyskinetic behaviors. Behavioural Brain Research, 263, 46–50.

Cote,S.R. and Kuzhikandathil,E. V. (2015) Chronic levodopa treatment alters expression and function of dopamine D3 receptor in the MPTP/p mouse model of Parkinson's disease. Neurosci Lett, 585, 33–37.

Dagan-Wiener,A. et al. (2019) Bitterdb: Taste ligands and receptors database in 2019. Nucleic Acids Res, 47, D1179–D1185.

Daigle,T.L. et al. (2008) Regulation of CB1 cannabinoid receptor internalization by a promiscuous phosphorylation-dependent mechanism. J Neurochem, 106, 70–82.

Day,M. et al. (2002) Stimulation of 5-HT(2) receptors in prefrontal pyramidal neurons inhibits Ca(v)1.2 L type Ca(2+) currents via a PLCbeta/IP3/calcineurin signaling cascade. J Neurophysiol, 87, 2490–2504.

Day,P.W. et al. (2007) A monoclonal antibody for G-protein-coupled receptor crystallography. Nat Methods, 4, 927–929.

Dekundy,A. et al. (2007) Modulation of l-DOPA-induced abnormal involuntary movements by clinically tested compounds: Further validation of the rat dyskinesia model. Behavioural Brain Research, 179, 76–89.

Deupi,X. et al. (2007) Structural Models of Class A G-protein-Coupled Receptors as a Tool for Drug Design: Insights on Transmembrane Bundle Plasticity. Curr Top Med Chem, 7, 991–998.

Dickson,C.J. et al. (2014) Lipid14: The amber lipid force field. J Chem Theory Comput, 10, 865–879.

Dixon,A.S. et al. (2016) NanoLuc Complementation Reporter Optimized for Accurate Measurement of Protein Interactions in Cells. ACS Chem Biol, 11, 400–408.

Dolinsky,T.J. et al. (2004) PDB2PQR: an automated pipeline for the setup of Poisson-Boltzmann electrostatics calculations. Nucleic Acids Res, 32.

Dror,R.O. et al. (2011) Pathway and mechanism of drug binding to G-protein-coupled receptors. Proc Natl Acad Sci U S A, 108, 13118–13123.

Dror,R.O. et al. (2015) Structural basis for nucleotide exchange in heterotrimeric G-proteins. Science (1979), 348, 1361–1365.

Du,J. et al. (2021) Structures of human mGlu2 and mGlu7 homo- and heterodimers. Nature 2021 594:7864, 594, 589–593.

Duan,J. et al. (2022) Molecular basis for allosteric agonism and G-protein subtype selectivity of galanin receptors. Nature Communications 2022 13:1, 13, 1–13.

Eberhardt,J. et al. (2021) AutoDock Vina 1.2.0: New Docking Methods, Expanded Force Field, and Python Bindings. J Chem Inf Model, 61, 3891–3898.

Eswar,N. et al. (2006) Comparative protein structure modeling using Modeller. Curr Protoc Bioinformatics, Chapter 5.

Fan,L. et al. (2020) Haloperidol bound D2 dopamine receptor structure inspired the discovery of subtype selective ligands. Nat Commun, 11.

Farré,D. et al. (2015) Stronger Dopamine D1 Receptor-Mediated Neurotransmission in Dyskinesia. Mol Neurobiol, 52, 1408–1420.

Fava,M. et al. (2022) REL-1017 (Esmethadone) as Adjunctive Treatment in Patients With Major Depressive Disorder: A Phase 2a Randomized Double-Blind Trial. Am J Psychiatry, 179, 122–131.

Ferré,S. et al. (1992) Adenosine-dopamine interactions in the brain. Neuroscience, 51, 501–512.

Ferré,S. et al. (2009) Building a new conceptual framework for receptor heteromers. Nat Chem Biol, 5, 131.

Ferré,S., Schwarcz,R., et al. (1994) Chronic haloperidol treatment leads to an increase in the intramembrane interaction between adenosine A2 and dopamine D2 receptors in the neostriatum. Psychopharmacology (Berl), 116, 279–284.

Ferré,S. et al. (2010) G-protein-coupled receptor heteromers as new targets for drug development. Prog Mol Biol Transl Sci, 91, 41–52.

Ferré,S. et al. (2014) G-protein-coupled receptor oligomerization revisited: Functional and pharmacological perspectives. Pharmacol Rev, 66, 413–434.

Ferré,S. et al. (2022) G-protein-coupled receptor-effector macromolecular membrane assemblies (GEMMAs). Pharmacol Ther, 231.

Ferré,S. (2016) Mechanisms of the psychostimulant effects of caffeine: implications for substance use disorders. Psychopharmacology (Berl), 233, 1963–1979.

Ferré,S., Giménez-Llort,L., et al. (1994) Motor activation in short- and long-term reserpinized mice: role of N-methyl-D-aspartate, dopamine D1 and dopamine D2 receptors. Eur J Pharmacol, 255, 203–213.

Ferré,S. et al. (2020) Oligomerization of G-protein-coupled receptors: Still doubted? Prog Mol Biol Transl Sci, 169, 297–321.

Ferré,S. (2015) The GPCR heterotetramer: Challenging classical pharmacology. Trends Pharmacol Sci, 36, 145–152.

Fiorentini,C. et al. (2008) Reciprocal regulation of dopamine D1 and D3 receptor function and trafficking by heterodimerization. Mol Pharmacol, 74, 59–69.

Fiser,A. et al. (2000) Modeling of loops in protein structures. Protein Sci, 9, 1753–1773.

Flock,T. et al. (2017) Selectivity determinants of GPCR–G-protein binding. Nature 2017 545:7654, 545, 317–322.

Flock,T. et al. (2015) Universal allosteric mechanism for Gα activation by GPCRs. Nature, 524, 173–179.

Fogaça,M. V. et al. (2019) N-Methyl-D-aspartate receptor antagonist d-methadone produces rapid, mTORC1-dependent antidepressant effects. Neuropsychopharmacology, 44, 2230–2238.

Fotiadis,D. et al. (2003) Rhodopsin dimers in native disc membranes. Nature 2003 421:6919, 421, 127–128.

Franco,R. et al. (2021) Structure and function of adenosine receptor heteromers. Cellular and Molecular Life Sciences, 78, 3957–3968.

Fraser,C.M. and Venter,J.C. (1982) The size of the mammalian lung β2-adrenergic receptor as determined by target size analysis and immunoaffinity chromatography. Biochem Biophys Res Commun, 109, 21–29.

Fredriksson,R. and Schiöth,H.B. (2005) The repertoire of G-protein-coupled receptors in fully sequenced genomes. Mol Pharmacol, 67, 1414–1425.

Fronik,P. et al. (2017) Bitopic Ligands and Metastable Binding Sites: Opportunities for G-protein-Coupled Receptor (GPCR) Medicinal Chemistry. J Med Chem, 60, 4126–4134.

Fuxe,K. et al. (2012) On the existence and function of galanin receptor heteromers in the central nervous system. Front Endocrinol (Lausanne), 3, 34962.

Galés,C. et al. (2006) Probing the activation-promoted structural rearrangements in preassembled receptor-G-protein complexes. Nat Struct Mol Biol, 13, 778–786.

Gallo,M. et al. (2022) Disrupting GPCR Complexes with Smart Drug-like Peptides. Pharmaceutics, 14.

Garća,M. et al. (2017) Central Hypothyroidism Due to a TRHR Mutation Causing Impaired Ligand Affinity and Transactivation of Gq. J Clin Endocrinol Metab, 102, 2433.

Gennick,S.E. et al. (1987) Characterization of the Subunit Structure of the Thyrotropin Receptor in the FRTL-5 Rat Thyroid Cell Line. Endocrinology, 121, 2119–2130.

Ghosh,I. et al. (2000) Antiparallel leucine zipper-directed protein reassembly: Application to the green fluorescent protein [12]. J Am Chem Soc, 122, 5658–5659.

Gilman,A.G. (1987) G-proteins: transducers of receptor-generated signals. Annu Rev Biochem, 56, 615–649.

Glukhova,A. et al. (2017) Structure of the Adenosine A1 Receptor Reveals the Basis for Subtype Selectivity. Cell, 168, 867-877.e13.

Gomes,I. et al. (2016) G-protein-Coupled Receptor Heteromers. Annu Rev Pharmacol Toxicol, 56, 403–425.

Gonzalez,A. et al. (2012) Impact of Helix Irregularities on Sequence Alignment and Homology Modeling of G-protein-Coupled Receptors. ChemBioChem, 13, 1393–1399.

González,A. et al. (2011) Molecular Basis of Ligand Dissociation in β-Adrenergic Receptors. PLoS One, 6, e23815.

Gorman,A.L. et al. (1997) The d- and l- isomers of methadone bind to the non-competitive site on the N-methyl-D-aspartate (NMDA) receptor in rat forebrain and spinal cord. Neurosci Lett, 223, 5–8.

Gowers,R. et al. (2016) MDAnalysis: A Python Package for the Rapid Analysis of Molecular Dynamics Simulations. In, Proceedings of the 15th Python in Science Conference.

Granzin,J. et al. (1998) X-ray crystal structure of arrestin from bovine rod outer segments. Nature, 391, 918–921.

Grundt,P. et al. (2005) Novel heterocyclic trans olefin analogues of N-{4-[4-(2,3-dichlorophenyl) piperazin-1-yl]butyl}arylcarboxamides as selective probes with high affinity for the dopamine D3 receptor. J Med Chem, 48, 839–848.

Guidotti,G. et al. (2017) Cell-Penetrating Peptides: From Basic Research to Clinics. Trends Pharmacol Sci, 38, 406–424.

Guinart,D. et al. (2020) Altered Signaling in CB1R-5-HT2AR Heteromers in Olfactory Neuroepithelium Cells of Schizophrenia Patients is Modulated by Cannabis Use. Schizophr Bull, 46, 1547–1557.

Guitart,X. et al. (2019) Biased G-protein-Independent Signaling of Dopamine D1-D3 Receptor Heteromers in the Nucleus Accumbens. Mol Neurobiol, 56, 6756–6769.

Guitart,X. et al. (2014) Functional selectivity of allosteric interactions within G-protein-coupled receptor oligomers: The dopamine D1-D3receptor heterotetramer. Mol Pharmacol, 86, 417–429.

Hanania,T. et al. (2019) The N-Methyl-D-Aspartate Receptor Antagonist d-Methadone Acutely Improves Depressive-Like Behavior in the Forced Swim Test Performance of Rats. Exp Clin Psychopharmacol.

Hassan,N.M. et al. (2017) Protein-Ligand Blind Docking Using QuickVina-W With Inter-Process Spatio-Temporal Integration. Scientific Reports 2017 7:1, 7, 1–13.

Hauser,A.S. et al. (2022) Common coupling map advances GPCR-G-protein selectivity. Elife, 11.

Hauser,A.S. et al. (2017) Trends in GPCR drug discovery: new agents, targets and indications. Nat Rev Drug Discov, 16, 829.

He,X. et al. (2020) A fast and high-quality charge model for the next generation general AMBER force field. Journal of Chemical Physics, 153, 114502.

Hedderich,J.B. et al. (2022) The pocketome of G-protein-coupled receptors reveals previously untargeted allosteric sites. Nat Commun, 13.

Henningfield,J. et al. (2022) REL-1017 (esmethadone; d-methadone) does not cause reinforcing effect, physical dependence and withdrawal signs in Sprague Dawley rats. Sci Rep, 12.

Henzler-Wildman,K. and Kern,D. (2007) Dynamic personalities of proteins. Nature 2007 450:7172, 450, 964–972.

Heté Nyi,C. and Van Der Spoel,D. (2002) Efficient docking of peptides to proteins without prior knowledge of the binding site. Protein Science, 11, 1729–1737.

Hilger,D. et al. (2018) Structure and dynamics of GPCR signaling complexes. Nat Struct Mol Biol, 25, 4–12.

Hilger,D. (2021) The role of structural dynamics in GPCR-mediated signaling. FEBS J, 288, 2461–2489.

Hoshino,Y. et al. (2014) Interaction between synthetic particles and biomacromolecules: fundamental study of nonspecific interaction and design of nanoparticles that recognize target molecules. Polymer Journal 2014 46:9, 46, 537–545.

Howlett,A.C. and Fleming,R.M. (1984) Cannabinoid inhibition of adenylate cyclase. Pharmacology of the response in neuroblastoma cell membranes. Mol Pharmacol, 26, 532.

Hua,X.Y. et al. (2004) Galanin Acts at GalR1 Receptors in Spinal Antinociception: Synergy with Morphine and AP-5. Journal of Pharmacology and Experimental Therapeutics, 308, 574–582.

Huang,J. et al. (2013) Crystal structure of oligomeric β 1-adrenergic G-protein-coupled receptors in ligand-free basal state. Nat Struct Mol Biol, 20, 419–425.

Huang,S. et al. (2022) GPCRs steer Gi and Gs selectivity via TM5-TM6 switches as revealed by structures of serotonin receptors. Mol Cell, 82, 2681-2695.e6.

Huang,W. et al. (2015) Structural insights into μ-opioid receptor activation. Nature, 524, 315–321.

Huang,W. et al. (2020) Structure of the neurotensin receptor 1 in complex with β-arrestin 1. Nature, 579, 303–308.

Huhn,M. et al. (2019) Comparative efficacy and tolerability of 32 oral antipsychotics for the acute treatment of adults with multi-episode schizophrenia: a systematic review and network meta-analysis. The Lancet, 394, 939–951.

Hurowitz,E.H. et al. (2000) Genomic Characterization of the Human Heterotrimeric G-protein α, β, and γ Subunit Genes. DNA Research, 7, 111–120.

Im,D. et al. (2020) Structure of the dopamine D2 receptor in complex with the antipsychotic drug spiperone. Nat Commun, 11.

Inoue,A. et al. (2019) Illuminating G-Protein-Coupling Selectivity of GPCRs. Cell, 177, 1933-1947.e25.

Isberg,V. et al. (2015) Generic GPCR residue numbers – aligning topology maps while minding the gaps. Trends Pharmacol Sci, 36, 22–31.

Isberg,V. et al. (2016) GPCRdb: an information system for G-protein-coupled receptors. Nucleic Acids Res, 44, D356–D364.

Jang,W. et al. (2023) The role of G-protein conformation in receptor–G-protein selectivity. Nature Chemical Biology 2023 19:6, 19, 687–694.

Jelinek,V. et al. (2021) Structures in G-proteins important for subtype selective receptor binding and subsequent activation. Communications Biology 2021 4:1, 4, 1–11.

Jiang,W. and Zheng,S. (2022) Structural insights into galanin receptor signaling. Proc Natl Acad Sci U S A, 119, e2121465119.

Jorgensen,W.L. et al. (1983) Comparison of simple potential functions for simulating liquid water. J Chem Phys, 79, 926–935.

Jumper,J. et al. (2021) Highly accurate protein structure prediction with AlphaFold. Nature 2021 596:7873, 596, 583–589.

Kang,Y. et al. (2018) Cryo-EM structure of human rhodopsin bound to an inhibitory G-protein. Nature 2018 558:7711, 558, 553–558.

Kang,Y. et al. (2015) Crystal structure of rhodopsin bound to arrestin by femtosecond X-ray laser. Nature, 523, 561–567.

Karplus,M. and McCammon,J.A. (2002) Molecular dynamics simulations of biomolecules. Nat Struct Biol, 9.

Karplus,M. and Petsko,G.A. (1990) Molecular dynamics simulations in biology. Nature, 347.

Katritch,V. et al. (2013) Structure-function of the G-protein-coupled receptor superfamily. Annu Rev Pharmacol Toxicol, 53, 531–556.

Kerppola,T.K. (2006) Design and implementation of bimolecular fluorescence complementation (BiFC) assays for the visualization of protein interactions in living cells. Nature Protocols 2006 1:3, 1, 1278–1286.

Klein,M.E. et al. (2020) Opioid system is necessary but not sufficient for antidepressive actions of ketamine in rodents. Proc Natl Acad Sci U S A, 117, 2656–2662.

Koehl,A. et al. (2019) Structural insights into the activation of metabotropic glutamate receptors. Nature 2019 566:7742, 566, 79–84.

Köfalvi,A. et al. (2020) Control of glutamate release by complexes of adenosine and cannabinoid receptors. BMC Biol, 18.

Kolakowski,L.F. (1994) GCRDb: a G-protein-coupled receptor database. Recept Channels, 2, 1–7.

Komolov,K.E. and Benovic,J.L. (2018) G-protein-coupled receptor kinases: Past, present and future. Cell Signal, 41, 17–24.

Kooistra,A.J. et al. (2021) GPCRdb in 2021: Integrating GPCR sequence, structure and function. Nucleic Acids Res, 49, D335–D343.

Krishna Kumar,K. et al. (2019) Structure of a Signaling Cannabinoid Receptor 1-G-protein Complex. Cell, 176, 448-458.e12.

Kristensen,K. (1995) The mu1, mu2, delta, kappa opioid receptor binding profiles of methadone stereoisomers and morphine. Life Sci, 56, PL45–PL50.

Kruse,A.C. et al. (2013) Activation and allosteric modulation of a muscarinic acetylcholine receptor. Nature, 504, 101–106.

Kumar,R. et al. (2009) Evaluation of D2 and D3 dopamine receptor selective compounds on l-dopa-dependent abnormal involuntary movements in rats. Neuropharmacology, 56, 956–969.

Kumar,V. et al. (2016) Highly selective dopamine D3 receptor (D3R) antagonists and partial agonists based on eticlopride and the D3R crystal structure: New leads for opioid dependence treatment. J Med Chem, 59, 7634–7650.

Lane,J.R. et al. (2020) Distinct inactive conformations of the dopamine D2 and D3 receptors correspond to different extents of inverse agonism. Elife, 9.

Lang,R. et al. (2015) Physiology, Signaling, and Pharmacology of Galanin Peptides and Receptors: Three Decades of Emerging Diversity. Pharmacol Rev, 67, 118–175.

Lanza,K. et al. (2018) Behavioral and cellular dopamine D1 and D3 receptor-mediated synergy: Implications for L-DOPA-induced dyskinesia. Neuropharmacology, 138, 304–314.

Lanza,K. et al. (2021) Genetic suppression of the dopamine D3 receptor in striatal D1 cells reduces the development of L-DOPA-induced dyskinesia. Exp Neurol, 336.

Laskowski,R.A. et al. (1993) PROCHECK: a program to check the stereochemical quality of protein structures. J Appl Crystallogr, 26, 283–291.

Latorraca,N.R. et al. (2017) GPCR dynamics: Structures in motion. Chem Rev, 117, 139–155.

Lazar,J. et al. (2011) Suppression of air refractive index variations in high-resolution interferometry. Sensors (Basel), 11, 7644–7655.

Lee,Y. et al. (2020) Molecular basis of β-arrestin coupling to formoterol-bound β1-adrenoceptor. Nature, 583, 862–866.

Lerner,E. et al. (2021) FRET-based dynamic structural biology: Challenges, perspectives and an appeal for open-science practices. Elife, 10.

Leucht,S. et al. (2009) Second-generation versus first-generation antipsychotic drugs for schizophrenia: a meta-analysis. The Lancet, 373, 31–41.

Levinstein,M.R. et al. (2023) Mu Opioid Receptor Activation Mediates (S)-ketamine Reinforcement in Rats: Implications for Abuse Liability. Biol Psychiatry, 93, 1118–1126.

Limbird,L.E. et al. (1975) Beta-adrenergic receptors: evidence for negative cooperativity. Biochem Biophys Res Commun, 64, 1160–1168.

Liu,J. et al. (2022) Biased signaling due to oligomerization of the G-protein-coupled platelet-activating factor receptor. Nature Communications 2022 13:1, 13, 1–16.

Liu,Q. et al. (2021) Ligand recognition and G-protein coupling selectivity of cholecystokinin A receptor. Nature Chemical Biology 2021 17:12, 17, 1238–1244.

Liu,S. et al. (2022) Differential activation mechanisms of lipid GPCRs by lysophosphatidic acid and sphingosine 1-phosphate. Nat Commun, 13.

Lomize,M.A. et al. (2012) OPM database and PPM web server: Resources for positioning of proteins in membranes. Nucleic Acids Res, 40.

Lomize,M.A. et al. (2006) OPM: Orientations of proteins in membranes database. Bioinformatics, 22, 623–625.

Lundblad,M. et al. (2002) Pharmacological validation of behavioural measures of akinesia and dyskinesia in a rat model of Parkinson's disease. European Journal of Neuroscience, 15, 120–132.

Machleidt,T. et al. (2015) NanoBRET--A Novel BRET Platform for the Analysis of Protein-Protein Interactions. ACS Chem Biol, 10, 1797–1804.

Maeda,S. et al. (2021) Endogenous agonist-bound S1PR3 structure reveals determinants of G-protein-subtype bias. Sci Adv, 7.

Maehle,A.H. et al. (2002) The emergence of the drug receptor theory. Nat Rev Drug Discov, 1, 637–641.

Maier,J.A. et al. (2015) ff14SB: Improving the Accuracy of Protein Side Chain and Backbone Parameters from ff99SB. J Chem Theory Comput, 11, 3696–3713.

Manglik,A. et al. (2012) Crystal structure of the μ-opioid receptor bound to a morphinan antagonist. Nature, 485, 321–326.

Marcellino,D. et al. (2008) Identification of dopamine D1-D3 receptor heteromers. Indications for a role of synergistic D1-D3 receptor interactions in the striatum. J Biol Chem, 283, 26016–26025.

De Martin,S. et al. (2021) REL-1017 (Esmethadone) Increases Circulating BDNF Levels in Healthy Subjects of a Phase 1 Clinical Study. Front Pharmacol, 12.

Martin,T.J. et al. (2007) Opioid self-administration in the nerve-injured rat: Relevance of antiallodynic effects to drug consumption and effects of intrathecal analgesics. Anesthesiology, 106, 312–322.

Martí-Renom,M.A. et al. (2000) Comparative protein structure modeling of genes and genomes. Annu Rev Biophys Biomol Struct, 29, 291–325.

Maßberg,D. and Hatt,H. (2018) Human olfactory receptors: Novel cellular functions outside of the nose. Physiol Rev, 98, 1739–1763.

Masuho,I. et al. (2023) Rules and mechanisms governing G-protein coupling selectivity of GPCRs. Cell Rep, 42, 113173.

Masureel,M. et al. (2018) Structural insights into binding specificity, efficacy and bias of a β 2 AR partial agonist. Nat Chem Biol, 14, 1059–1066.

Mayol,E. et al. (2020) HomolWat: a web server tool to incorporate 'homologous' water molecules into GPCR structures. Nucleic Acids Res, 48, W54–W59.

McCorvy,J.D. et al. (2018) Structure-inspired design of β-arrestin-biased ligands for aminergic GPCRs. Nat Chem Biol, 14, 126–134.

Michaud-Agrawal,N. et al. (2011) MDAnalysis: A toolkit for the analysis of molecular dynamics simulations. J Comput Chem, 32, 2319–2327.

Milletti,F. (2012) Cell-penetrating peptides: classes, origin, and current landscape. Drug Discov Today, 17, 850–860.

Miyawaki,A. (2008) Green Fluorescent Protein Glows Gold. Cell, 135, 987–990.

Mombaerts,P. (2004) Genes and ligands for odorant, vomeronasal and taste receptors. Nature Reviews Neuroscience 2004 5:4, 5, 263–278.

Moreno,E. et al. (2017) Functional μ-Opioid-Galanin Receptor Heteromers in the Ventral Tegmental Area. Journal of Neuroscience, 37, 1176–1186.

Moreno,J.L. et al. (2016) Allosteric signaling through an mGlu2 and 5-HT2A heteromeric receptor complex and its potential contribution to schizophrenia. Sci Signal, 9.

Müller,S.M. et al. (2013) Quantification of Förster resonance energy transfer by monitoring sensitized emission in living plant cells. Front Plant Sci, 4.

Munk,C. et al. (2019) An online resource for GPCR structure determination and analysis. Nature Methods 2019 16:2, 16, 151–162.

Munk,C. et al. (2016) GPCRdb: the G-protein-coupled receptor database – an introduction. Br J Pharmacol, 173, 2195–2207.

Navarro,G., Cordomí,A., Brugarolas,M., et al. (2018) Cross-communication between Gi and Gs in a G-protein-coupled receptor heterotetramer guided by a receptor C-terminal domain. BMC Biol, 16.

Navarro,G., Cordomí,A., Casadó-Anguera,V., et al. (2018) Evidence for functional pre-coupled complexes of receptor heteromers and adenylyl cyclase. Nat Commun, 9.

Navarro,G. et al. (2010) Interactions between Intracellular Domains as Key Determinants of the Quaternary Structure and Function of Receptor Heteromers *. Journal of Biological Chemistry, 285, 27346–27359.

Navarro,G. et al. (2016) Quaternary structure of a G-protein-coupled receptor heterotetramer in complex with Gi and Gs. BMC Biol, 14.

Newman,A.H. et al. (2020) 2016 Philip S. Portoghese Medicinal Chemistry Lectureship: Designing Bivalent or Bitopic Molecules for G-Protein Coupled Receptors. The Whole Is Greater Than the Sum of Its Parts. J Med Chem, 63, 1779–1797.

Ng,G.Y.K. et al. (1996) Dopamine D2 Receptor Dimers and Receptor-Blocking Peptides. Biochem Biophys Res Commun, 227, 200–204.

Niederberger,E. et al. (2017) Drugging the pain epigenome. Nat Rev Neurol, 13, 434–447.

Nygaard,R. et al. (2013) The dynamic process of β(2)-adrenergic receptor activation. Cell, 152, 532–542.

O'Connor,E.C. et al. (2011) The predictive validity of the rat self-administration model for abuse liability. Neurosci Biobehav Rev, 35, 912–938.

Ögren,S.O. et al. (1997) Prolonged treatment with haloperidol and clozapine in the rat: Differential effects on spontaneous and theophylline-induced motor activity. Neurosci Lett, 232, 21–24.

Okashah,N. et al. (2019) Variable G-protein determinants of GPCR coupling selectivity. Proc Natl Acad Sci U S A, 116, 12054–12059.

Oldham,W.M. and Hamm,H.E. (2008) Heterotrimeric G-protein activation by G-protein-coupled receptors. Nat Rev Mol Cell Biol, 9, 60–71.

Oprea,T.I. et al. (2018) Unexplored therapeutic opportunities in the human genome. Nat Rev Drug Discov, 17, 317–332.

Overton,M.C. and Blumer,K.J. (2000) G-protein-coupled receptors function as oligomers in vivo. Current Biology, 10, 341–344.

Palczewski,K. et al. (2000) Crystal structure of rhodopsin: A G-protein-coupled receptor. Science (1979), 289, 739–745.

Pándy-Szekeres,G. et al. (2018) GPCRdb in 2018: Adding GPCR structure models and ligands. Nucleic Acids Res, 46.

Papasergi-Scott,M.M. et al. (2020) Structures of metabotropic GABAB receptor. Nature, 584, 310.

Papasergi-Scott,M.M. et al. (2023) Time-resolved cryo-EM of G-protein activation by a GPCR. bioRxiv, 2023.03.20.533387.

Pellissier,L.P. et al. (2009) Conformational toggle switches implicated in basal constitutive and agonist-induced activated states of 5-hydroxytryptamine-4 receptors. Mol Pharmacol, 75, 982–990.

Persechino,M. et al. (2022) Allosteric modulation of GPCRs: From structural insights to in silico drug discovery. Pharmacol Ther, 237, 108242.

Peterson,Y.K. and Luttrell,L.M. (2017) The Diverse Roles of Arrestin Scaffolds in G-protein-Coupled Receptor Signaling. Pharmacol Rev, 69, 256–297.

Pin,J.P. et al. (2007) International Union of Basic and Clinical Pharmacology. LXVII. Recommendations for the recognition and nomenclature of G-protein-coupled receptor heteromultimers. Pharmacol Rev, 59, 5–13.

Qi,C. et al. (2019) The structure of a membrane adenylyl cyclase bound to an activated stimulatory G-protein. Science, 364, 389–394.

Rasmussen,K. et al. (2018) NIDA's medication development priorities in response to the Opioid Crisis: ten most wanted. Neuropsychopharmacology 2018 44:4, 44, 657–659.

Rasmussen,S.G.F. et al. (2011) Crystal structure of the β2 adrenergic receptor-Gs protein complex. Nature, 477, 549–557.

Renaud,J.P. et al. (2018) Cryo-EM in drug discovery: achievements, limitations and prospects. Nat Rev Drug Discov, 17, 471–492.

Riddle,L.R. et al. (2011) Evaluation of the D3 dopamine receptor selective agonist/partial agonist PG01042 on l-dopa dependent animal involuntary movements in rats. Neuropharmacology, 60, 284–294.

Rodríguez-Frade,J.M. et al. (1999) The chemokine monocyte chemoattractant protein-1 induces functional responses through dimerization of its receptor CCR2. Proc Natl Acad Sci U S A, 96, 3628–3633.

Rosenbaum,D.M. et al. (2007) GPCR engineering yields high-resolution structural insights into beta2-adrenergic receptor function. Science, 318, 1266–1273.

Sadler,F. et al. (2023) Autoregulation of GPCR signalling through the third intracellular loop. Nature 2023 615:7953, 615, 734–741.

Šali,A. and Blundell,T.L. (1993) Comparative protein modelling by satisfaction of spatial restraints. J Mol Biol, 234, 779–815.

Samaha,A.N. et al. (2007) 'Breakthrough' dopamine supersensitivity during ongoing antipsychotic treatment leads to treatment failure over time. Journal of Neuroscience, 27, 2979–2986.

Sanchez-Soto,M. et al. (2020) A structural basis for how ligand binding site changes can allosterically regulate GPCR signaling and engender functional selectivity. Sci Signal, 13.

Sandhu,M. et al. (2022) Dynamic spatiotemporal determinants modulate GPCR:G-protein coupling selectivity and promiscuity. Nature Communications 2022 13:1, 13, 1–14.

Sansuk,K. et al. (2011) A Structural Insight into the Reorientation of Transmembrane Domains 3 and 5 during Family A G-protein-Coupled Receptor Activation. Mol Pharmacol, 79, 262–269.

Schertler,G.F.X. et al. (1993) Projection structure of rhodopsin. Nature 1993 362:6422, 362, 770–772.

Schmid,C.L. et al. (2017) Bias Factor and Therapeutic Window Correlate to Predict Safer Opioid Analgesics. Cell, 171, 1165.e13-1175.e13.

Schöneberg,T. and Liebscher,I. (2021) Mutations in G-protein–coupled receptors: Mechanisms, pathophysiology and potential therapeutic approaches. Pharmacol Rev, 73, 89–119.

Schott-Verdugo,S. and Gohlke,H. (2019) PACKMOL-Memgen: A Simple-To-Use, Generalized Workflow for Membrane-Protein-Lipid-Bilayer System Building. J Chem Inf Model.

Schwartz,J.C. et al. (1998) Functional implications of multiple dopamine receptor subtypes: The D1/D3 receptor coexistence. Brain Res Rev, 26, 236–242.

Schwarze,S.R. et al. (1999) In vivo protein transduction: Delivery of a biologically active protein into the mouse. Science (1979), 285, 1569–1572.

Serrano-Vega,M.J. et al. (2008) Conformational thermostabilization of the beta1-adrenergic receptor in a detergent-resistant form. Proc Natl Acad Sci U S A, 105, 877–882.

Shimada,I. et al. (2018) GPCR drug discovery: integrating solution NMR data with crystal and cryo-EM structures. Nature Reviews Drug Discovery 2018 18:1, 18, 59–82.

Sievers,F. et al. (2011) Fast, scalable generation of high-quality protein multiple sequence alignments using Clustal Omega. Mol Syst Biol, 7, 539.

Silvestri,S. et al. (2000) Increased dopamine D2 receptor binding after long-term treatment with antipsychotics in humans: A clinical PET study. Psychopharmacology (Berl), 152, 174–180.

Singh,P. et al. (2008) Structures of rhodopsin kinase in different ligand states reveal key elements involved in G-protein-coupled receptor kinase activation. J Biol Chem, 283, 14053–14062.

Siu,F.Y. et al. (2013) Structure of the human glucagon class B G-protein-coupled receptor. Nature, 499, 444–449.

Smith,J.S. et al. (2018) Biased Signalling: From Simple Switches to Allosteric Microprocessors. Nat Rev Drug Discov, 17, 243.

Smith,N.J. and Milligan,G. (2010) Allostery at G-protein-Coupled Receptor Homo- and Heteromers: Uncharted Pharmacological Landscapes. Pharmacol Rev, 62, 701–725.

Søndergaard,C.R. et al. (2011) Improved treatment of ligands and coupling effects in empirical calculation and rationalization of p K a values. J Chem Theory Comput, 7, 2284–2295.

Spiga,R. et al. (1996) Human methadone self-administration: effects of dose and ratio requirement. Behavioural Pharmacology, 7.

Sperger,T. et al. (2016) Computation and Experiment: A Powerful Combination to Understand and Predict Reactivities. Acc Chem Res, 49, 1311–1319.

Starr,B.S. et al. (1987) Behavioural role of dopamine D1 receptors in the reserpine-treated mouse. Neuroscience, 22, 179–188.

Steinpreis,R.E. et al. (1996) Methadone produces conditioned place preference in the rat. Pharmacol Biochem Behav, 54, 339–341.

Stenkamp,R.E. et al. (2018) Identifying G-protein-coupled receptor dimers from crystal packings. urn:issn:2059-7983, 74, 655–670.

Strang,J. et al. (2020) Opioid use disorder. Nat Rev Dis Primers, 6.

Strohman,M.J. et al. (2019) Local membrane charge regulates β2 adrenergic receptor coupling to Gi3. Nat Commun, 10.

Sun,B. et al. (2021) Crystal structure of dopamine D1 receptor in complex with G-protein and a non-catechol agonist. Nature Communications 2021 12:1, 12, 1–9.

Suzuki,T. et al. (2015) Dopamine supersensitivity psychosis as a pivotal factor in treatment-resistant schizophrenia. Psychiatry Res, 227, 278–282.

Syrovatkina,V. et al. (2016) Regulation, Signaling, and Physiological Functions of G-Proteins. J Mol Biol, 428, 3850–3868.

Szalai,B. et al. (2014) Improved Methodical Approach for Quantitative BRET Analysis of G-protein Coupled Receptor Dimerization. PLoS One, 9, e109503.

Unger,V.M. and Schertler,G.F. (1995) Low resolution structure of bovine rhodopsin determined by electron cryo-microscopy. Biophys J, 68, 1776–1786.

Urizar,E. et al. (2011) CODA-RET reveals functional selectivity as a result of GPCR heteromerization. Nat Chem Biol, 7, 624.

Valle-León,M. et al. (2021) Decreased striatal adenosine A2A-dopamine D2 receptor heteromerization in schizophrenia. Neuropsychopharmacology, 46, 665–672.

Vangone,A. and Bonvin,A.M.J.J. (2015) Contacts-based prediction of binding affinity in protein–protein complexes. Elife, 4.

Velazhahan,V. et al. (2021) Structure of the class D GPCR Ste2 dimer coupled to two G-proteins. Nature, 589, 148–153.

Venkatakrishnan,A.J. et al. (2016) Diverse activation pathways in class A GPCRs converge near the G-protein-coupling region. Nature, 536, 484–487.

Viñals,X. et al. (2015) Cognitive Impairment Induced by Delta9-tetrahydrocannabinol Occurs through Heteromers between Cannabinoid CB1 and Serotonin 5-HT2A Receptors. PLoS Biol, 13, e1002194.

Volkow,N.D. and Collins,F.S. (2017) The Role of Science in Addressing the Opioid Crisis. New England Journal of Medicine, 377, 391–394.

Waldo,G.L. et al. (2010) Kinetic scaffolding mediated by a phospholipase C-beta and Gq signaling complex. Science, 330, 974–980.

Wall,M.A. et al. (1995) The structure of the G-protein heterotrimer Gi alpha 1 beta 1 gamma 2. Cell, 83, 1047–1058.

Wang,C., Jiang,Y., et al. (2013) Structural basis for molecular recognition at serotonin receptors. Science (1979), 340, 610–614.

Wang,C., Wu,H., et al. (2013) Structure of the human smoothened receptor bound to an antitumour agent. Nature, 497, 338–343.

Wang,S. et al. (2018) Structure of the D2 dopamine receptor bound to the atypical antipsychotic drug risperidone. Nature, 555, 269–273.

Weis,W.I. and Kobilka,B.K. (2018) The Molecular Basis of G-protein-Coupled Receptor Activation. Annu Rev Biochem, 87, 897–919.

Wheatley,M. et al. (2012) Lifting the lid on GPCRs: the role of extracellular loops. Br J Pharmacol, 165, 1688–1703.

Whorton,M.R. and MacKinnon,R. (2013) X-ray structure of the mammalian GIRK2-βγ G-protein complex. Nature, 498, 190–197.

Williams,J.T. et al. (2013) Regulation of μ-Opioid Receptors: Desensitization, Phosphorylation, Internalization, and Tolerance. Pharmacol Rev, 65, 223–254.

Williams,N.R. et al. (2018) Attenuation of antidepressant effects of ketamine by opioid receptor antagonism. American Journal of Psychiatry, 175, 1205–1215.

Wingler,L.M. et al. (2020) Angiotensin and biased analogs induce structurally distinct active conformations within a GPCR. Science (1979), 367, 888–892.

Wirz,S.A. et al. (2005) Homodimerization and internalization of galanin type 1 receptor in living CHO cells. Neuropeptides, 39, 535–546.

Wootten,D. et al. (2018) Mechanisms of signalling and biased agonism in G-protein-coupled receptors. Nat Rev Mol Cell Biol, 19, 638–653.

Wouters,E. et al. (2018) Assessing GPCR dimerization in living cells: Comparison of the nanobit assay with related bioluminescence- and fluorescence-based approaches. Neuromethods, 140, 239–250.

Wu,B. et al. (2010) Structures of the CXCR4 chemokine GPCR with small-molecule and cyclic peptide antagonists. Science, 330, 1066–1071.

Xiao,R.P. et al. (1999) Coupling of β2-adrenoceptor to G(i) proteins and its physiological relevance in murine cardiac myocytes. Circ Res, 84, 43–52.

Xing,C. et al. (2020) Cryo-EM Structure of the Human Cannabinoid Receptor CB2-Gi Signaling Complex. Cell, 180, 645-654.e13.

Xu,F. et al. (2011) Structure of an agonist-bound human A2A adenosine receptor. Science, 332, 322–327.

Yin,J. et al. (2020) Structure of a D2 dopamine receptor–G-protein complex in a lipid membrane. Nature, 584, 125–129.

Yue,Y. et al. (2022) Structural insight into apelin receptor-G-protein stoichiometry. Nature Structural & Molecular Biology 2022 29:7, 29, 688–697.

Zhang,Y. et al. (2017) Cryo-EM structure of the activated GLP-1 receptor in complex with a G-protein. Nature, 546, 248–253.

Zhou,P., Li,B., et al. (2018) Hierarchical Flexible Peptide Docking by Conformer Generation and Ensemble Docking of Peptides. J Chem Inf Model, 58, 1292–1302.

Zhou,P., Jin,B., et al. (2018) HPEPDOCK: a web server for blind peptide-protein docking based on a hierarchical algorithm. Nucleic Acids Res, 46, W443–W450.

Zhou,Q. et al. (2019) Common activation mechanism of class a GPCRs. Elife, 8.

Zhuang,Y. et al. (2022) Molecular recognition of morphine and fentanyl by the human μ-opioid receptor. Cell, 185, 4361-4375.e19.

Zhuang,Y. et al. (2021) Structural insights into the human D1 and D2 dopamine receptor signaling complexes. Cell, 184, 931-942.e18.

Zhuang,Y. et al. (2020) Structure of formylpeptide receptor 2-Gi complex reveals insights into ligand recognition and signaling. Nat Commun, 11.